Active Tectonics of the Northeastern Tibetan Plateau(Dissertation_全文)

AUTHOR(S):

Chen, Peng

CITATION:

Chen, Peng. Active Tectonics of the Northeastern Tibetan Plateau. 京都大学, 2019, 博士(理学)

ISSUE DATE:

2019-11-25

URL:

https://doi.org/10.14989/doctor.k22113

京都大学　　博士論文

チベット高原北東部のアクティブテクトニクス

2019 年 6 月

大学院　理学研究科

地球惑星科学専攻

陳　鵬

THESIS

Active Tectonics of the Northeastern Tibetan Plateau

June 2019

Department of Geophysics, Graduate School of Science,

Kyoto University

Peng Chen

Abstract

The uplift of the Tibetan Plateau is regarded as the consequence of the collision and convergence between the Indian and Eurasian Plates, and the uplift in turn caused enormous changes in topography and the geodynamic processes. The northeastern marginal zone of the Tibetan Plateau, as the frontal belt of plateau outward expansion, is an ideal region to study the intracontinental active tectonic deformation, which can provide important constraints recording the active tectonic processes and the geodynamic mechanism of northeastward expansion of the Tibetan Plateau. To understand the active tectonism of the northeastern Tibetan Plateau, this study focuses on the active tectonics containing the tectonic geomorphology, active flexural folding and faulting using comprehensive methods including three dimension (3D) topographic analysis, field investigations, trench excavations and radiocarbon dating.

1) Based on the detailed topographic analysis via the drainage systems extraction, satellite images interpretation, 3D reconstruction of digital elevation models (DEM) data, together with field observations reveal that: i) the WNW-trending en echelon topographic divides between the Haiyuan Fault and the West Qinling Fault in the northeastern marginal zone of the Tibetan Plateau were defined, and these topographic divides separate the tributary drainage systems of the Yellow River; ii) the late Cenozoic strata and deposits distributed on both sides of these divides has been tilted and folded, and the latest fluvial deposits are also tilted, manifesting that the tectonic tilting and uplifting is still active near these divides; and iii) the maximum compressive stress inferred from the fold deformation, trends NE-SW to ENE–WSW. These results demonstrate that the formation of these en echelon topographic divides separating the Yellow River drainage systems in the northeastern Tibetan Plateau is possibly associated

with the flexural folding and uplifting under the northeastward compressive stress, in response to the ongoing convergence between the Indian and Eurasian plates.

2) The West Qinling Fault (WQLF), the target of this study, one important active strike-slip faults in the northeastern Tibetan Plateau, trends WNW–ESE in the east and nearly E–W in the west. Based on the interpretation of the Google Earth images and 3D topographic images, field investigations, and ^{14}C dating results reveal that i) the drainage systems, mountain ridges, alluvial fans, and terraces across the WQLF have been systematically left-lateral deflected and/or offset by ~7 m up to hundreds of meters during the late Pleistocene–Holocene; ii) the left-lateral strike-slip rate of the WQLF is estimated to be 2.0–2.6 mm/yr since the late Pleistocene; iii) in contrast to the well-known active strike-slip faults developed in the northern and northwestern Tibetan Plateau such as the Altyn Tagh Fault and the Kunlun Fault with high slip rate of > 10–20 mm/yr, the WQLF displays a characteristically low strike-slip rate of < 3 mm/yr. The low slip rate of the WQLF suggests that most of the strain was absorbed and partitioned by continuous crustal deformation in the northeastern marginal zone of the Tibetan Plateau, rather than the horizontal displacement along the active strike-slip faults.

3) Topographic analysis associated with active faulting and trench excavations, together with radiocarbon dating results reveal that: i) the most recent surface-rupturing earthquake (E1) occurred after 760–471 yr Cal BP. This means that an unrecorded historic earthquake capable of producing surface rupture occurred near the trench 2. If no large historic earthquakes should be missed in the catalogue, this event could only correspond to the 1654 M 8.0 Tianshui earthquake; in this case, the source seismogenic fault of the 1654 Tianshui earthquake is not the Lixian–Luojiabao fault (LLF) as previously reported, but the WQLF is; ii) the penultimate large earthquake (E2)

occurred in the period of 2693–760 yr Cal BP; iii) the third recent large earthquake (E3) occurred in the period of 10229–6032 yr Cal BP with a higher probability in the range of 9005–8596 yr Cal BP; iv) Given the wide time-span for E3 and the recurrence discipline of characteristic fault, another paleoearthquake possibly occurred in the period of 8596–6032 yr Cal BP. Then, the above E3 becomes E4 and occurred in the period of 9005–8596 yr Cal BP. Therefore, three or four large earthquakes occurred during the past ~9000 years on the WQLF, suggesting an average recurrence interval of large earthquakes of 2250–3000 years. The findings concerning with the recurrence interval of large earthquakes on the WQLF would provide valuable information for the re-assessment of seismic potential, also for a better understanding of earthquake mechanism and geodynamic implications in the northeastern Tibetan Plateau.

The results obtained in this study demonstrate that the active tectonic deformation in the northeastern Tibetan Plateau was mainly dominated by the active flexural folding and left-lateral strike-slip faulting under the NE-trending tectonic compression and that the strain energy is absorbed and partitioned by the crustal shortening, topographic uplift, and the eastward extrusion along the major strike-slip faults accommodating the ongoing convergence and collision between the Indian and Eurasian plates.

Keywords: Tibetan Plateau, Strike-slip rate, West Qinling Fault (WQLF), Lixian–Luojiabao Fault (LLF), Seismogenic fault, 1654 M 8.0 Tianshui earthquake, Topographic divides, Active faulting, Active flexural folding, Drainage systems, Yellow River, Indian–Eurasian collision.

Table of Contents

List of Tables……1

List of Figures……..2

Acknowledgements……14

Chapter 1. Introduction 17

1.1. The research history and status of the Tibetan Plateau 17

1.2. Geodynamic models about the tectonic deformation of the Tibetan Plateau..... 18

1.3. The targets and research purpose 20

Chapter 2. Studying methods 23

2.1. Interpretations of Remote sensing images and DEM processing 23

2.2. Field investigation and trench excavation..... 26

2.3. Radiocarbon dating technique..... 28

Chapter 3. Tectonic setting 33

3.1. Tectonic evolution of the NE Tibetan Plateau..... 33

3.2. Regional geology of the study area..... 36

3.3. Topographic features..... 40

Chapter 4. Tectonic geomorphology in the northeastern Tibetan Plateau..... 46

4.1. Abstract 46

4.2. Introduction..... 46

4.3. Tectonic setting 49

4.4. Method 52

4.5. Topographic divides of the tributary drainage systems of the Yellow River 52

4.6. Topographic analyses of DEM data and remote sensing images..... 53

4.7. Tectonic deformation near the topographic divides..... 55

4.8. Discussion..... 59

4.8.1. Formation timing and mechanism of the regional-scale topographic divides59

4.8.2. Tibetan–Himalayan drainage systems 60

4.9. Conclusions..... 62

Chapter 5. Late Pleistocene activity of the West Qinling Fault..... 74

5.1. Abstract 74

5.2. Introduction..... 74

5.3. Tectonic setting 76

5.4. Tectonic geomorphology..... 77

5.5. Structural features 79

5.6. Dating of deformed geomorphic surface markers..... 81

5.7. Discussion 84
5.7.1. Late Pleistocene strike-slip rate 84
5.7.2. Initial timing of left-lateral strike-slip faulting, maximum cumulative displacement and its tectonic implications 86
5.8. Conclusions 88
Chapter 6. Paleoseismic study on the West Qinling Fault 105
6.1. Abstract 105
6.2. Introduction 106
6.3. Tectonic setting 107
6.4. Faulted geomorphology 108
6.5. Outcrop observations 109
6.6. Trench investigations 110
6.6.1. Trench 1 111
6.6.2. Trench 2 112
6.7. Identification of Paleoseismic events 113
6.7.1. Event 1 114
6.7.2. Event 2 114
6.7.3. Event 3 115
6.7.4. Another inferred event (Event 4) 115
6.8. Discussion 116
6.8.1. Timing and Recurrence interval of large earthquakes on WQLF 116
6.8.2. Seismic activities on LLF and WQLF 120
6.9. Conclusions 122
Chapter 7. Discussion 136
7.1. Active tectonic characteristics in the NE Tibetan Plateau 136
7.2. Deformation mechanism of active tectonics 142
Chapter 8. Summary and conclusions 146
References: 153

List of Tables

Chapter 5.

Table 5.1. Radiocarbon dating results.

Table 5.2. Dating ages of deformed geomorphic surface markers and the corresponding offset amounts.

Chapter 6.

Table 6.1. Radiocarbon dating results.

Table 6.2. Seismic parameters of historical large earthquakes occurred in the Tibetan Plateau.

List of Figures

Chapter 2.

Fig. 2.1. Tectonic geomorphic features formed by active strike-slip faulting (cited from the Research Group for Active Faults of Japan, 1991). The alphabets are defined as follows: B: fault triangular facet; C: fault scarp facing the downstream; D: sag pond; E: tectonic bulge or push-up structures; F: fault saddle; G: graben structure; H: offset stream channel; I: shutter ridge; J: beheaded stream; K: wind gap; L–L′: offset piedmont line; M–M′: offset higher terrace; M1–M1′: offset lower terrace; Q: sag pond.

Fig. 2.2. 3D topographic images showing the fault scarps developed along the Kunlun Fault by exaggerating the topographic relief in vertical scale. The V/H means the vertical scale versus the horizontal scale. (a) V/H＝1. (b) V/H＝3. (c) V/H＝6.

Chapter 3.

Fig. 3.1. Color shaded-relief map generated from SRTM 30 PLUS (Shuttle Radar Topography Mission, 1-km-resolution) showing the topographic features of the Tibetan Plateau and adjacent area. The main active faults were labeled with the acronyms defined as follows: ATF: Altyn Tagh Fault; KLF: Kunlun Fault; HYF: Haiyuan Fault; WQLF: West Qinling Fault; LMSF: Longmenshan Fault; GYXF: Ganzi–Yushu–Xianshuihe Fault.

Fig. 3.2. Simplified sketch showing the major tectonic framework and terrane composition bounding by sutures (modified from Yin and Harrision, 2000).

Fig. 3.3. Geologic map showing the main framework and stratigraphy composition of

the Tibetan Plateau (modified from the Chengdu Institute of Geology and Mineral, CAGS, 1988). The numbers of sutures are (1) North Qilian Suture, (2) Kunlun Suture, (3) Jinsha Suture, (4) Bangong Suture, and that (5) Indo–Zangbo Suture, respectively.

Fig. 3.4. Index map showing the tectonic background and topographic features of the study area. (a) Tectonic setting showing the location and major active faults within and surrounding the Tibetan Plateau. (b) Color-shaded relief map showing the topographic characters along the Altyn Tagh Fault. (c) Color-shaded relief map showing the topographic features along the Kunlun Fault. Epicenters and focal mechanism solutions are from the Global Harvard CMT catalogue (http://www.globalcmt.org). ATF: Altyn Tagh Fault; HYF: Haiyuan Fault; WQLF: West Qinling Fault; KLF: Kunlun Fault; GYXF: Ganzi–Yushu–Xianshuihe Fault.

Chapter 4.

Fig. 4.1. Tectonic background and topographic features of the study area. (a) Tectonic setting of the study area showing the location and the major active faults within and surrounding the Tibetan Plateau. Block motion velocity of the Indian plate is cited from Zhang et al. (2004). (b) Color-shaded relief map showing the distribution of drainage systems that flow into the Yellow River, topographic divides, and major active faults on the northeastern marginal zone of the Tibetan Plateau. The drainage system was extracted from the 30-m-resolution ASTER GDEM data by using the GIS tools. Noting the left-stepping en echelon geometry of the topographic divides. Historic earthquake information from the Earthquake Disaster Prevention Department

of China Earthquake Administration catalogue (EDPDCEA, 1995). Epicenters and focal mechanism solutions are from the Global Harvard CMT catalogue (http://www.globalcmt.org). (c) Greyscale map of drainage systems without elevation information. HYF: Haiyuan Fault; WQLF: West Qinling Fault; KLF: Kunlun Fault.

Fig. 4.2. Color-shaded relief maps showing the 3D perspective of the topographic divides that separate the Yellow River drainage systems (see Fig. 4.1b for locations). The arrows with different colors show the flowing direction of rivers. The color legends representing different rivers are consistent with that shown in Fig. 4.1. The white dashed line indicates the general striking of the topographic divides.

Fig. 4.3. Topographic profiles P1–P4 across the four topographic divides (see Fig. 4.1b for locations). (P1) Qinghai-nanshan topographic divide. (P2) Lajishan divide. (P3) Maxianshan divide (P4) Huajialing divide.

Fig. 4.4. Color-shaded relief map and Google Earth images showing the geomorphological features of push-up structure or tectonic bulge developed within alluvial fans and fluvial terraces (see Fig. 4.1b for location). (a) Color-shaded relief map showing the topographic features of the Qinghai-nanshan topographic divide. (b) Overview of the geomorphological setting showing the location of alluvial fan and fluvial terrace. (c) Push-up structure or bulge developed within terrace deposits with curved axes. (d) Tectonic bulge developed within alluvial fan deposits that have been folded and uplifted, resulting in the systematic deflection of gullies to the left. (e) Terrace deposits that has been folded and uplifted. The red dashed line

indicates the general striking of the axis of the flexural fold. (f-g) Topographic profiles across the push-up structure and tectonic bulge in (d) and (e).

Fig. 4.5. Google Earth images and a field photograph showing the topographic characteristics and tectonic deformation of terrace deposits at the south side of Qinghai-nanshan divide at Loc.1 (see Fig. 4.4a for location). (a–b) Google Earth images showing the topographic features of fluvial terrace. (c) Interpreted geomorphic map of (b) to show the terrace divisions. (d) Field outcrop showing a titled bedding structure of the terrace deposits. The white arrows indicate the bedding of the terrace deposits.

Fig. 4.6. Color-shaded relief map and geological map showing the topographic features and the geological structures at the Lajishan topographic divide. (a) Geomorphic image showing the topographic characteristics of the Lajishan topographic divide that separate the Huangshui River from the Yellow River (see Fig. 4.1b for location). (b) Geological map in the periphery of Lajishan topographic divide (Modified from the Qinghai BGMR, 2009). Note the anticline and syncline structures (broken line) developed in the late Cenozoic strata and deposits.

Fig. 4.7. Color-shaded relief map and field photograph showing the topographic features around the Maxianshan topographic divide and tectonic deformation developed within the conglomerate at Loc. 2 on the northern side of the divide. (a) The Maxianshan topographic divide that separates the Yellow River from the Taohe River as shown by the drainage system distribution (see Fig. 4.1b for location). Note the change of channel width at the turning

points of the Yellow River near this divide. (b) Arc-shape curved bedding structure developed within the brownish red conglomerate. Note the dipping direction of the strata is oriented NE-trending.

Fig. 4.8. Color-shaded relief map and geological map showing the topographic features and strata composition at the Huajialing topographic divide that separate the Weihe River from the Yellow River. (a) Color-shaded relief map showing the topographic characteristics and drainage system distribution (see Fig. 4.1b for location). (b) Geological map in the periphery of the Huajialing divide (Modified from Gansu BGMR, 2006).

Fig. 4.9. Field photographs showing the strata attitude and deposits composition at Loc.3 in the Huajialing topographic divide (see Fig. 4.8b for location). (a) The tilted bedding structure developed within the terrace deposits as indicated by the white arrows. (b) Terrace deposits at the summit of Mountain, which is ~200 m higher than the riverbed, indicating a great uplift at the Huajialing area. (c) Fluvial pebbles with good roundness. (d) close-up view of fluvial pebbles.

Chapter 5.

Fig. 5.1. Tectonic background and topographic features of the study area. (a) Color-shaded relief map showing the location of the study area and the major active faults within and surrounding the Tibetan Plateau. Motion velocity of the Indian plate is cited from Zhang et al. (2004). (b) Color-shaded relief map showing the topographic and tectonic features of the study area. Historic earthquake information is from the Earthquake Disaster Prevention Department of China Earthquake Administration

catalogue (EDPDCEA, 1995) and focal mechanism are from the Global Harvard CMT catalogue (http://www.globalcmt.org). Note the offset and/or deflection of Daxiahe River and Taohe River. The acronyms used in the figure are defined as follows: ATF: Altyn Tagh Fault; KLF: Kunlun Fault; HYF: Haiyuan Fault; WQLF: West Qinling Fault; QCF; Qingchuan Fault; XSHF: Xianshuihe Fault; RRF: Red River Fault; THR; Taohe River; DXHR: Daxiahe River.

Fig. 5.2. Color-shaded relief maps showing the reconstructed process of deflected drainage systems. (a) STRM 30 PLUS 30-m-resolution color-shaded relief map showing the topography and the main tributaries of Yellow River drainage systems (see Fig. 5.1b for location). (b) Restored drainage systems after removing the ~18 km sinistral displacement along the WQLF.

Fig. 5.3. Google Earth images showing systematic offset of gullies along the WQLF with displacement amounts varying from 70 m to 390 m (see Fig. 5.1b for location). R1–R18 are deflected stream channels and Hr1–Hr18 are corresponding offset amounts. Short red lines indicate the dipping direction of the fault scarps. (a) and (c) are the original Google Earth images, and (b) and (d) are the corresponding interpreted maps.

Fig. 5.4. 3D Google Earth images and photographs showing tectonic landforms and field outcrops associated with left-lateral faulting of the WQLF (see Fig. 5.1 for location). (a) Google Earth image showing the active fault trace along the WQLF. (b) Systematic offset of geomorphological markers including stream channels and mountain ridges. R19–R23 are deflected stream channels and Hr19–Hr23 are corresponding offset amounts. (c) Continuous faulted saddles.

(d) Close-up view of saddles 2 and 3. (e–f) Offset gully and fault scarps. Short red line indicates the facing direction of the fault scarp. The blue line with arrow indicates the stream channel.

Fig. 5.5. Field photographs showing the fault outcrop observed at Loc. 1 (see Fig. 5.1b for location). (a) Overview of the fault outcrop developed along the fault scarp. The white dotted line indicates the topographic slope, note the change of slope angle. (b) Active fault developed along the contact zone between the basement rock and the colluvial deposits. (c) Striations on the main fault plane showing the principal strike-slip motion with thrust component along the WQLF. (d) Fault damage zone consisting of fault gouge and fault breccia. (e) Stereographic projection of the striations measured on the main fault plane.

Fig. 5.6. Field photographs showing the fault outcrop observed at Loc. 2 (see Fig. 5.3b for location) (a) Active fault developed along the contact zone between the basement marble and the late Quaternary sediments with lineament fault scarps extending into the highland. (b) Photographs showing the exposure position along the contact zone. (c) Close-up view of (b) showing the structural features of the fault zone. (d) Striations on the main fault plane showing the dominated strike-slip motion of the WQLF. (e) Stereo projection of the striations measured on the main fault plane.

Fig. 5.7. Field photographs showing the fault outcrop observed at Loc. 3 (see Fig. 5.3d for location) (a) Photographs showing the overview of field outcrop. (b) Interpreted map showing the faults. (c) Disturbed bedding structure due to the activity of the F2 and F3 faults. (d) Gravels bounded on the F2 and F3 faults

were dragged and re-oriented parallel to the fault plane. (e) Sketch of (c). (f) Sketch of (d). The white dotted line indicates the bedding of alluvial fan deposits.

Fig. 5.8. 3D topographic image and field photographs showing associated tectonic geomorphology along the WQLF. (a) 3D topographic image showing the active fault trace indicated by fault scarps, offset gullies and mountain ridges (see Fig. 5.2a for location). (b) Offset gullies and mountain ridges. (c–d) Field outcrops of fault scarps and an offset stream channel. (e) Sedimentary sequences of terrace deposits and ^{14}C sampling locations. The blue dotted line in (b) and (d) indicate the stream channel and the white dotted line in (e) represent the abandoned boundary of the alluvial fan deposit.

Fig. 5.9. Google Earth image and field photographs showing the faulted landforms and field outcrop. (a) Active fault trace indicated by the fault scarps and systematic deflection and/or offset of stream channels (see Fig. 5.2a for location). (b) Interpreted geomorphic map of (a). The short red line indicates the facing direction of fault scarp. (c–d) Photographs showing the offset stream channels and terrace with the offset amount of 35 m and 72 m, respectively. Noting the fault scarp perpendicular to the water flow. (e–f) ^{14}C sampling sites and sedimentary sequences of terrace deposit.

Fig. 5.10. Schematic diagram to explain the principle of calculating slip rate. D_c and D_T represent the offset of the stream channel and the terrace T_L, respectively. t_1 and t_2 represent the corresponding ages of geomorphic surface marker. S means the slip rate of the strike-slip fault. In general, $D_c \leq D_T$, but D_c is considered to be close to D_T in the causes of Figs. 5.8 and 5.9, because the

streams are well trapped in the incised channels.

Chapter 6.

Fig. 6.1. Color-shaded relief map showing the topographic and tectonic setting of the study area. (a) Index map showing the location and the major active faults within and surrounding the Tibetan Plateau. The motion velocity of the Indian Plate is cited from Zhang et al (2004). (b) Color-shaded relief map showing the topographic features and tectonic setting of the study area. Historic earthquake information are from the Earthquake Disaster Prevention Department of China Earthquake Administration catalogue (EDPDCEA, 1995) and the focal mechanism is from the Global Harvard CMT catalogue (http://www.globalcmt.org). The acronyms used in the figure are defined as follows: ATF: Altyn Tagh Fault; KLF: Kunlun Fault; HYF: Haiyuan Fault; WQLF: West Qinling Fault; XSHF: Xianshuihe Fault; RRF: Red River Fault.

Fig. 6.2. 3D Google Earth images showing the tectonic landforms associated with active strike-slip faulting along the WQLF. (a) Overview of the tectonic landforms (see Fig. 6.1b for location). (b) The active fault trace indicated by the systematical offset of stream channels and fault scarps. The red dotted line indicates the trace of active fault, and short red arrows indicate the fault scarp and the dipping direction of fault scarp. (c) The related topography including fault scarps, saddles and sag ponds.

Fig. 6.3. Google Earth images showing the tectonic landforms associated with active strike-slip faulting along the WQLF (see Fig. 6.2c for locations). (a) Continuous fault scarps facing the uphill and the gully with an offset of ~42 m. (b) Beheaded rivers bounded by the active fault. (c) Fault scarps and trench

locations with a gully deflected by ~10 m. (d) Surface rupture on an alluvial fan. The red dotted line indicates the trace of active fault and short red arrows indicate the fault scarp.

Fig. 6.4. 3D topographic image and field photographs showing the active fault trace and the field overview of tectonic landform and outcrop. (a) 3D view showing the active fault trace indicated by the fault scarps facing the uphill (see Fig. 6.1b for location). (b) Field photograph showing the fault scarps developed in a piedmont area. The white dashed line indicates the topographic surface slope. (c) Fault outcrop showing the formation of colluvial wedges bounded by the active faults (F1-F3), indicating a faulting event occurred in the period between 9125-8460 yr Cal BP from the samples of C11 and C09.

Fig. 6.5. Photographs showing the overview of tectonic landforms associated with the active strike-slip faulting. (a) Field photograph showing the faulted saddle geomorphology (see Fig. 6.3a for location). (b) Fault scarps facing the uphill. The red dashed line indicates the active fault trace, the same location as (a). (c) Photographs showing the fault scarps facing the upstream of gully (see Fig. 6.3c for location). (d) Push-up structure occurred on the alluvial fan deposits, the same location as (c).

Fig. 6.6. Field photographs showing the topographic features and the outcrop walls in Trench 1. (a) Field photograph showing the overview of faulted geomorphology characterized by the fault scarps developed on both flanks of gully with the sinistral displacement of ~10 m, the same location as Fig. 6.5c. (b) The frontal view of trench locations (see Fig. 6.3c for trench locations), a ~10 m left-lateral offset of gully was observed between these two trenches. (c) West wall of

Trench 1. (d) East wall of Trench 1. (e) Sketch of (c). (f) Sketch of (d).

Fig. 6.7. Field photograph and sketch of Trench 2. (a) Photograph and (b) the corresponding sketch of Trench 2. The sampling locations may not be exactly accurate due to the heavy snow, but the basic accuracy can be guaranteed.

Fig. 6.8. Photographs showing the deformational characteristics of the sedimentary units in Trench 2. (a) Graben structure developed between fault F2 and fault F3, causing the thickened accumulation of dark-grey organic soil and related alluvial deposits. (b) The extremely different color difference between the both sides of fault F3. (c) Injection veins filled by the grey to dark soil and the associated sampling locations. (d) The fault F3 bounded the alluvial deposits and basement rock. Foliation structures developed in the cataclasitic rock. The red dashed line indicates the foliation.

Fig. 6.9. Schematic diagram to explain the timing and processes of the paleoseismic events from E4 to E1. The thick fault line indicates the slipping fault when the paleoearthquake occurred. The dashed line represents the inferred boundary of sedimentary unit or topographic surface. The Numbers ①-⑪ represent the evolution stages of paleoseismic events including the deposition, erosion and faulting.

Fig. 6.10. The historic earthquakes occurred on WQLF (Earthquake Disaster Prevention Department of China Earthquake Administration catalogue (EDPDCEA, 1995). The red column indicates the paleoseismic event E1 occurred after AD1414–AD1479, the magnitude is inferred from the empirical relationship between the surface rupture length and the Magnitude (Wells and Coppersmith, 1994).

Chapter 7.

Fig. 7.1. Geodynamic model showing the active tectonic characteristics associating with the active flexural folding and faulting in the NE marginal zone of the Tibetan Plateau. Noting the left-stepping en echelon topographic divides separating the Yellow River drainage systems and the low slip rate of 2.0–2.6 mm/yr on WQLF. The focal mechanisms are from the Global Harvard CMT catalogue (http://www.globalcmt.org). GPS data shown by arrows are modified from Zhang et al. (2004) and the lithospheric structures are modified from Tapponnier et al. (2001) and Ye et al. (2015). The white dashed line indicates the axis of topographic divide.

Acknowledgments

I will start by thanking the members of my committee for their support, encouragement, patience, and guidance. I extend my sincerest gratitude to my supervisor Prof. Aiming Lin for his instructive advice, patient guidance and ongoing support during the process of Ph.D. courses and in the completion of this thesis. I cherish the opportunity to study in Japan offered by Prof. Lin and it is him who introduced me to the excitement of active tectonics and the palace of science.

Prof. Lin is an amazing and creative geologist and earthquake geologist, and simply put, my success as a geologic researcher would not be possible without his leadership, support and dedication to my work. He pushed me constantly to make progress to grow as a curious, critical and forward-looking researcher. Working with Prof. Lin, I learned the rigorous scientific logic and detailed processing of finishing one high-quality academic paper. I also learned how to focus on the scientific problems from big picture geologic problems, such as the tectonic evolution of the Tibetan Plateau to the smallest details like how to make a beautiful figure shown in the papers. In addition, Prof. Lin set a good example for very student of us. He is always working very hard and keeping a high passion for scientific research whenever it is. In countless late nights after 12 o'clock, when I planned to come back to my home, the light in Prof. Lin’ office is always on even at weekends that impressed me deeply.

My another two supervisors, Prof. Fukuda and Prof. Iwata who gave me great support and help during the final stage of my PhD course. It is my great honor and fortune to be a student advised by them.

My research was assisted by numerous individuals at Kyoto University. I want to express my appreciates to Akiyama-san, Yoshida-san, Satsukawa-san, Sugita-san and

Tsutsumi-san for their kindness and help during my three years period in Kyoto University. They helped organize and arrange my fieldwork in China and provided me a good logistical support that help ease my mind at work. I would also like to thank my classmates who shared my joy and pain together. Heartfelt thanks to Di Bian, Zahra Mohammadi Asl, Takafumi Nishiwaki, Bingcheng Liu, Hong Peng and Hayato Shimazu.

I also want to thank my professors and classmates who ever worked with me together in the institute of Geomechanics, Chinese Academy of Geological Sciences when I was a master student. Prof. Shuwen Dong, Jianmin Hu, Wei Shi and Jiaxi Yang were appreciated for their careness, support and encouragement during my stressful time and have taught me a lot about life. My classmates, Dr. Xiaobo Liu, Jiyuan Yan, Xiang Qin, Zixian Zhao and Yongzhi Cheng were deeply appreciated from my heart for their help work in the field no matter how terrible the weather was.

Deep appreciations also were given to the previous generation of Prof. Lin students that served as role models, including the Dr. Zhikun Ren, Gang Rao, Maomao Wang and Bing Yan. They have ever taught and discussed a lot of scientific problems and field outcrops with me, which helped me make progress quickly. They have made a great contribution in the field of active tectonics in China and still are playing an active and positive role in the stage of young geologists.

Then, I sincerely thank my family members including my parents, elder sister and brother for their selfless and ongoing devotion and understanding during my Ph.D. courses. My parents raised three of us with higher education by their hard work, which is not easy in the present-day China. My girlfriend Wang M gave me meticulous care and concern during the final stage of my Ph.D. course, which given me strong

motivation to finish the thesis conscientiously and carefully.

Finally, I want to express my sincerest respect and heartfelt thanks to every member from my defense committee including Prof. Fukuda, Prof. Iwata, Prof. Fukahata, Prof. Matsushi, Prof. Ikeda and Prof. Shimizu. Fukuda-sensei and Iwata-sensei, gave me the considerate careness and encouragement, and discussed the overall structure and scientific logic with me on the thesis. Matsushi-sensei, Fukahata-sensei, Ikeda-sensei and Shimizu-sensei guided me the concrete revision process from the major structure to the minor mistakes even the font size in the figures. Finally, Prof. Fukahata-sensei took a long time and great efforts to help me check and polish the English writing. The critical and constructive comments and suggestions provided by them have greatly improved the quality of the manuscript. Without their help, I couldn't make such progress. It is my great honor to have six professors to teach, to encourage, to help me to make this thesis become better and better. During the process of revision and presentation, I not only learn the new knowledge, but also the scientific faith and attitude that a researcher should keep in his/her life. I strongly believe that my future will certainly benefit from the new understanding on the nature of science. Sincerest appreciates to every defense committee member.

The research presented in this dissertation benefits from everyone's efforts mentioned above. For all of these efforts, I am deeply grateful.

Chapter 1. Introduction

1.1. The research history and status of the Tibetan Plateau

Orogenic belts created by continent-continent collision are perhaps the most dominant geologic features of the Earth surface (Dewey and Burke, 1973). The Qinling–Dabie–Sulu belt in central China, the Appalachian belt in North America, and the Ural Mountains in central Eurasia are some of the best examples with a length of thousands of kilometers along strike. A great deal of research works has been done to the genesis of these orogenic systems since the development of plate tectonics 50 years ago owing to the fact that the continent-continent collision is the most dominant and efficient process in forming the supercontinents.

The Tibetan Plateau, the youngest and most spectacular continent-continent collisional belt in the world, is famous for its high-altitude and complex geological, geomorphic, climatic and ecological processes. The uplift of the Tibetan Plateau is a result of the subduction and collision between the Indian Plate and the Eurasian Plate, and the uplift in turn caused enormous changes in topography, climate, drainage system and the geodynamic process (e.g., Molnar et al., 1993; Yin and Harrison, 2000; Tapponnier et al., 2001). It is this large-scale interaction between lithospheric deformation and atmospheric circulation that have played a critical role in shaping what the Tibetan Plateau looks like today.

The Himalaya–Tibetan orogeny and its neighboring regions in east Asia are ideal places and natural laboratory for the study of continent-continent collision and intracontinental deformation, especially for the relationship and interaction between active tectonics and tectonic geomorphology that can be demonstrated directly using the methods of neotectonic and active tectonic studies (Allen et al., 1984; Armijo et al.,

1989; Lin et al., 2002; Zhang et al., 2004; Yan and Lin, 2015). Further, the intracontinental deformation and its geodynamic mechanism have been the extensive research project for the past several decades in order to optimize the theory of plate tectonics (Sengör and Kidd, 1979; Chen et al., 2000; Thatcher, 2007; Royden et al., 2008; Harkins et al., 2010; Li et al., 2018).

The ongoing penetration of India into Eurasia has driven the upward and outward expansion of the Tibetan Plateau since 50 Ma (Beck et al., 1995). The northeastern marginal zone of the Tibetan Plateau, as the frontal edge of plateau outward growth, occupies a transition zone between the high-elevation thick crust (> 45 km) and the low-elevation thin crust (< 45 km) of adjacent cratons (Ye et al., 2015), making it an ideal location to determine the interaction between active tectonics and geomorphology (e.g., Tapponnier et al., 1982; Burchfiel et al., 1991; Hubert-Ferrari et al., 2007).

Our knowledge and understanding of the growth of the northeastern margin of the Tibetan Plateau has progressed immensely over the past decade (Yuan et al., 2013). Previous study suggested that the earliest response of the northeastern Tibetan Plateau to the collision of Himalaya orogeny is Pliocene–Holocene time (Meyer et al., 1998), but the Eocene initiation was suggested by recent works (Yin et al., 2002; Clark et al., 2010), progressing through the Oligocene–early Miocene and accelerating in middle Miocene–Holocene time (Fang et al., 2005; Craddock et al., 2011).

1.2. Geodynamic models about the tectonic deformation of the Tibetan Plateau

In contrast to the Early Cenozoic deformation dominated by structural shortening, the modern tectonic deformation in the northeastern Tibetan Plateau is more complex since the recognition of active strike-slip faults (Molnar and Tapponnier, 1975). How did the

Tibetan Plateau deform in response to the collision between the Indian Plate and Eurasian Plate remains enigmatic and subject to debate; hypotheses have appealed to rigid plates or blocks (e.g., Tapponnier et al., 2001), continuous deformation of the entire lithosphere (Holt et al., 2000; Houseman and England, 1993), and channel flow in the lower crust or mantle (Royden et al., 1997) to provide keys to the understanding of deformation mechanisms.

Based on the above theories and hypotheses, two endmembers of the northeastern Tibetan deformation during the ongoing Cenozoic continental collision have focused on the question whether the plateau material was extruded along the major strike-slip faults with large horizontal displacement of up to hundreds to thousands of kilometers (e.g., ATF; KLF, WQLF and HYF; Tapponnier et al., 1982; 2001) or the strain energy was mostly absorbed by the more broadly distributed deformation dominated by crustal shortening and thickening (England and Houseman, 1986). The model of tectonic escaping thought that the plateau deformation is dominated by the eastward strike-slip motions of rigid blocks along the first-order active strike-slip faults, which stressed the strong local deformation along the active strike-slip fault zones and is characterized by the non-continuous deformation. In contrast, other researchers argued that the uplift and deformation in the Tibetan Plateau was mainly controlled by crustal shortening and thickening, a diffused and continuous deformation style at the three-dimensional spatial space (Houseman and England, 1993; Zhang et al., 2004). This mode places more emphasis on the tectonic shortening and continuous deformation throughout the lithosphere.

One of the important causes that leads to the disagreement between the above two modes is the lacking of quantitative evaluations of strain energy absorbed by the lateral

strike-slip motions and structural shortening, respectively. Neotectonic and active tectonic studies have provided some illumination to this controversy. The tectonic extrusion model was supported by the high strike-slip rates along the Altyn Tagh Fault (e.g., Molnar et al., 1987; Peltzer et al., 1989), the western and central segment of Kunlun Fault (Kidd and Molnar, 1988; Lin et al., 2006) and the Ganzi–Yushu–Xianshuihe Fault (Yan and Lin, 2016). However, recent studies in the past decade report that the left-lateral slip rate of the Kunlun Fault diminishes toward the east at an average gradient of 1 mm/100 km from larger than 10 mm/yr in the western and central segment to ~3 mm/yr at its eastern tip (Kirby et al., 2007; Lin and Guo, 2008). The Haiyuan Fault and West Qinling Fault also behave at a low left-lateral slip rate of ~4.5 mm/yr and 2.3 mm/yr in the northeast, respectively (Li et al., 2007, 2009). Between the Kunlun Fault and the Haiyuan Fault, many minor thrust faults and strike-slip structures striking both NW–SE and NE–SW developed in the study region also display a characteristically low slip rates (Zheng et al., 2016).

1.3. The targets and research purpose

The indentation of the Indian plate into the Eurasia has driven the upward and outward growth of the Tibetan Plateau since ~50 Ma (Beck et al., 1995; Yin and Harrison, 2000), shaping the world's largest topographic perturbation. The kinematics and dynamics of plateau deformation can be studied by revealing the position, extent and topography of elevated terrains during the growth of the Tibetan Plateau (Tapponnier et al., 2001; Royden et al., 2008), especially for the plateau margins, which is suffering from the strongest active tectonic deformation with pronounced topographic, climatic and tectonic gradients (Yin and Harrison, 2000).

However, the constraints on the characteristics of active tectonic deformation, as well the associated tectonic geomorphology are still poor. Even the slip rate and the recurrence interval of large earthquakes of the West Qinling Fault, one important regional-scale strike-slip fault in the northeastern Tibetan Plateau, remain unclear, which seriously hinder the understanding on the plateau expansion and geodynamic mechanism. Therefore, the thesis focuses on the active tectonics of the northeastern Tibetan Plateau, which will help provide qualitative and quantitative evaluation into the problem mentioned above.

Two major research works have been conducted and analyzed in this thesis. The first part is shown in Chapter 4, in which the topographic divides that separate the Yellow River and its main tributaries were identified based on the extraction of drainage systems developed in the northeastern Tibetan Plateau. The processing of digital elevation model (DEM) data, interpretations of high-resolution remote sensing images and detailed field outcrop investigations reveal that these topographic divides formed by tectonic uplifting and folding in response to the ongoing northeastward shortening of the plateau accommodating the Eurasia–India continental collision.

The second part is a comprehensive study on active faults, including the related tectonic geomorphology, Late Pleistocene activity, slip rate and seismic recurrence characteristics on the WQLF, one of the main active strike-slip faults developed in the northeastern Tibetan Plateau.

In Chapter 5, work that is mainly concerning with the topographic analyses and field investigations on the Late Quaternary activities of the WQLF has been done. The topographic and drainage system responses related with strike-slip faulting of the WQLF were interpreted and analyzed; systematic offsets and deflections of stream

channels along the WQLF, as well as the maximum cumulative offset recorded by some tributaries of the Yellow River were displayed and summarized. Furthermore, the horizontal slip rate of the WQLF was estimated based on the deformation features of young river terraces and radiocarbon dating results.

In Chapter 6, the paleoseismic events along the WQLF were also studied through the trench excavations and radiocarbon dating. Three or four large earthquakes occurred during the past ~9000 years on WQLF, suggesting an average recurrence interval of large earthquakes of 2250–3000 years.

In Chapter 7, crustal deformation models for the Tibetan Plateau and the active tectonic implications of this study to the northeastern Tibetan Plateau have been discussed. The active tectonic deformation in the northeastern Tibetan Plateau was suggested to be dominated by the ubiquitous crustal shortening and partially partitioned by limited strike-slip displacement along the major strike-slip faults associated with the active folding and faulting in the northeastern marginal zone of the Tibetan Plateau.

In Chapter 8, The main research achievements and conclusions obtained in this study are summarized, which will continually help and guide my future research work.

Chapter 2. Studying methods

2.1. Interpretations of Remote sensing images and DEM processing

In order to understand the most recent activity of active faults and reveal the recurrence characteristics of large earthquakes, the precise interpretation of high-resolution remote sensing images is a prerequisite for guiding the field investigations and assessing the geomorphic features altered by the active faulting and fault folding. A rational interpretation of topographic images not only helps improve the field work efficiency, but also can provide a perfect indicator of tectonic geomorphology related with active tectonics. In this study, the traces of active faults, active flexural fold structures and associated tectonic geomorphology were identified from interpretation of remote sensing images including ASTER GDEM (30-m-resolution)，SRTM 90 m (90-m-resolution), STRM30 (1-km-resolution) released by Earth Remote Sensing Data Analysis Center (RESDAC) and United States Geological Survey (USGS) and Google Earth imagery.

The unrelenting competition between tectonic process that tend to build topography and surface process that tend to tear them down represents the core of tectonic geomorphology. Sharp contrasts in the appearance of landscapes in a given climatic or tectonic regime inspired the curiosity to explore these contrasts.

Present-day geomorphology, with its constituent processes of analyses and measurement of deflected and/or offset topographical surface markers, is highly effective for revealing the records of the deformation process and accumulated displacement along active faults. Hence, these topographical surface markers are regarded as a kind of “paleoseismic fossil”, which record the fault slipping events (e.g., Koons, 1995; Lin and Guo, 2008; Yan and Lin, 2016;). In tectonic geomorphology, an

identifiable feature that has been displaced is a prerequisite before determining and measuring the amount of deformation that has been accumulated along the active faults or preexisting fault-related structures due to the repeated seismic slipping. The pre-deformational morphology and geometry of a geomorphic marker has to be reconstructed accurately in order to calculate the displacement and compare the topographic difference caused by the tectonic process. The best geomorphic markers which can be used as a reference frame against which to gauge the absolute deformation should meet the following criteria: 1) an undeformed initial geometry; 2) a known or dateable age; 3) high preservation potential with respect to time scale of the tectonic process being studied (Burbank and Anderson, 2012). Due to the erosion and/or deposition, the presently exposed appearance is only a fragment of formerly continuous surfaces, which demands the pre-deformational geometry of a geomorphic feature must be defined. Therefore, a reliable and precise reconstruction process of the pre-deformational geometry and morphology is crucial to calibrate tectonic deformation amount.

Generally, two types of geomorphic markers comprising the planar and linear geomorphic features were widely utilized to interpret and assess the deformational characteristics of active faults and folds as illustrated by Fig. 2.1, which are also the cores of remote sensing image interpretations. In the northeast marginal zone of the Tibetan Plateau, the target area of this study, these tectonic geomorphic features associated with the left-lateral strike-slip faulting have also been observed in the field, the details are described in Chapter 4 and Chapter 5.In contrast with the two-dimensional planar geomorphic markers represent regionally extensive surfaces, the linear geomorphic and man-made features is another type of topographic markers

applied to determine deformation characteristics of active faults. The linear geomorphic features such as the stream channel and mountain ridge can provide ideal piercing point from which an offset can be unambiguously measured.

Drainage system, as one of most applied geomorphic features, which is sensitive to active faulting and folding, is the best indicator to restore the deformational process and assess the active characteristics of active faults. The systematic deflection and/or offset along intracontinental strike-slip faults have long been recognized as the most important and reliable geomorphic markers for understanding the deformational features of active strike-slip faults (Matsuda, 1975; Maruyama and Lin, 2000, 2002; Yan and Lin, 2015).

Systematic deflection and/or offset of drainage systems along the strike-slip faults is a result of repeated fault slipping cumulated on the stream channels. The analyses and measurement of offset amount of drainage systems will enhance our understanding of deformational behaviors of strike-slip faults and advance the relationship between the topographic response and active faulting. For example, Yan and Lin (2015) reported that the maximum accumulated offset recorded by the Yangtze River and its tributaries along the Ganzi–Yushu–Xianshuihe left-lateral strike-slip fault is ~60 km accumulated in the past 13–5 Ma in the southeastern margin of the Tibetan Plateau. Similarly, the maximum displacement amount of drainage systems in the northeastern marginal zone of the Tibetan Plateau has been studied and reported in the thesis. The details are documented in Chapter 4.

Besides the large-scale lateral displacement, the most recent tectonic deformation generally was also recorded by miniature rivers or gullies with a short upstream length varying tens to thousands of meters. The systematic offset and deflection of stream channels with a relatively short upstream length along the WQLF will be demonstrated

in Chapter 5 in detail.

When utilizing these geomorphic markers comprising the planar and linear geomorphic features, the restoration and reconstruction of the pre-deformed morphology of the markers is the basis for all interpretations of deformation. Different geomorphic markers such as the terrace and alluvial fans generally have some predictable geometries according to their structural features and space-time evolution patterns. Furthermore, different kinds of deformational styles of faults and folds often display distinctive surface deformation and geomorphic responses.

The reconstruction of 3D perspective images which highlights the vertical relief of topographic surfaces will help us understand the present-day geomorphic evolution results resulting from the active tectonic process. Generally, the vertical scale could be exaggerated by different times to put more emphasize on the topographic relief (Fig.2.2). The method is highly effective in places where the fault scarps develop with the vertical offset, especially when the offset amount is relatively small. The reconstruction process can be implemented by draping the remote sensing images onto DEM data through the using of Envi tool, which is also available in Google Earth for 3D perspective.

2.2. Field investigation and trench excavation

After finishing the remote sensing interpretations, the active tectonic deformation comprising the active faulting and folding need to be further checked and verified. The processes of fieldwork also help analyze the active characteristics of active faults, the geomorphic appearance, and the paleoseismic events revealed by field outcrops and trench excavations.

For the conventional fieldwork for the research of active tectonics, the first is to

ascertain the main traces of active faults integrating the results of remote sensing interpretations. Fault outcrops and tectonic geomorphology associated with the active faulting and folding are the basic evidences for determining the fault traces. The results of field investigation will be explained in the Chapter 4 and Chapter 5 in detail. Here, we want to make brief introduction for the trench excavations and paleoseismic investigation.

The most direct way to expose the geologic features related with paleoseismic faulting events is to excavate trenches across the active fault (Sieh, 1978). The purpose of trench excavations is to find evidences of fault slipping recorded in the near-surface deposits and topographic relief. Large and shallow earthquakes disrupt and displace geomorphic features and stratigraphic units, leaving information of fault slipping and provide a chance to analyze the paleoseismic events (Wallace, 1968; Agnew and Sieh, 1978). The information can be preserved over many seismic recycles, enabling investigations into the recurrence characteristics of surface rupturing earthquakes. However, it must be realized that the uniqueness of each trench even excavated across the same fault. The detailed interpretations and analyses of trench wall exposures are critical to determine the timing of paleoseismic events and recurrence interval of large earthquakes (Sieh, 1978; Wesnousky et al., 1991; Lin and Guo, 2008). Structural and stratigraphic features associated with the faulting are commonly used to identify the occurrence of large paleo- and historical-earthquakes. The information includes the displacement of sedimentary strata, disturbance of water-laid sediments, the upward termination of fault planes and the presence of infilled fissures and scarp-derived colluviums and so on (Lin and Guo, 2008; Rao et al., 2016). The basic criterion for identifying the paleo-earthquakes is similar to the principle of traditional structural

geology based on the cross-cutting relationships and the stratigraphic sequence.

In this study, several basement trenches have been excavated for identifying the paleoseismic faulting events. Tens of organic samples from trench walls and outcrops were collected for radiocarbon dating. Time scale of 50k yr BP and uncertainty of several decades are sufficient to reveal the recurrence intervals varying from hundreds to thousands of years during Late Quaternary period. The details are described in Chapter 4.

2.3. Radiocarbon dating technique

During the past decades, a great progress has been made for determining the formation ages of geomorphic markers and further evaluating the mechanisms and rates of surface process. Today, with the availability of dating techniques, it is possible to measure how rapidly a given site is moving with respect to another and how those rates are partitioned among various faults and folds. In the field of active tectonics and tectonic geomorphology, the principal means of determining the deformational rate and establishing the timing of topographic evolution, as well as defining the paleoseismic events was mainly through the use of relative dating methods until the advent of radiocarbon dating methods. The absolute dating permits us to place a number on the formation ages of geomorphic features and geological markers.

The radiocarbon dating is the most commonly used method to date geomorphic surfaces that are less than 40–50 ka due to carbon-14 half-life of 5730±40 years (Olsson, 1968).

The quantitative evaluation of how rapidly deformation has occurred in the past, and how the shortening rate and strike-slip rate were partitioned in the northeastern marginal

zone of the Tibetan Plateau during the process of plateau expansion. When the deformation amount is combined with rates benefiting from datable geomorphic markers, the three-dimensional reconstruction of tectonic evolution and surface process can be attained.

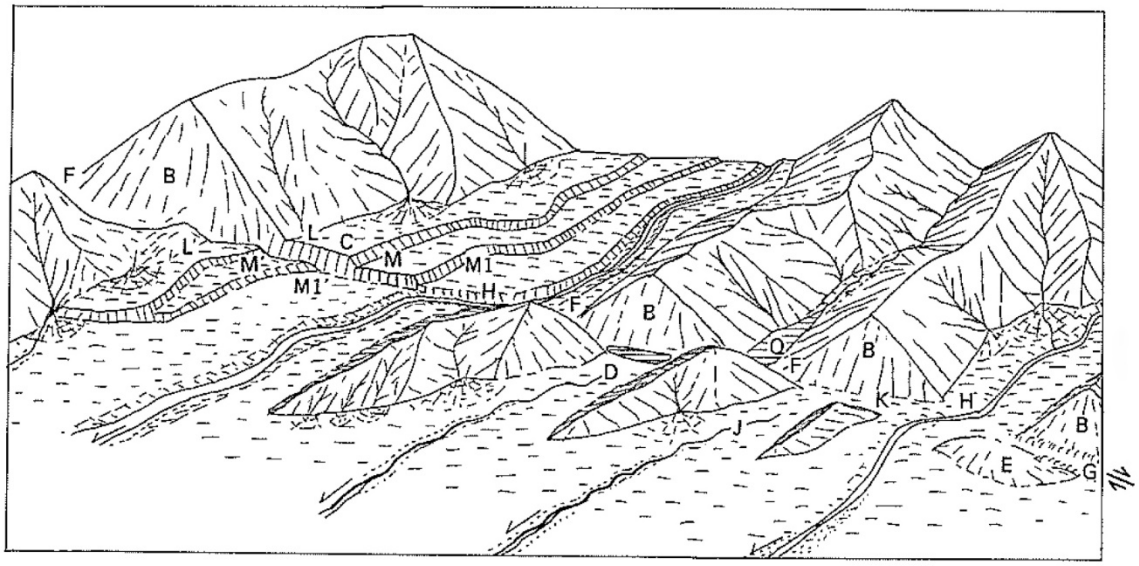

Fig. 2.1. Tectonic geomorphic features formed by active strike-slip faulting (cited from the Research Group for Active Faults of Japan, 1991). The alphabets are defined as follows: B: fault triangular facet; C: fault scarp facing the downstream; D: sag pond; E: tectonic bulge or push-up structures; F: fault saddle; G: graben structure; H: offset stream channel; I: shutter ridge; J: beheaded stream; K: wind gap; L–L´: offset piedmont line; M–M´: offset higher terrace; M1–M1´: offset lower terrace; Q: sag pond.

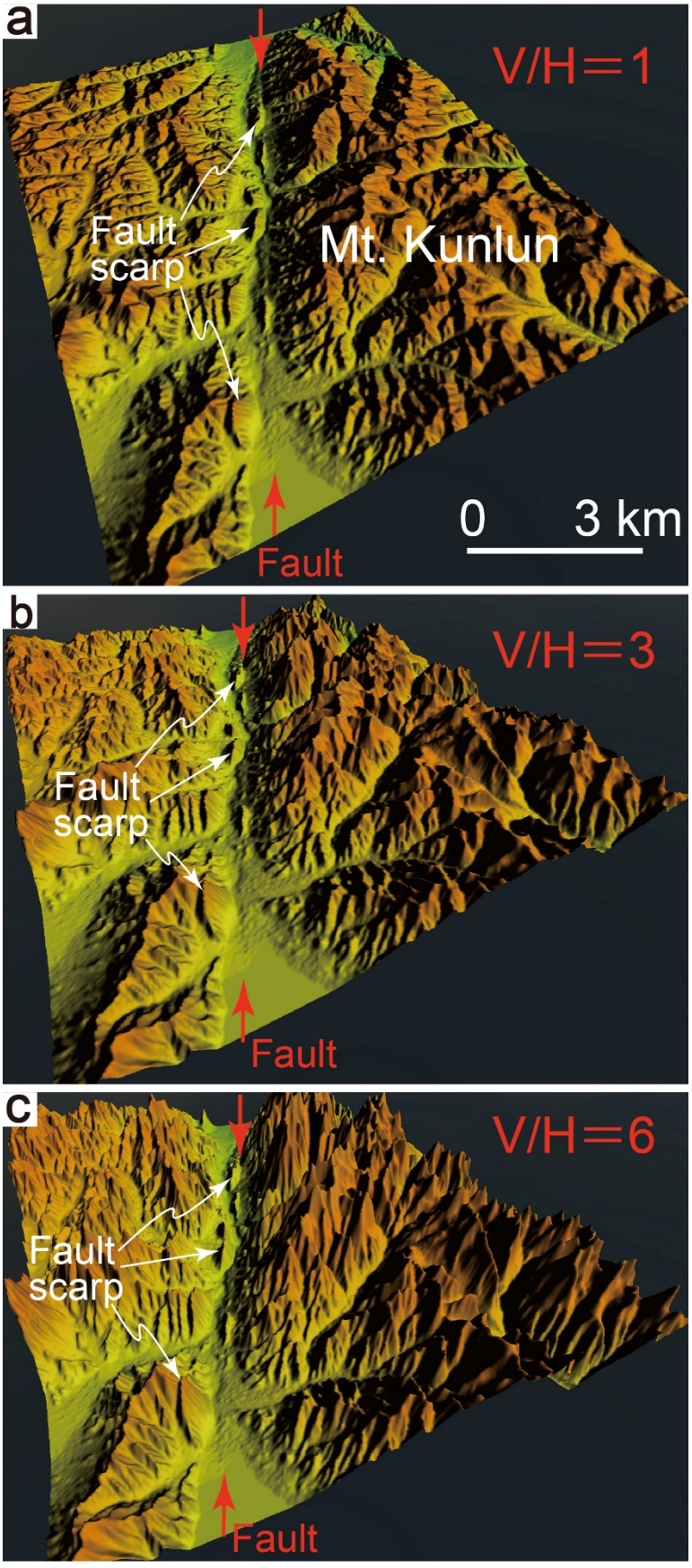
a
V/H=1
Fault
scarp
Mt. Kunlun
0
3 km
Fault
b
V/H=3
Fault
scarp
Fault
c
V/H=6
Fault
scarp
Fault

Fig. 2.2. 3D topographic images showing the fault scarps developed along the Kunlun Fault by exaggerating the topographic relief in vertical scale. The V/H means the vertical scale versus the horizontal scale. (a) V/H＝1. (b) V/H＝3. (c) V/H＝6.

Chapter 3. Tectonic setting

3.1. Tectonic evolution of the NE Tibetan Plateau

The Tibetan Plateau, the “Roof of the World”, takes up for approximately 3 million square kilometers with an average elevation of ca. 4000–5000 m (Fig. 3.1). It has been widely accepted that the plateau formed as a result of collision between the Indian and Eurasian plates (e.g., Yin and Harrison, 2000; Tapponnier et al., 2001). The geologic and topographic evolution of the Tibetan Plateau is also thought to have played a critical function in adjusting the global climate change due to the tremendous topographic uplift (e.g., Ruddiman and Kutzbach, 1989; Molnar et al., 1993; Ramstein et al., 1997). In turn, the climate change may have affected the erosion rate and thus altered the topography pattern on a long-time scale (e.g., Avouac and Buron, 1996., Lease, 2014). It is the large-scale and long-term interaction between the lithospheric deformation and the surface process that makes greater significance on the formation and evolution of the present-day Tibetan Plateau, which constitutes the core of earth system science.

The Tibetan Plateau is composed of multiple terranes that successively accreted to the Asian plate (Fig. 3.2; Dewey et al., 1988). The northernmost Qaidam–Qilian Terrane is separated from the Tarim–North China Block along the North Qilian suture that formed during the early Silurian to Middle Devonian (Song et al., 2006). Southward, the Qaidam–Qilian terrane is separated from the Songpan–Ganzi Terrane along the Kunlun suture from the early Permian to Middle Triassic (Yang et al., 1996), and the subsequent Qiangtang Terrane, Lhasa Terrane is blank off from the Songpan–Ganzi and Qiangtang Terrane by the Jinsha suture and Bangong suture, respectively (Wang et al., 2000; Guynn et al., 2006). Finally, the Indus–Zangbo suture divides the Lhasa Terrane from the Peninsular India block (Yin and Harrision, 2000).

Understanding how the Tibetan Plateau was constructed greatly affects our knowledge of plate tectonics and intracontinental deforamtion (Molnar, 1988; Yin, 2010). Three end-member models for plateau formation and evolution have been summarized as: 1) Continuous Cenozoic underthrusting of the Indian and shortening and thickening (Dewey and Burke, 1973; England and Houseman, 1986), This model provided a plausible mechanism to explain both the double crustal thickness of Tibet and surface uplift of the Plateau. However, the complex tectonic deformation comprising the folding and thrusting developed on the Proterozoic to Holocene rocks was ignored; 2) Discrete Cenozoic intracontinental subduction coupled with lateral extrusion along the major strike-slip faults (Tapponnier et al., 1982, 2001). They proposed ~1000 km of right-lateral motion along the Karakoram Fault and ~500 km of left-lateral slip along the Altyn Tagh Fault, but the scale of tectonic extrusion is always doubted (e.g., Yin and Harrison, 2000; Cowgill et al., 2003); 3) Channel flow in the lower crust or lithospheric mantle (Bird, 1991; Clark and Royden, 2000; Royden et al., 2008). The model proposed that the lower crust is very weak and is decoupled from both the upper crust and the upper mantle. However, no consolidated geological and geophysical evidence show that the middle or lower crust is flowing as predicted by this model.

Among these models, some contradicts are still existing, which place a big doubt on the geodynamic process of the Tibetan Plateau. For instance, how the shortened crust was partitioned between lateral extrusion and crustal thickening, and the spatiotemporal evolution of such strain partitioning remain controversial (Wright et al., 2004; Yang and Liu, 2009). The predictions of the lower crustal flow were initially supported by east-west horizontal crustal shortening across the Longmenshan along the eastern

margin of the plateau (Burchfiel et al., 1995). However, recent seismic reflection analyses and balanced cross-section result indicate that the crustal shortening alone in the eastern margin is enough to generate the crustal thickness and elevation without the role of lower crustal flow (Hubbard and Shaw, 2009). The profound research of Cenozoic tectonic deformation, especially the active tectonics in the northeastern marginal zone of the Tibetan Plateau will provide a quantitative and diagnostic test for examining these tectonic models.

The northeastern Tibetan Plateau, as the frontal belt of outward expansion of the Tibetan Plateau, occupies a transition zone between the high-elevation thick crust (>65 km) of the central plateau and the low-elevation thin crust (<45 km) of adjacent cratons such as the Ordos massif (Ye et al., 2015). Understanding of the tectonic evolution of the northeastern Tibetan Plateau has greatly benefited from the previous research over the past decade (Yuan et al., 2013). The original response to the continental collision in the northeastern Tibet was suggested to start in the Eocene as an almost simultaneous feedback (Yin et al., 2002; Clark et al., 2010), progressing through the Oligocene–Early Miocene (Fang et al., 2003) and accelerating in the Late Quaternary period (Craddock et al., 2011).

The modern deformation in the northeastern Tibetan Plateau is more sophisticated in contrast to the north–south crustal shortening due to the strike-slip faulting. The large-scale strike-slip faults distributed in the plateau interior and its margins arose debate that the plateau material whether were extruded eastward (Tapponnier et al., 1982) or participate in more diffused deformation (England and Houseman, 1986). Six major active strike-slip fault are lying the interior and margins of the plateau, arranging in the order of the Altyn Tagh Fault, Kunlun Fault, Haiyuan Fault, West Qinling Fault,

Longmenshan Thrust Fault and Ganzi–Yushu–Xianshuihe Fault (Fig. 3.1).

3.2. Regional geology of the study area

In geological structure, the NE plateau is composed of northwest-trending strike-slip fault-bounded ranges and intermontane basins at a spatial interval of 30–40 km. The geophysical receiver function and seismic reflection section revealed that the crustal thickness across the area varies from 55 to 65 km (Gao et al., 2013; Ye et al., 2015). However, the Ordos Block, a relatively stable block with far fewer earthquakes, has a crustal thickness of ~40 km (Ye et al., 2015). The abrupt changes in topographic relief and crustal thickness place more attention on this studying area, which will help uncover the geodynamic mechanism of plateau growth.

The northeastern Tibetan Plateau has a complex pre-Cenozoic tectonic evolution involving multiple phases of deformational history comprising the Proterozoic basement deformation and metamorphism, early Paleozoic orogeny, Jurassic–Cretaceous extension and Cenozoic tectonic shortening and left-lateral shearing (Yin and Harrison, 2000; Yuan et al., 2013).

The early Paleozoic Qilian–Haiyuan orogeny recorded the mircrocontinent collision process between the Kunlun–Qaidam massif and the southern margin of the North China craton marked by the closure of the Qilian Ocean (Yin and Nie, 1996; Song et al., 2013). The basement of the Qilian–Haiyuan orogen is composed of Silurian flysch sedimentary sequences, Ordovician–Silurian plutonic bodies, ophiolitic mélange, and low- to high-grade metamorphic rocks (Gansu BGMR, 1989). The Jurassic and Cretaceous extensional setting is expressed by the occurrence of extensional and transtensional basins in the northeastern marginal zone of the Tibetan Plateau (Chen et

al., 2003; Yin and Harrison., 2000). These basins were filled by widespread terrestrial sedimentation that transformed from marginal marine and lacustrine strata. The terrestrial strata are characterized by the composition of red sandstone interbedded with siltstone and shale (Fig. 3.3, Gansu BGMR, 1989; Qinghai BGMR, 1989).

The Cenozoic tectonic deformation is mainly accommodated by the crustal shortening and material lateral extrusion along the large-scale strike-slip faults within and surround the Tibetan Plateau. The strike-slip faults, which play a critical role in partitioning and accommodating the strain energy and deformational style. Five major large-scale active strike-slip faults are lying the interior or margins of the Tibetan plateau, including the Altyn Tagh Fault, Haiyuan Fault, West Qinling Fault, Kunlun Fault and Ganzi–Yushu–Xianshuihe Fault southward, respectively (Fig. 3.1).

The Altyn Tagh Fault, one of the largest active strike-slip faults in the world with a length of ca.2000 km, defines the northern edge of the Tibetan Plateau (Fig. 3.4b). The fault has been regarded as either a crustal-scale transfer linking thrust belts (Burchfiel et al., 1989) or a lithospheric-scale strike-slip fault accommodating eastward extrusion of the Tibetan Plateau (Wittlinger et al., 1998). The slip rate along the active, left-slip Altyn Tagh Fault has been disputed for more than two decades. The effort has yielded slip rates along the fault that vary by almost a factor of three among the Global Positioning System (GPS) velocity field (Wang et al., 2001), slip rates at Late Quaternary time scales using displaced geomorphic features (Mériaux et al., 2004; Chevalier et al., 2005), and that inferred from interferometric synthetic aperture radar (InSAR) data (Jolivet et al., 2008). The largest slip rate of the Altyn Tagh Fault during Holocene period was suggested to be 20–30 mm/yr based on the landform reconstructions of offset river terrace along the central segment (Mériaux et al., 2004),

though the slip rate decreases to ~4 mm/yr at the tip of eastern Altyn Tagh Fault (Cowgill et al., 2009). The geological and historical large earthquakes have repeatedly occurred along the Altyn Tagh Fault characterized by the coseismic surface rupture reported by the previous documents (State Seismological Bureau, 1992). However, what is worth noting is that these large earthquakes with M≥ 6.5 documented along the Altyn Tagh Fault since A.D 1785 occurred only along the westernmost part of the fault. The Yutian M_w 7.1 and M_w 6.9 occurred in 2008 and 2014 produced 31-km-long and 28-km-long coseismic surface rupture zone, respectively (Xu et al., 2011; Li et al., 2015). Another pair of earthquakes with magnitude of M_s 7.2 inferred from the building damage also occurred at the westernmost segment of the Altyn Tagh Fault in 1924. Whereas, there are barely large earthquakes ever occurred at the eastern Altyn Tagh Fault. In this paper, in order to uncover the active tectonic deformational characteristics of the eastern segment of Altyn Tagh Fault, the high-resolution remote sensing images and tectonic geomorphology related with the active faulting and flexural-folding were interpreted and analyzed.

The Kunlun Fault, the seismogenic fault of the 2001 M_s 8.1 central Kunlun earthquake, is located in the Kunlun mountain area with an average elevation of more than 4500 m in the northern Tibetan Plateau (Fig.3.4c). The Kunlun fault strikes east–west to west-northwest–east-southeast with a length of >1200 km and is considered as one of the major strike-slip faults along which strike-slip partitioning occurs in accommodating the northeastward shortening and eastward extrusion of the Tibetan Plateau (Meyer et al., 1998; Lin et al., 2002). The 2001 M_s 8.1 Kunlun earthquake generated a nearly 400-km-long strike-slip surface rupture zone with a lateral offset up to 16.3 m along the pre-existing strike-slip Kunlun Fault, in which the rupture length

and maximum displacement produced by individual large earthquake both are the largest value among the coseismic surface rupture zones ever reported in intracontinental earthquakes (Lin et al., 2002). The Kunlun Fault exhibits gradient strike-slip rate across the different segments, varying from 10–20 mm/yr in the west to ~3 mm/yr at the tip of its eastern segment (Lin et al., 2006; Lin and Guo, 2008). The non-uniform along strike-slip rate of Kunlun Fault indicates a diminishment toward the east at an average gradient of 1 mm/100 km (Lin and Guo, 2008).

The Haiyuan Fault, the seismogenic fault of the 1920 M 8.5 Haiyuan earthquake, lies to the east of the North Qilianshan Fault and to the west of Liupanshan Fault on the northeastern margin of the Tibetan Plateau. The 1920 M 8.5 Haiyuan earthquake generated a 237-km-long surface rupture zone with a maximum left-lateral strike-slip displacement of 10.5 m (Institute of Geology, SSB, 1990). The Haiyuan Fault became active expressed by the thrust faults and related folds developed in the Pliocene strata, and transformed into a dominated left-lateral strike-slip fault in the Late Pliocene or Early Pleistocene (Burchfiel et al., 1991). The slip rate of the Haiyuan Fault has been reported based on different manners involving the interferometric synthetic aperture radar (Wang et al., 2003), Global Positioning System (Zhang et al., 2004) and LiDAR (Chen et al., 2014). Currently, the widely accepted geological slip rate of the Haiyuan Fault is reported to be 4.5 mm/yr based on the terrace evolution analyses (Li et al., 2009). A millennial recurrence interval was also achieved from 19 trench result across the fault (Zhang et al., 1988b).

The Ganzi–Yushu–Xianshuihe Fault, striking WNW–ESE in the northwest and NNW–SSE in its southeastern section, has a geometry of an arc projecting northeastwards. The fault extends from the central part of the plateau, through the

eastern margin into the Yunnan–Guizhou plateau. At least 14 large earthquakes of M≥7.0 have occurred along the fault in the past 700 years based in the historical records, including the 2010 M_w 6.9 Yushu earthquake (Rao et al., 2011). The maximum accumulated displacement along the Ganzi–Yushu–Xianshuihe Fault recorded by the Yangtze River and its tributaries was reported to be ca. 60 km, and the long-term average strike-slip rate is 4.6–12 mm/yr (Yan and Lin, 2015).

The West Qinling Fault, striking WNW–ESE, is a dominated left-lateral strike-slip fault bounding the topographic boundary between the West Qinling Range and Longzhong basin, the previous research focusing on the West Qinling Fault are quite insufficient with very few publications, the active characteristics of this fault including the related tectonic geomorphology, slip rate and paleoseismic events are discussed in detail in Chapter 5 and Chapter 6.

3.3. Topographic features

The present-day high elevation of the Tibetan Plateau was suggested to be the result of the Inidan–Eurasian collision (Yin and Harrison, 2000). The northeastern Tibetan Plateau is slightly lower (~4 km) and then drops rapidly to the northeast in the Hexi Corridor foreland and Ordos (Fig. 3.1). The topographic transition from the high-elevation low-relief interior to moderate-elevation high-relief margins is a characteristic feature of the Tibetan Plateau, which provides a window to understand how low-relief plateau is formed.

The northeastern plateau, north of the Kunlun range and Qaidam basin and south of the Hexi corridor and Gobi-desert, composed of roughly parallel ranges and intermontane basins (Fig. 3.1). The growing folds and active thrust or strike-slip faults

usually divide the ranges and basins. Due to the arid to semiarid climate, the drainage network is not well developed in this area. Most rivers flow parallel to the orientation of mountain ranges, a few rivers drain north into the Hexi Corridor and Ala Shan platform. The Yellow River, as an externally drained river, penetrates into the northeasternmost part and developed a large rectangular square bend around the Ordos block (Lin et al., 2001).

Detailed topographic analyses of the northeastern Tibetan Plateau are rare, but have significant potential to understand the plateau landscape evolution. Previous researches have focused primarily on the Hexi Corridor north of the Qilian Shan, and the regional uplift and erosion rates (Champagnac et al., 2010; Palumbo et al., 2011). Analyses of the longitudinal profiles of bedrock channels revealed systematic differences in the channel steepness index along the trend of the frontal ranges, indicating a result of differential rates of rock uplift (Hu et al., 2010). The recent study proposed a “bathtub” basin-filling model that played the important role in smoothing out the structural relief across the northeastern marginal zone of the Tibetan Plateau generated by the tectonic process (Liu-Zeng et al., 2008). An important topographic feature in the local relief distribution is that the larger local relief is localized along the plateau rim. On the contrary, the relief is smaller toward the areas away from this rim, such as the Qaidam and Gonghe basin, though with a generally high elevation. The fact that the low relief and high elevation inside the plateau suggests that relief reduction has outpaced the relief growth by tectonic uplift at a rate during the process of interactions between tectonism and surface erosion.

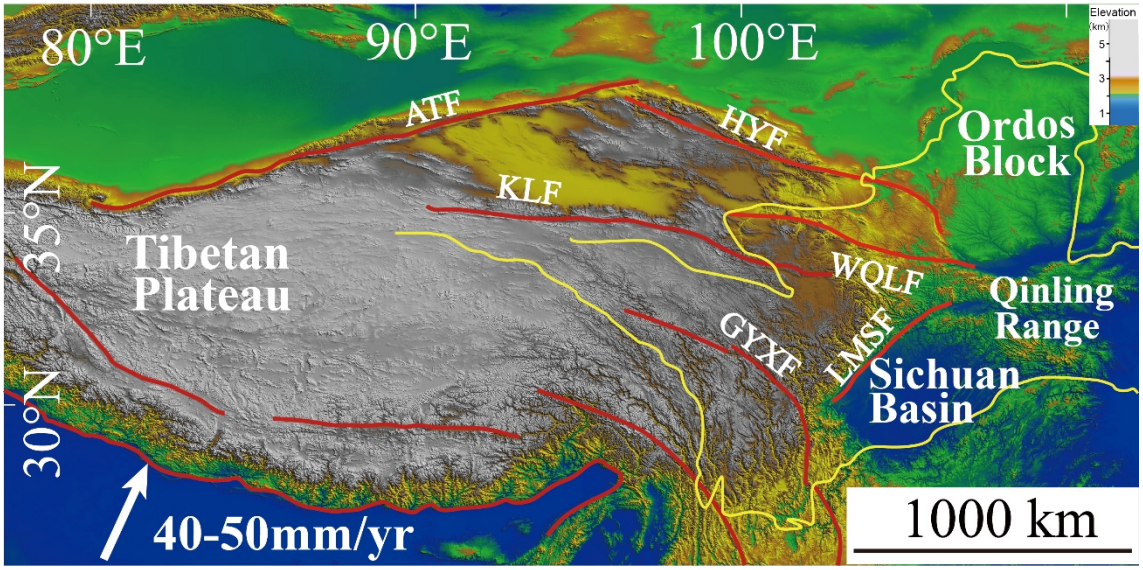

Fig. 3.1. Color shaded-relief map generated from SRTM 30 PLUS (Shuttle Radar Topography Mission, 1-km-resolution) showing the topographic features of the Tibetan Plateau and adjacent area. The main active faults were labeled with the acronyms defined as follows: ATF: Altyn Tagh Fault; KLF: Kunlun Fault; HYF: Haiyuan Fault; WQLF: West Qinling Fault; LMSF: Longmenshan Fault; GYXF: Ganzi–Yushu–Xianshuihe Fault.

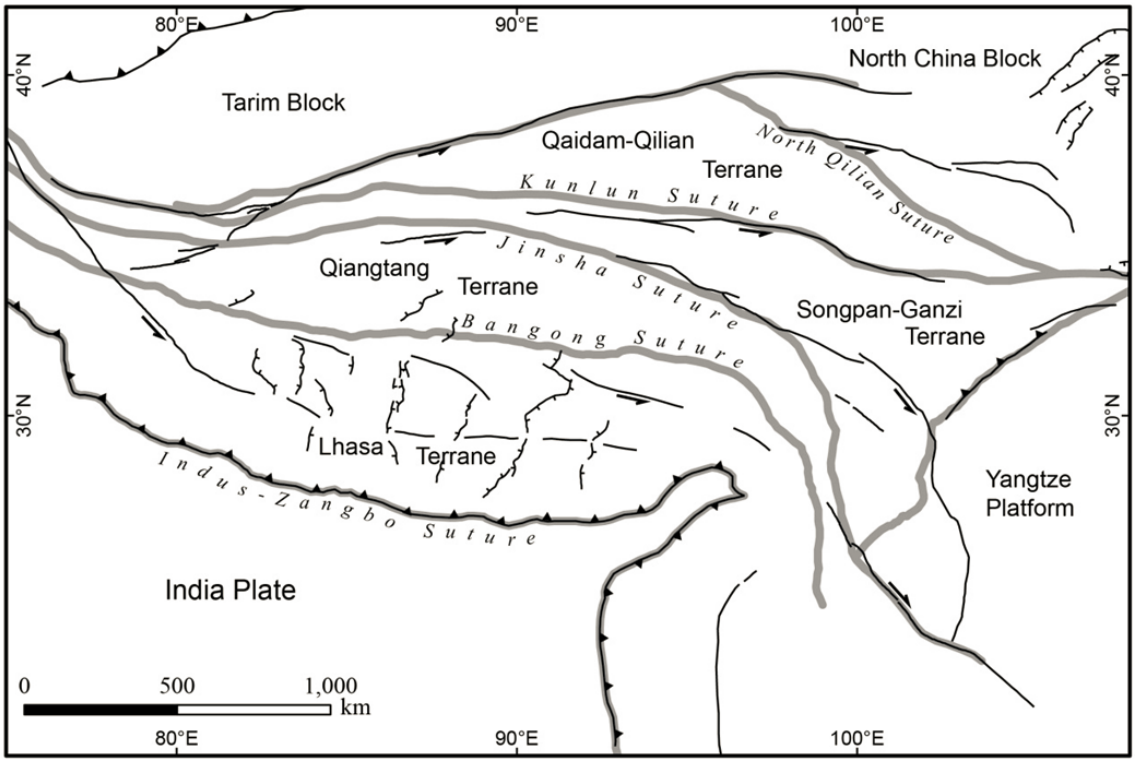

Fig. 3.2. Simplified sketch showing the major tectonic framework and terrane composition bounding by sutures (modified from Yin and Harrision, 2000).

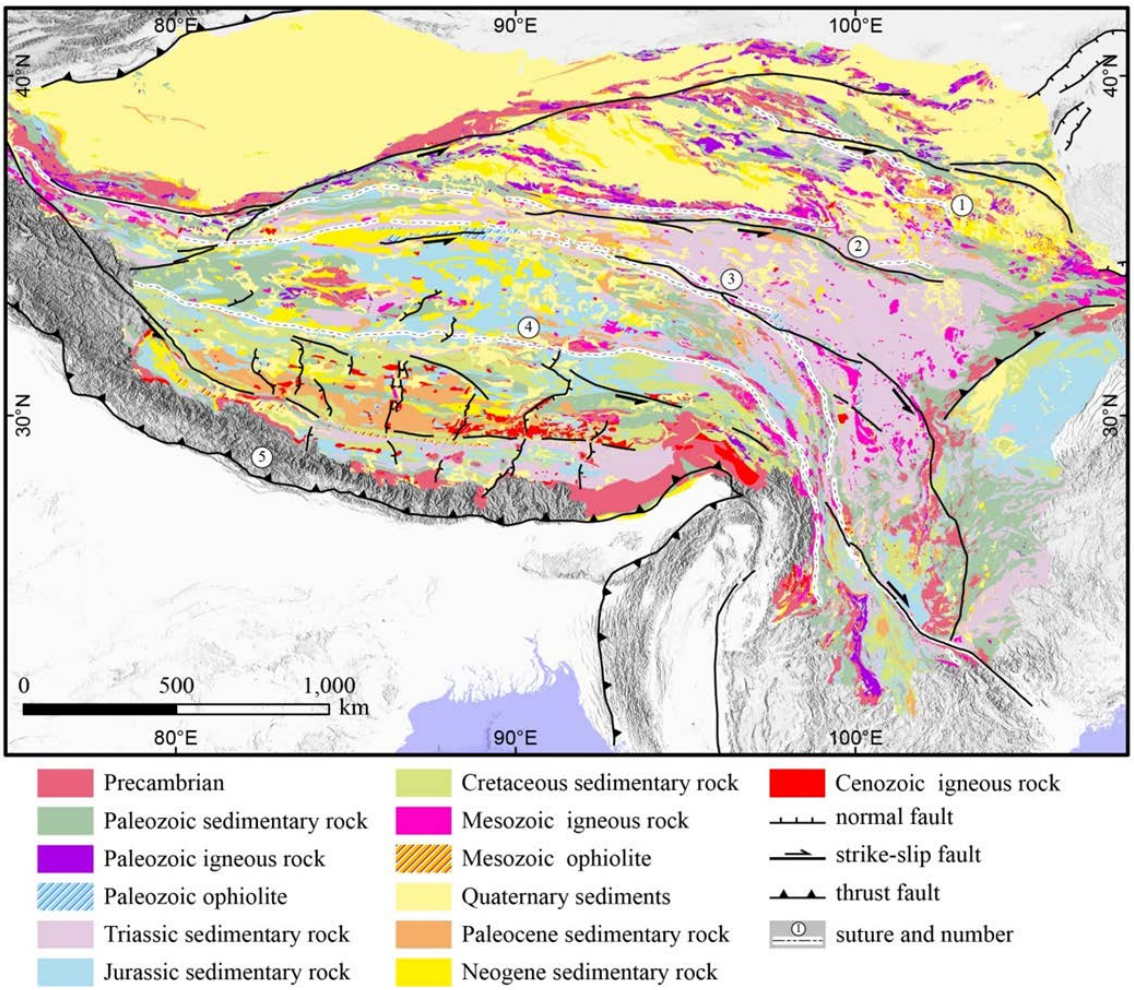

Fig. 3.3. Geologic map showing the main framework and stratigraphy composition of the Tibetan Plateau (modified from the Chengdu Institute of Geology and Mineral, CAGS, 1988). The numbers of sutures are (1) North Qilian Suture, (2) Kunlun Suture, (3) Jinsha Suture, (4) Bangong Suture, and that (5) Indo–Zangbo Suture, respectively.

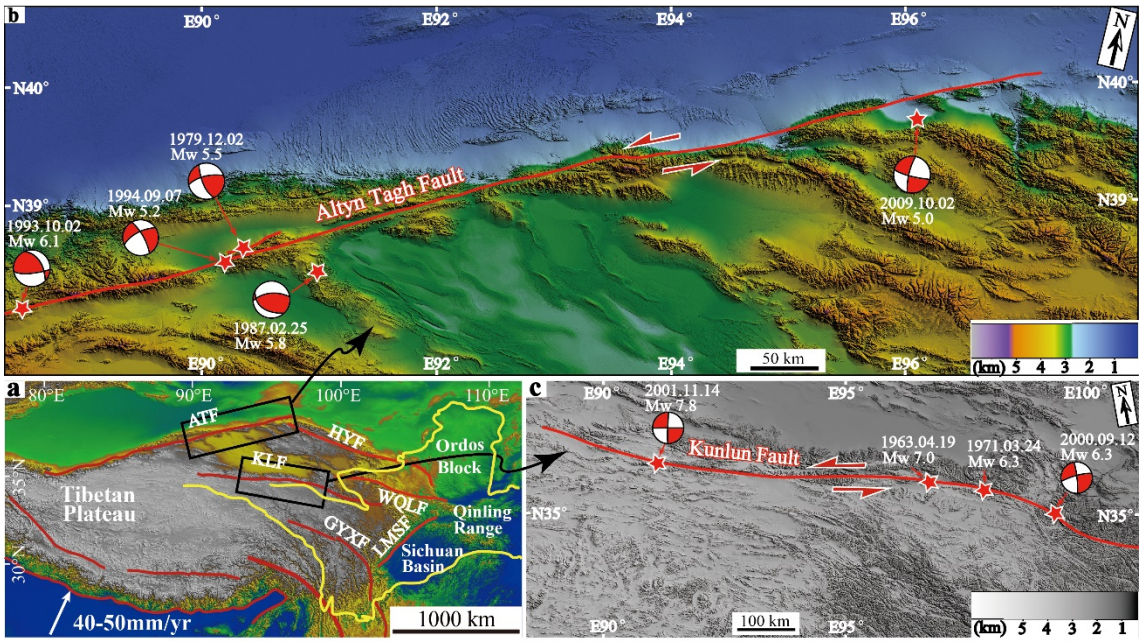

Fig. 3.4. Index map showing the tectonic background and topographic features of the study area. (a) Tectonic setting showing the location and major active faults within and surrounding the Tibetan Plateau. (b) Color-shaded relief map showing the topographic characters along the Altyn Tagh Fault. (c) Color-shaded relief map showing the topographic features along the Kunlun Fault. Epicenters and focal mechanism solutions are from the Global Harvard CMT catalogue (http://www.globalcmt.org). ATF: Altyn Tagh Fault; HYF: Haiyuan Fault; WQLF: West Qinling Fault; KLF: Kunlun Fault; GYXF: Ganzi–Yushu–Xianshuihe Fault.

Chapter 4. Tectonic geomorphology in the northeastern Tibetan Plateau

4.1. Abstract

The drainage system, as an important carrier of topographic features, can provide critical constraints to characterize the active tectonic processes and associated tectonic geomorphology. Based on the topographic analysis via the extraction of drainage systems, interpretation of remote sensing images and 3D processing of DEM data, together with field observations reveal that: i) the WNW-trending en echelon topographic divides developed in the northeastern marginal zone of the Tibetan Plateau separate the tributary drainage systems of the Yellow River; ii) the late Cenozoic strata and deposits distributed on both sides of these divides has been folded and tilted, and the latest fluvial deposits are also tilted, manifesting the tectonic tilting and uplifting is still active in this region near these divides; and iii) the regional axis of maximum compressive stress, as inferred from the geological structures and fold deformation developed in the late Cenozoic strata and deposits, trends NE–SW to ENE–WSW. The findings obtained in this study demonstrate that the formation of these topographic divides separating the Yellow River drainage systems in the northeastern Tibetan Plateau is possibly associated with flexural folding and uplifting under the northeastward compression, in response to the ongoing convergence between the Indian and Eurasian plates.

4.2. Introduction

The uplift of the Tibetan Plateau is regarded as a consequence of the subduction and collision between the Indian Plate and the Eurasian Plate since ~50 Ma ago, which has been widely accepted by most geologists, geophysicists and geomorphologists (e.g., Yin

and Harrision, 2000; Tapponnier et al., 2001), and in turn the uplift of the Tibetan Plateau caused enormous changes in topography, climate, drainage system evolution and the geodynamic process (e.g., Molnar et al., 1993; Yin and Harrison, 2000; Tapponnier et al., 2001). Among these geological and geomorphological indicators, the evolution of drainage systems, especially for the great rivers, as one of the most sensitive topographic factors, can best be shaped by tectonic process and thus record the important information of tectonism, although they are modified by climatic change and local lithological control (Brookfield, 1998; Yan and Lin, 2015). Therefore, the drainage systems are generally used as the geomorphic markers that record accumulated fault displacement due to the repeated slipping events (Ouchi, 2005). Meanwhile, drainage systems are deeply influenced by the topographic relief, and has an authentic feedback to the differential uplift of rocks along or across fault and fold (e.g., Jackson et al., 1996; Formento-Trigilio et al., 2002; Yan and Lin, 2015; Walker, 2006). Such examples have been reported all over the world. In the foothills of the Nepalese Himalaya, through examining the height difference river terraces and dating the deformed geomorphic markers, the shortening rate across the main frontal thrust fault of the southern Himalayan fold belt was estimated (Lavé and Avouac, 2000). In southeast Iran, which is actively deforming, the geometry and morphology of active flexural folds developed in the late Quaternary alluvial fan and terrace deposits was accurately constrained by analyzing the deflection and migration of stream channels (Walker, 2006; Ramsey et al., 2008). In the Catania region in eastern Sicily which is characterized by recent large earthquakes, a new kinematic and dynamic model was proposed through the comparison of channel morphology between the pre- and post-deformation. Morphological observations applied on the late Pleistocene–Holocene

alluvial terraces indicate that young sedimentary deposits is experiencing the active flexural folding and uplifting (Catalano et al., 2011). Similarly, in the Himalayan–Tibetan Plateau, the pattern and morphology of drainage system networks was controlled and shaped by the regional continental subduction, collision and active tectonic processes (e.g., Seeber and Gornitz, 1983; Gupta, 1997; Lin et al., 2001; Clark et al., 2004; Yan and Lin, 2015).

The northeastern marginal zone of the Tibetan Plateau, as the frontal belt of plateau outward growth and expansion, locates in a transition zone between the high-elevation thick crust (> 45 km) in the central Tibetan Plateau and the low-elevation thin crust (< 45 km) of adjacent cratons (Ye et al., 2015), providing a natural laboratory to determine the interaction between active tectonics and topographic response (e.g., Tapponnier et al., 1982; Burchfiel et al., 1991; Hubert-Ferrari et al., 2007). The Yellow River, the fifth longest rivers in the world with a total length of ~5500 km, originates from the central Tibetan Plateau and occupies a huge drainage area in the northeastern plateau. The Yellow River has a complex geometry and develops a square bending from northwestward to northeastward at the central segment of its course (Fig. 4.1b and c). Since the Pleistocene, a topographic divide formed by folding and uplifting has separated the Yellow River from its tributary drainage system of the Weihe River (Lin et al., 2001). Therefore, the study in the geometry and morphology of drainage systems may provide important constraints and direct evidence on active tectonism, which helps understand the interaction between tectonic process and drainage system evolution.

In this study, the drainage system networks developed in the northeastern Tibetan Plateau were extracted using the DEM data and GIS tools to analyze and confirm the existence of these topographic divides. In addition, in order to observe tectonic

deformation at both sides of these topographic divides, field investigations were conducted. Finally, the formation mechanism of the regional-scale topographic divides, and active tectonic implications for the geodynamics of the Tibetan Plateau were discussed.

4.3. Tectonic setting

The study area, located in the northeastern corner of the Tibetan Plateau, bridges the central Tibetan Plateau and the northeastern Ordos Block, and also has a function as the frontal belt of the northeastward expansion of the Tibetan Plateau (Fig. 4.1a). Due to the special tectonic background, the structural pattern, deformational characteristics and the topographic response of the northeastern Tibetan Plateau have been extensively examined by research projects with the purpose of characterizing the timing and deformation since the collision between the Indian and Eurasian plates (Yuan et al., 2013; Lease, 2014). A complex pre-Cenozoic tectonic evolution history comprising multiple phases of Proterozoic basement deformation, early Paleozoic orogeny, Jurassic–Cretaceous extension, and subsequent tectonic uplift since the collision have occurred in the northeastern Tibetan Plateau (Yin and Harrison, 2000). The Silurian flysch sedimentary sequences, Ordovician–Silurian intrusive bodies, and low- to high-grade metamorphic rocks constitute the main body of the basement rocks (Xi’an IGMR, 1992). The red strata composed of Jurassic–Cretaceous sandstone, siltstone, conglomerate, carbon-rich shale and coal are widely-distributed in this region, recording a transition from marginal marine and lacustrine environment to terrestrial sedimentation (Gansu BGMR, 1989).

In geomorphology, the most obvious characteristics of the northeastern Tibetan

Plateau is the alternately-distributed basin and range topography, contrasting with the relatively flat surface in the central Tibetan Plateau. A steep topographic boundary developed in the transition zone where the elevation drops off rapidly to lower than 1.5 km to the northeast in the Longzhong Basin across the WQLF (Fig. 4.1b). To the northeast, the Ordos Block has been suggested to be a relatively stable craton with an average elevation of ~1300 m, where far fewer earthquakes ever occurred according to the historical and instrumental records in comparison to the adjacent plateau (Earthquake Disaster Prevention Department of China Earthquake Administration [EDPDCEA], 1995; Liu et al., 2006).

In structural geology, the tectonic deformation in this region was suggested to be associated with crustal shortening and left-lateral strike-slip faulting due to the ongoing northeastward expansion of the Tibetan Plateau (Burchfiel et al., 1991; Meyer et al., 1998). Two regional-scale WNW-trending active faults, the Haiyuan Fault (HYF) and the West Qinling Fault (WQLF), are lying in this area. First, the HYF, the source seismogenic fault of the 1920 M 8.5 Haiyuan earthquake, trends WNW in the west and NE- to NNE-trending in the east. Burchfiel et al. (1991) suggested that the Haiyuan fault was not tectonically active during the early Oligocene to late Miocene. Then, it became active as a result of NE–SW shortening characterized by the fold deformation and thrust faults developed within the Pliocene strata. The initiation timing of the left-lateral strike-slip faulting was suggested to be in the late Pliocene (Burchfiel et al., 1991; Ren et al., 2016). To the west, the WNW-trending HYF has accommodated 10–15 km left-lateral displacement at an average slip rate of 5–10 mm/yr during the Quaternary period (Burchfiel et al., 1991; Zhang et al., 1988), which is consistent with the results of GPS measurement and geophysical data (Zhang et al., 2004; Gan et al.,

2005). To the east, the HYF changes its striking from NW- to NNW-trending, accompanying the transformation of slip sense from left-lateral strike-slip to reverse slip in the Liupanshan area (Fig. 4.1b). The 1920 M 8.5 Haiyuan earthquake occurred on the HYF, produced a ~237-km-long coseismic surface rupture with a maximum left-lateral strike-slip displacement of 10.5 m (Institute of Geology, SSB, 1990). In addition, a millennial recurrence interval of large earthquakes was reported based on the investigation results of 19 trenches on the Haiyuan Fault (Zhang et al., 1988b).

Second, the WQLF, striking nearly E–W in the west and WNW–ESE in the east, bounds the Longzhong Basin to the south and the West Qinling Range to the north with an elevation difference of ~500–1500 m (Fig. 4.1a). The evolution history of the WQLF was divided into two distinct phases by initiating as a frontal thrust fault since Paleogene due to the northeastward compression of the Tibetan Plateau, then transforming into a dominated left-lateral strike-slip fault since the late Quaternary (Li et al., 2007). As a mature active fault, large historic earthquakes repeatedly occurred on the WQLF, followed by the AD 143 M 7.0 Gangu West, AD 734 M ≥ 7.0 Tianshui, and the most recent 2013 M_s 6.6 Zhangxian earthquake.

The structural geology and historical seismicity strongly indicate that both the HYF and WQLF, as two regional-scale left-lateral strike-slip fault developed in the northeastern Tibetan Plateau, have a potential to cause large earthquakes. In this study, between the two active faults, the drainage system network of the Yellow River and its tributaries was extracted to analyze the topographic characteristics and tectonic deformation with a particular focus on these topographic divides.

4.4. Method

To determine the occurrence and formation mechanism of these topographic divides, the following methods were used in this study. First, the drainage systems developed in the northeastern marginal zone of the Tibetan Plateau were extracted using the DEM data and GIS tools, which confirm the locations of these topographic divides. Second, the 3D processing of DEM data and the interpretation of high-resolution remote sensing images are used to investigate the topographic features including push-up structures or tectonic bulges, especially for places where it is difficult to access due to high altitudes of the Tibetan Plateau. The interpretation of abnormal topography such as the push-up structures or bulges developed within the alluvial fan and terrace deposits help analyze the topographic characteristics of uplifted sediments (Figs. 4.4–4.5). Third, the structural analyses and field investigation were carried out to observe deformational features of the strata and deposits in the periphery of these topographic divides (Figs. 4.6–4.9).

4.5. Topographic divides of the tributary drainage systems of the Yellow River

The Yellow River drainage systems developed in the northeastern Tibetan Plateau can be divided into six tributaries from west to east: Qinghai Lake, Shazhuyuhe, Huangshui, Taohe, Weihe, and Jinghe rivers (Fig. 4.1b). The topographic divides among these drainage systems were discerned and identified via the river extraction and watershed analyses processed from 30 m-resolution ASTER GDEM (ASTER global digital elevation model) data. The extraction is primarily based on the simulation of surface flow routes by assigning one or more flow directions to each DEM pixel. In order to ensure the water in each pixel to flow to the basin outlet, the depression-filling pretreatment of DEM data has to be conducted and the elevation of depression region

should be raised to that of the pouring-out point (Bai et al., 2015). The topographic divides generally trend WNW–ESE in the west and center of the study area and NNW–SSE in the Liupanshan region (Fig. 4.1b). In the west, the Qinghai Lake drainage system is separated from the Shazhuyuhe and Huangshui drainage systems by the Qinghai-nanshan and Lajishan divides, respectively. In the center, the Yellow River is separated from the Huangshui River to the north and Taohe River to the south by the Lajishan and Maxianshan divides, respectively. In the east, the Huajialing divide separate the Yellow River from the Weihe drainage system. In the northeast, the Weihe and Jinghe drainage systems are separated by the Liupanshan divide where the HYF terminates. The Yellow River flows eastward in the west and center of the study area, and changes its direction to the northeast near the Maxianshan and Huajialing divides. Then the course of the Yellow River follows a large rectangular bend around the Ordos Block (Fig. 4.1a). The four regional-scale topographic divides separating the Yellow River drainage systems display a left-stepping en echelon geometric pattern and occur within a WNW–ESE-trending zone bounded by the HYF and WQLF to the north and to the south, respectively (Fig. 4.1b). The special spatial configuration of these topographic divides lay the basic topographic framework of the Yellow River catchment between the HYF and WQLF, which controls the present-day morphology and geometry of the drainage system networks developed in the northeastern marginal zone of the Tibetan Plateau.

4.6. Topographic analyses of DEM data and remote sensing images

In order to characterize the geomorphic features of the four en echelon topographic divides, the three-dimensional topographic images were processed by exaggerating the

vertical relief based on the 30-m resolution ASTER GDEM data (Fig. 4.2, see Fig. 4.1b for locations). The topographic profiles across the four divides P1–P4 are shown in Fig. 4.3 (see Fig. 4.1b for profile locations). The 3D topographic images and profiles further help confirm the presence and basic geomorphic characteristics of these topographic divides in the northeastern Tibetan Plateau.

In order to observe the local-scale topographic features near these divides, representative remote sensing images were analyzed as shown in Fig. 4.4. At the south side of Qinghai-nanshan divide in the west of the study area, the piedmont alluvial fan and terrace deposits are deformed and uplifted, forming structural bulges in topography (Fig.4.4b–d). The abnormal topographic features are suggested to be in association with active flexural folding, because no distinct active faults are observed from the DEM and remote sensing images where the push-up structures developed (Fig. 4.4). The gullies developed on the alluvial fan surface were systematically deflected to the east due to the blocking of the uplifted alluvial fan sediments (Fig. 4.4d). The topographic profiles across the structural bulges display the distinctly different geomorphic characteristics when compared with the normal alluvial fan and terrace (Fig. 4.4f). In Fig 4.4f, the profile I–I' starts with the normal alluvial fan slope with an dipping angle of ~5–10^{o}, then the slope suddenly become steep with an angle of ~40–50^{o} and opposite dipping direction until another limb of the bulge. The width of the topographic bulge is measured to be ~600 m within the alluvial fan deposits (Fig. 4.4f). Similarly, the phenomena also developed within the terrace deposits, which could be observed at the eastern segment of Qinghai-nashan topographic divide (Fig. 4.4e). The topographic profile across the bugle indicate a ~700-m-wide uplifted area (Fig. 4.4g).

The push-up structures or structural bulges generally appear like a narrow-rounded

ridge with a gentle slope on both limbs, which are linked as a hillocky range. The newly-formed bugle or mole track generally follows and duplicates the pre-existing push-up structure and gradually become larger in size. In the horizontal direction, these push-up structures or bulges often form a linked array via the unceasing connection of different individuals. These structures vary in size from several meters to hundreds of kilometers in length, these regional-scale topographic divides formed through the unceasing duplication and connection of these outcrop-scale push-up structures as those of coseismic mole track structures previously-reported (Rao et al., 2011).

4.7. Tectonic deformation near the topographic divides

In structural geology, the term of “flexural fold” is generally used to describe fold deformation in sedimentary rocks with good layering (e.g., Yeats et al., 1997). The deformation mechanism that produce the flexural folds includes flexural slip, flexural shear or orthogonal flexure (Mount and Suppe, 1987). The flexural slip means the slipping occurs along the bedding interfaces during folding. The flexural shear means that the slip increases away from the hinge line, being opposite on the two limbs. In contrast, the term “active flexural fold”, which is used in the field of active tectonics, keeps the original definition with that in traditional structural geology and refers to flexural flow folds developed in weakly consolidated and/or unconsolidated sedimentary deposits during the recent geological time (generally in late Pleistocene–Holocene). What the “active flexural folding” emphasize is that the folding occurs in the young sedimentary deposits in the time span of the field of active tectonics. In this chapter, the term “flexural fold” is used to contain all varieties of flexural folds, including flexural slip and flexural shear folds that developed within the weakly

consolidated and/or unconsolidated sediments, and folds generating waveform landform in different temporal and spatial scales.

Late Quaternary alluvial fan and terrace deposits that have involved the fold deformation are suggested through the push-up structures as revealed by the topographic images and profiles across the topographic bulges (Fig. 4.4), which are also supported by the structural analyses and field observations of tectonic deformation developed within the late Cenozoic strata and alluvial fan and terrace deposits (Figs. 4.5–4.9).

Typical field outcrops and deformed geomorphological features were observed and confirmed at the south side of Qinghai-nanshan divide at Loc. 1 (see Fig. 4.4a for location). Three-level fluvial terraces are developing at both sides of river as reveled by the topographic image and the corresponding interpreted map (Fig. 4.5b–c). The terrace deposits composed of the interbedded sand and gravel have been disturbed to be tilted with the dipping angle of up to 16^{o} (Fig. 4.5d). The bedding structure was confirmed by the interbedded sand-gravel deposits composed of the fluvial pebbles and fine-grained sand-silt. The outcrop indicate that the terrace deposits is experiencing the tectonic tilting and flexural folding, which probably leads to the uplift of the divide.

At the Lajishan topographic divide that separate the Huangshui River from the Yellow River, the geological structure was analyzed to understand the tectonic deformation in this area (Fig. 4.6). From the close-up topographic image of Lajishan divide (Fig. 4.6a, see Fig. 4.1b for location), the topographic attribute of the divide could be explicitly defined as revealed by the separated drainage systems. The fold deformation developed within the late Cenozoic strata could be discerned and identified according to the attitude data presented in the geological map (Fig. 4.6b). The result

indicate that the Eocene strata developed in Lajishan area have been folded into anticline and syncline structures, and the Pliocene strata also has been tectonic tilted (Fig. 4.6b), probably leading to the uplift of Lajishan area and the formation of the topographic divide. Here, it should be noted that the pre-Mesozoic basement rocks developed in this area possibly have been a high-altitude terrain before the flexural folding, but what is emphasized in this study is that the late Cenozoic tectonic deformation contributes the uplift and formation of topographic divide to some extent. The fold deformation developed within the late Cenozoic strata and deposits indicates the NE-trending compressive stress.

In Fig. 4.7a (see Fig. 4.1b for location), at the eastern segment of Maxianshan topographic divide, the Yellow River changes its course from northeastward to northwestward and then turns to northeastward again with a “z-shape” geometric pattern. Around the turning points, the channel width significantly decreases from the wide upstream to the narrow linear channel near the divide (Fig. 4.7a). It is inferred that the change was possibly caused by the compression and contraction of the Maxianshan divide. If the change was produced by the naturally lateral erosion, the channel width should keep roughly similar in such short distance. Therefore, it is the tectonism-derived uplift that leads to the change of water flowing and channel width of the Yellow River. The analyses are supported by the result of field observation. At the north side of Maxianshan topographic divide at Loc.2 (see Fig. 4.7a for location), the sand-gravel deposits show asymmetric flexural fold deformation with a curved bedding structure. The dipping angle gradually become larger from sub-horizontal at the core to up to ~30° at its eastern limb with the dipping direction to NE (Fig. 4.7b), indicating the NE-trending compressive stress.

In the east of the Huajialing topographic divide, the geomorphological analysis and geological investigation were conducted. Similar with the other three topographic divides, the close-up topographic image clearly shows the distribution of drainage systems at both sides of Huajialing divide that separate the Weihe River from the Yellow River. In the north, the branch of the Yellow River drainage system flows northward into the mainstream, while Weihe River flows southward in the south of Huajialing divide (Fig. 4.8a, see Fig 4.1b for location). The geological map near this divide indicates that the strata is mainly composed of the Pliocene sandstone, conglomerate and the Pleistocene unconsolidated and/or weakly consolidated sand-gravel. According to the attitude data, the Pliocene strata has been folded into the different anticline and syncline structures (Fig. 4.8b). The geological structures developed within the late Cenozoic strata and deposits show the continuous fold deformation, indicating NE-trending tectonic compression. At the summit of Huajialing topographic divide at Loc.3 between the Weihe River and Yellow River drainage systems (see Fig. 4.8b for location), the reddish brown strata composed of sand-gravel deposits are tilted with a dip angle of 40–60^{o} (Fig. 4.9a). Furthermore, the terrace deposits appears at the summit of this divide which is ~200 m higher than the riverbed (Fig. 4.9b), suggesting a great uplift since the deposition of the terrace deposits characterized by the fluvial pebbles with good roundness and sorting (Fig. 4.9c–d).Based on the interpretations of 3D topographical images and field observations in the vicinity of the four left-stepping en echelon topographic divides, the late Cenozoic strata and alluvial fan and terrace deposits at either side of the topographic divides have been flexural folded with the general NW- and WNW-trending axes (Fig. 4.1) that are sub-parallel to the HYF and WQLF. The deformed topographic features including terrace and alluvial fan are the

latest expression of active flexural folding during the late Pleistocene–Holocene in the northeastern marginal zone of the Tibetan Plateau.

4.8. Discussion

4.8.1. Formation timing and mechanism of the regional-scale topographic divides

The temporal and spatial relationship between the regional-scale geological structure and the local-scale deformation may be the most basic project in geology and geomorphology, which needs to be considered using an evolutionary view. The earlier fold deformation and mountain uplift before Quaternary has possibly occurred, indicating a long-term geologic and geomorphological process during the formation and growth of these regional-scale topographic divides. Furthermore, the late Pleistocene–Holocene deposits developed in the alluvial fan and terrace also occurred tectonic uplift and fold deformation as revealed by the topographic images and field observations. That is, the flexural folding is still existing since the Neogene or earlier, which probably corresponds to the interseismic strain accumulation. The fact that the newly-formed topography often inherits and duplicates the pre-existing topography has been widely accepted by most geologists and geomorphologists (Burbank and Anderson, 2012). In vertical direction, the flexural folds or topographic bulges become higher in altitude via the unceasing duplication and superimposition of outcrop-scale deformation structure. In horizontal direction, it is suggested that these topographic divides gradually become larger and longer over time through the unceasing connection and combination of the push-up structures or bulges. Eventually, the regional-scale topographic divides formed by the endless vertical uplift and lateral connection and made them what they look like today that separate the Yellow River drainage systems.

Here, we have to realize that the regional-scale topographic divides formed through a long geologic history, rather than during a short time-span of active tectonics alone. What is emphasized in this paper is that the tectonic tilting and uplifting are still active in this region based on the evidence of tilted fluvial deposits. These topographic divides are still growing and uplifting.

The maximum principal stress inferred from the fold deformation developed in the late Cenozoic strata and deposits as presented in Figs. 4.6 and 4.8 is oriented NE, which is consistent with that estimated from the focal mechanisms of modern earthquakes (Fig. 4.1b). The observations of GPS velocity vector also indicate the NE-trending compressive stress in the northeastern marginal zone of the Tibetan Plateau (Zhang et al., 2004). This compression is suggested to be in association with the northeastward expansion of the Tibetan Plateau accommodating the ongoing convergence between the Indian and Eurasian plates.

4.8.2. Tibetan–Himalayan drainage systems

The geometry and morphology of stream channel are excellent carriers and indicators to reflect regional tectonic processes, especially for areas which are experiencing active faulting and folding (e.g., Howard, 1967; Ouchi, 2005; Walker, 2006; Melosh and Keller, 2013). Studies of the Tibetan–Himalayan drainage systems and other large rivers worldwide indicate that the flow of rivers generally follow major structures and tectonic lineaments, and therefore record the information of tectonism acting on the drainage systems (e.g., Jackson, et al., 1996; Schumm et al., 2000; Lin et al., 2001; Clark et al., 2004).

Major rivers on the Tibetan Plateau have been interacting with tectonic processes

including continental collision, regional tilting and tectonic extrusion (e.g., Lin et al., 2001; Lin and Guo, 2008; Kirby et al., 2002; Clark et al., 2004; Yan and Lin, 2015). The Yellow River, flows around a large rectangular bend, and is deflected by major active strike-slip faults developed in the northeastern Tibetan Plateau including the Kunlun Fault, Haiyuan Fault and WQLF (e.g., Burchfiel et al., 1991; Gaudemer et al., 1995; Zhang et al., 1998). The Maxianshan and Huajialing divides as presented here changed the course of the Yellow River from southeastward to northeastward, separating the mainstream of the Yellow River from the Taohe and Weihe drainage systems (Figs. 4.1 and 4.2).

In the southeastern margin of the Tibetan Plateau, the major rivers including the Yangtze River and its tributaries were suggested to be antecedent rivers based on an analysis of river longitudinal profiles (Seeber and Gornitz, 1983). That is, this area experienced a roughly uniform tectonic process since the collision between the Indian and Eurasian plates (Yin and Harrison, 2000). The Yangtze River, the world's third longest river with a total length of ~6300 km, also develops a large rectangular bend in the southwest of the Sichuan Basin, and changes its course from southward to eastward, and is separated from the Red River to the south by a topographic divide (Fig. 4.1a). Therefore, the great bending of the Yellow River and Yangtze River in their courses was suggest a control by tectonic uplifting and flexural folding in response to the ongoing collision and convergence between the Indian and Eurasian plates (Lin et al., 2001, 2008). The abnormal changes in geometry and morphology of the two largest rivers developed in the northeastern and southeastern margin of the Tibetan Plateau provide important information to constrain intracontinental processes of the Tibetan Plateau, and advancing the understanding of how the drainage system evolution responds to the

tectonic process.

4.9. Conclusions

In this study, based on the topographic analysis including the extraction of drainage systems, interpretation of remote sensing images and the 3D processing of DEM data, together with field observations, the following conclusions are obtained:

1) The WNW–ESE-trending left-stepping en echelon topographic divides separate the drainage systems that flow into the Yellow River.
2) The late Cenozoic strata and deposits distributed on both sides of these topographic divides have been folded and tilted, resulting in the uplift of the topographic divides.
3) The maximum compressive stress inferred from the directions of the flexural folds and geological structures indicate the NE-trending tectonic compression in the northeastern marginal zone of the Tibetan Plateau, probably associated with the ongoing convergence between the Indian and Eurasian plates.

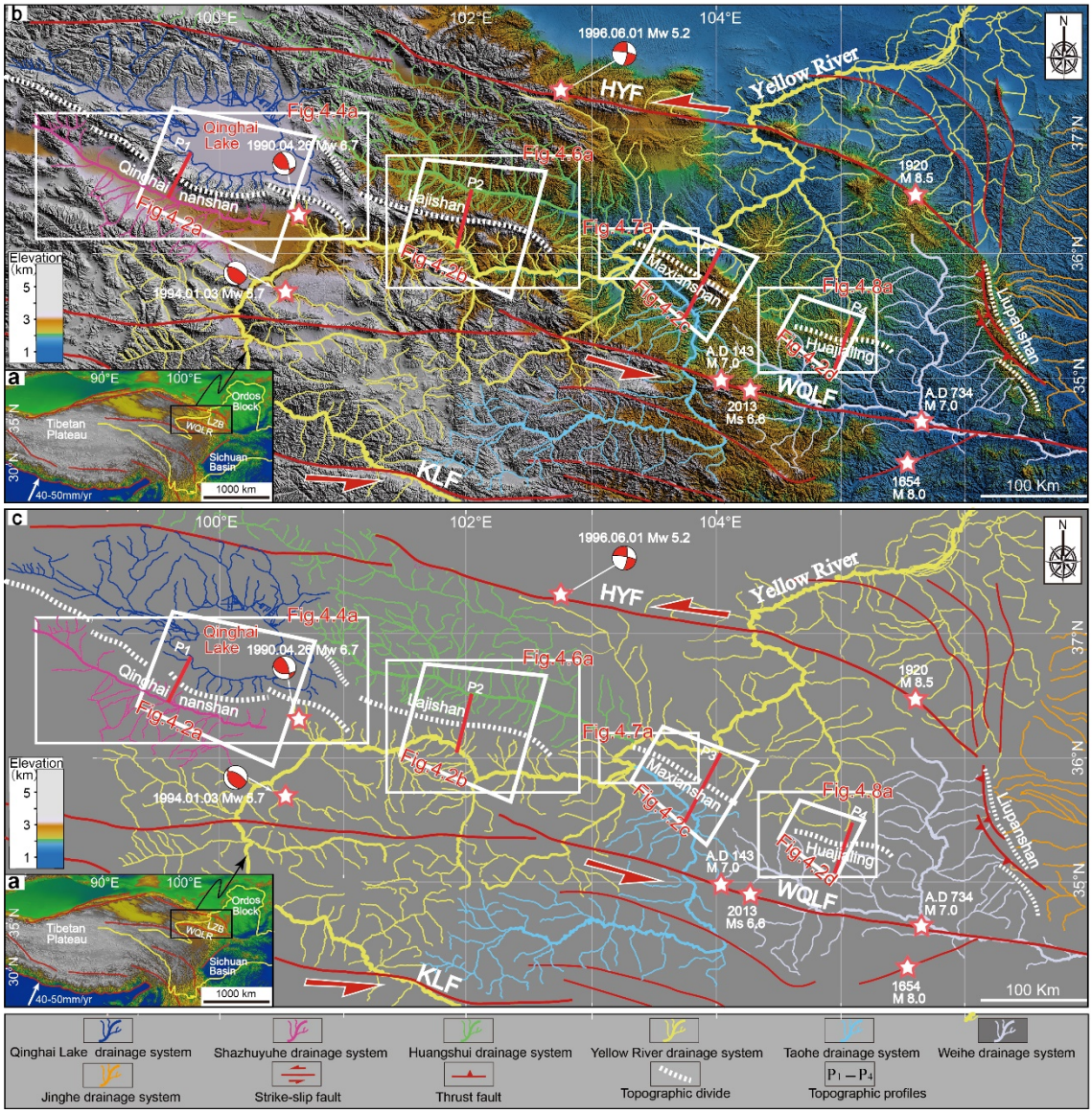

Fig. 4.1. Tectonic background and topographic features of the study area. (a) Tectonic setting of the study area showing the location and the major active faults within and surrounding the Tibetan Plateau. Block motion velocity of the Indian plate is cited from Zhang et al. (2004). (b) Color-shaded relief map showing the distribution of drainage systems that flow into the Yellow River, topographic divides, and major active faults on the northeastern marginal zone of the Tibetan Plateau. The drainage system was extracted from the 30-m-resolution ASTER GDEM data by using the GIS tools. Noting

the left-stepping en echelon geometry of the topographic divides. Historic earthquake information from the Earthquake Disaster Prevention Department of China Earthquake Administration catalogue (EDPDCEA, 1995). Epicenters and focal mechanism solutions are from the Global Harvard CMT catalogue (http://www.globalcmt.org). (c) Greyscale map of drainage systems without elevation information. HYF: Haiyuan Fault; WQLF: West Qinling Fault; KLF: Kunlun Fault.

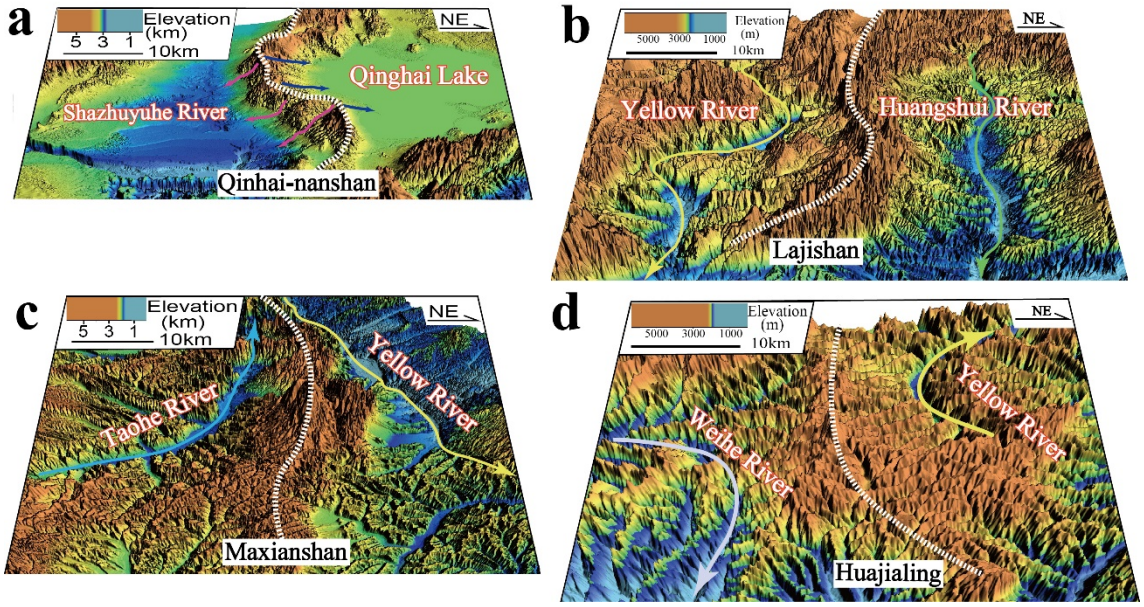

Fig. 4.2. Color-shaded relief maps showing the 3D perspective of the topographic divides that separate the Yellow River drainage systems (see Fig. 4.1b for locations). The arrows with different colors show the flowing direction of rivers. The color legends representing different rivers are consistent with that shown in Fig. 4.1. The white dashed line indicates the general striking of the topographic divides.

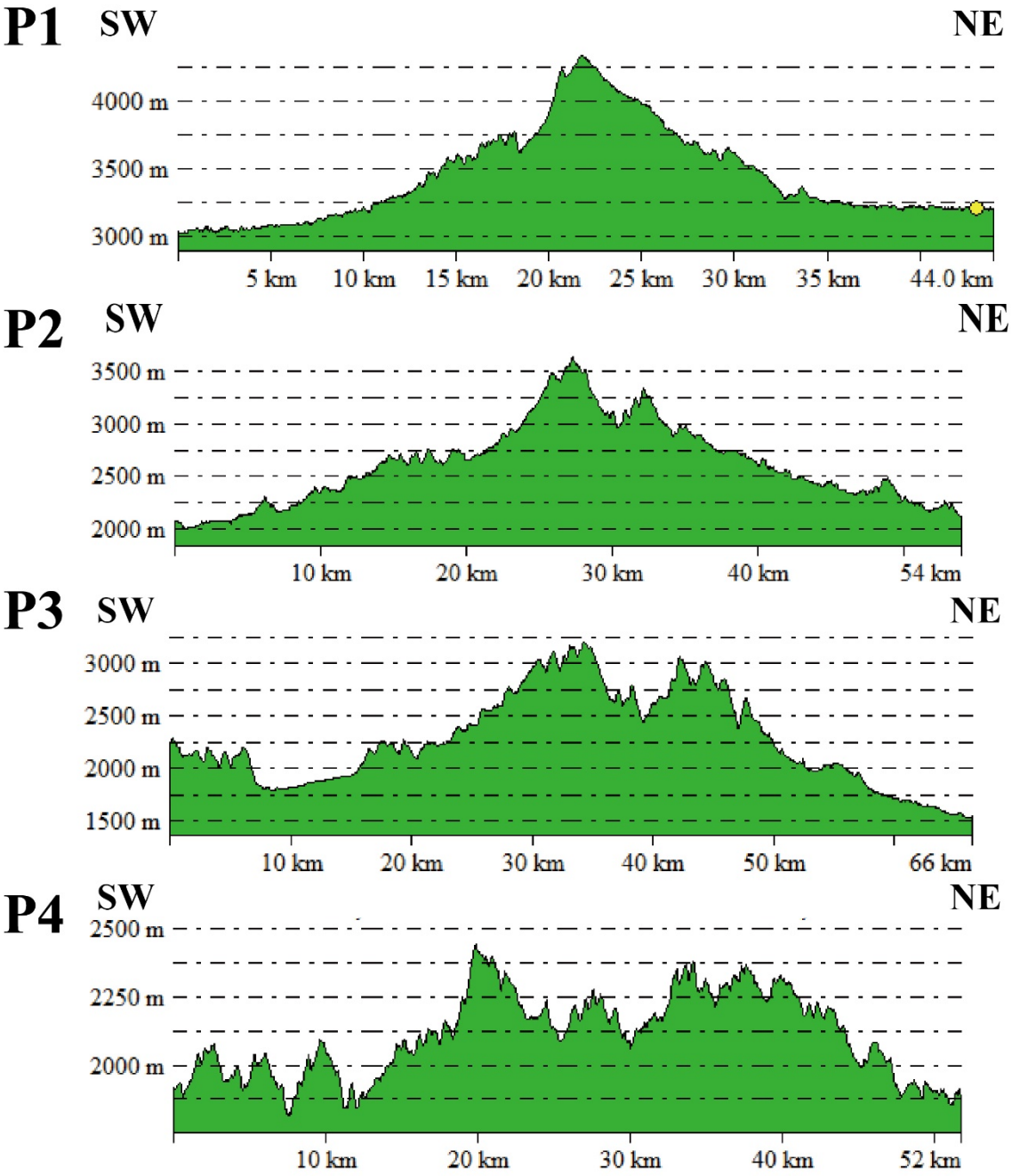

Fig. 4.3. Topographic profiles P1–P4 across the four topographic divides (see Fig. 4.1b for locations). (P1) Qinghai-nanshan topographic divide. (P2) Lajishan divide. (P3) Maxianshan divide (P4) Huajialing divide.

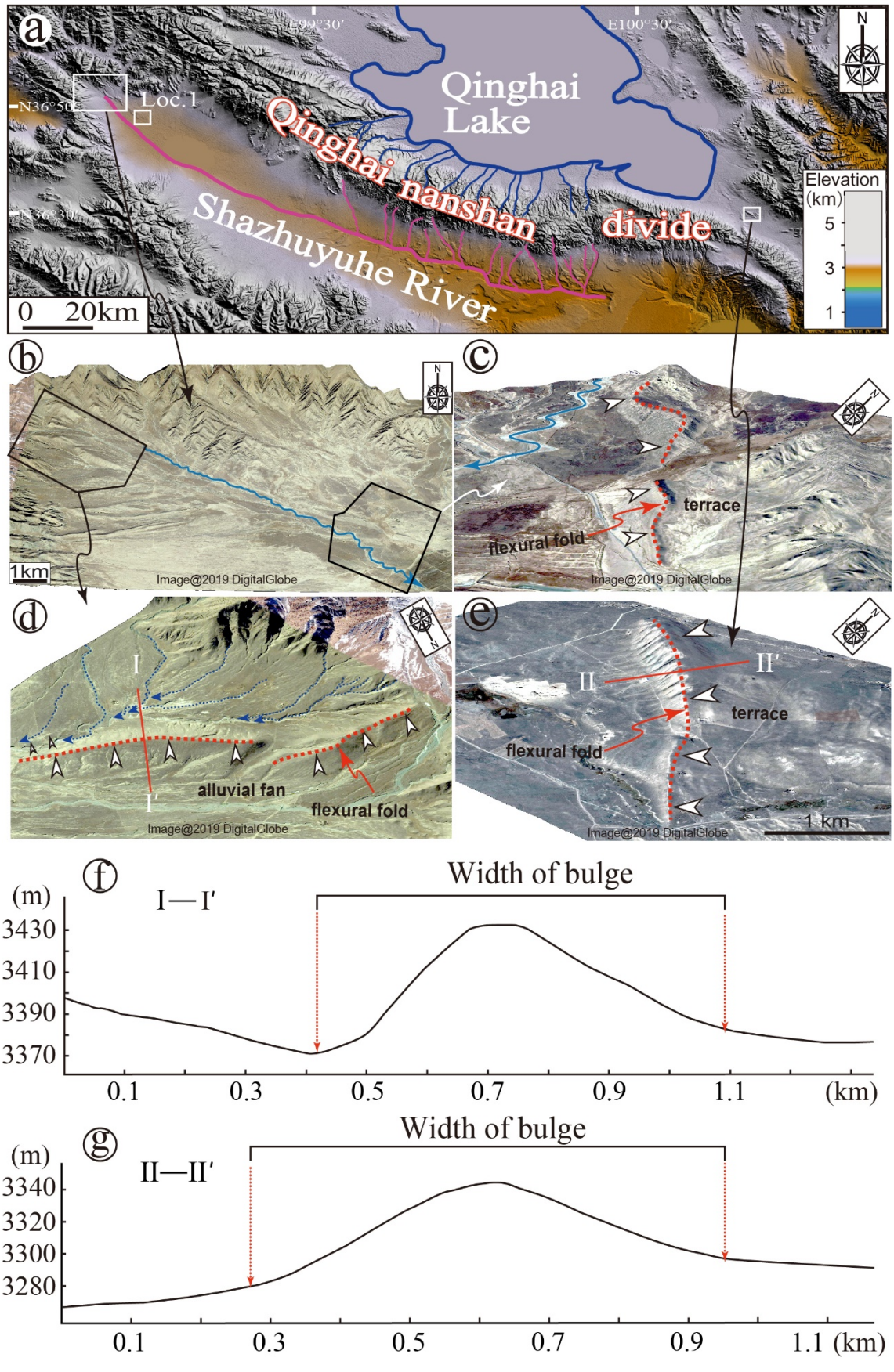
a
E99°30′
E100°30′
N36°30′
N36°30′
Loc.1
Qinghai Lake
Qinghai nanshan divide
Shazhuyuhe River
Elevation (km)
5
3
1
0 20km
b
1km
Image@2019 DigitalGlobe
c
terrace
flexural fold
Image@2019 DigitalGlobe
d
I
I′
alluvial fan
flexural fold
Image@2019 DigitalGlobe
e
II
II′
terrace
flexural fold
Image@2019 DigitalGlobe
1 km
f
I—I′
Width of bulge
(m)
3430
3410
3390
3370
0.1
0.3
0.5
0.7
0.9
1.1
(km)
g
II—II′
Width of bulge
(m)
3340
3320
3300
3280
0.1
0.3
0.5
0.7
0.9
1.1 (km)

Fig. 4.4. Color-shaded relief map and Google Earth images showing the geomorphological features of push-up structure or tectonic bulge developed withinalluvial fans and fluvial terraces (see Fig. 4.1b for location). (a) Color-shaded relief map showing the topographic features of the Qinghai-nanshan topographic divide. (b) Overview of the geomorphological setting showing the location of alluvial fan and fluvial terrace. (c) Push-up structure or bulge developed within terrace deposits with curved axes. (d) Tectonic bulge developed within alluvial fan deposits that have been folded and uplifted, resulting in the systematic deflection of gullies to the left. (e) Terrace deposits that has been folded and uplifted. The red dashed line indicates the general striking of the axis of the flexural fold. (f-g) Topographic profiles across the push-up structure and tectonic bulge in (d) and (e).

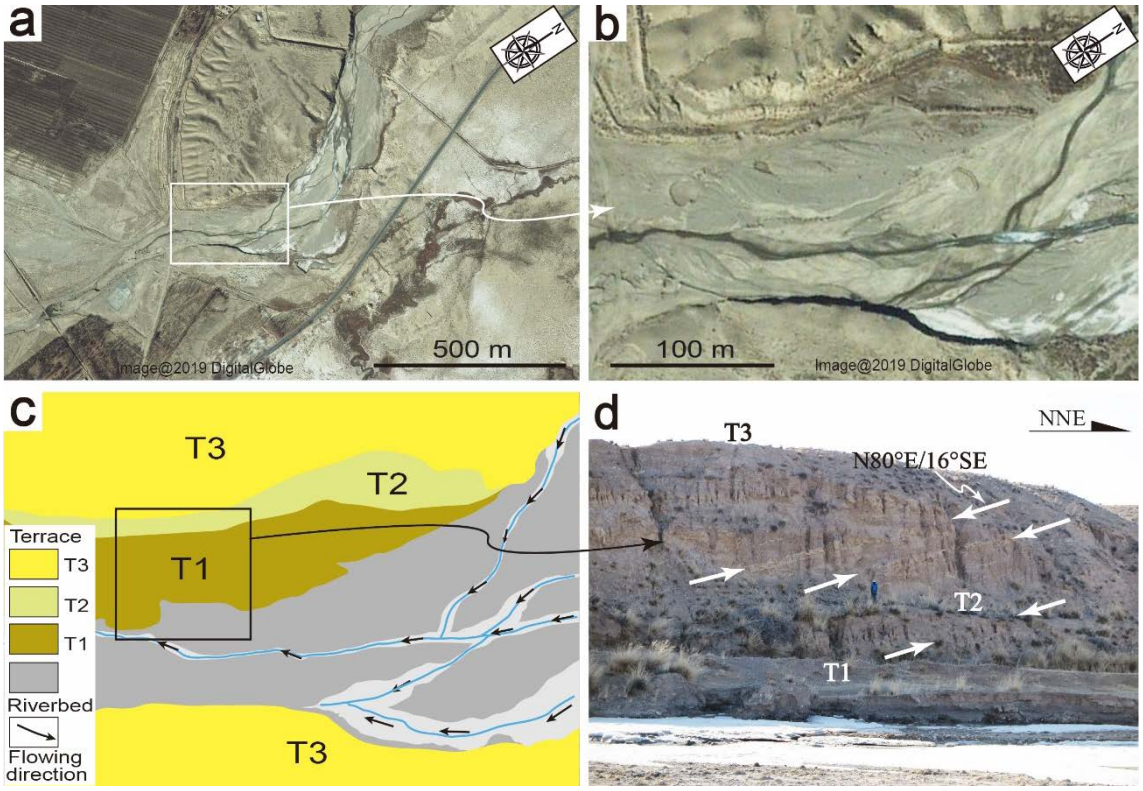

Fig. 4.5. Google Earth images and a field photograph showing the topographic characteristics and tectonic deformation of terrace deposits at the south side of

Qinghai-nanshan divide at Loc.1 (see Fig. 4.4a for location). (a–b) Google Earth images showing the topographic features of fluvial terrace. (c) Interpreted geomorphic map of (b) to show the terrace divisions. (d) Field outcrop showing a titled bedding structure of the terrace deposits. The white arrows indicate the bedding of the terrace deposits.

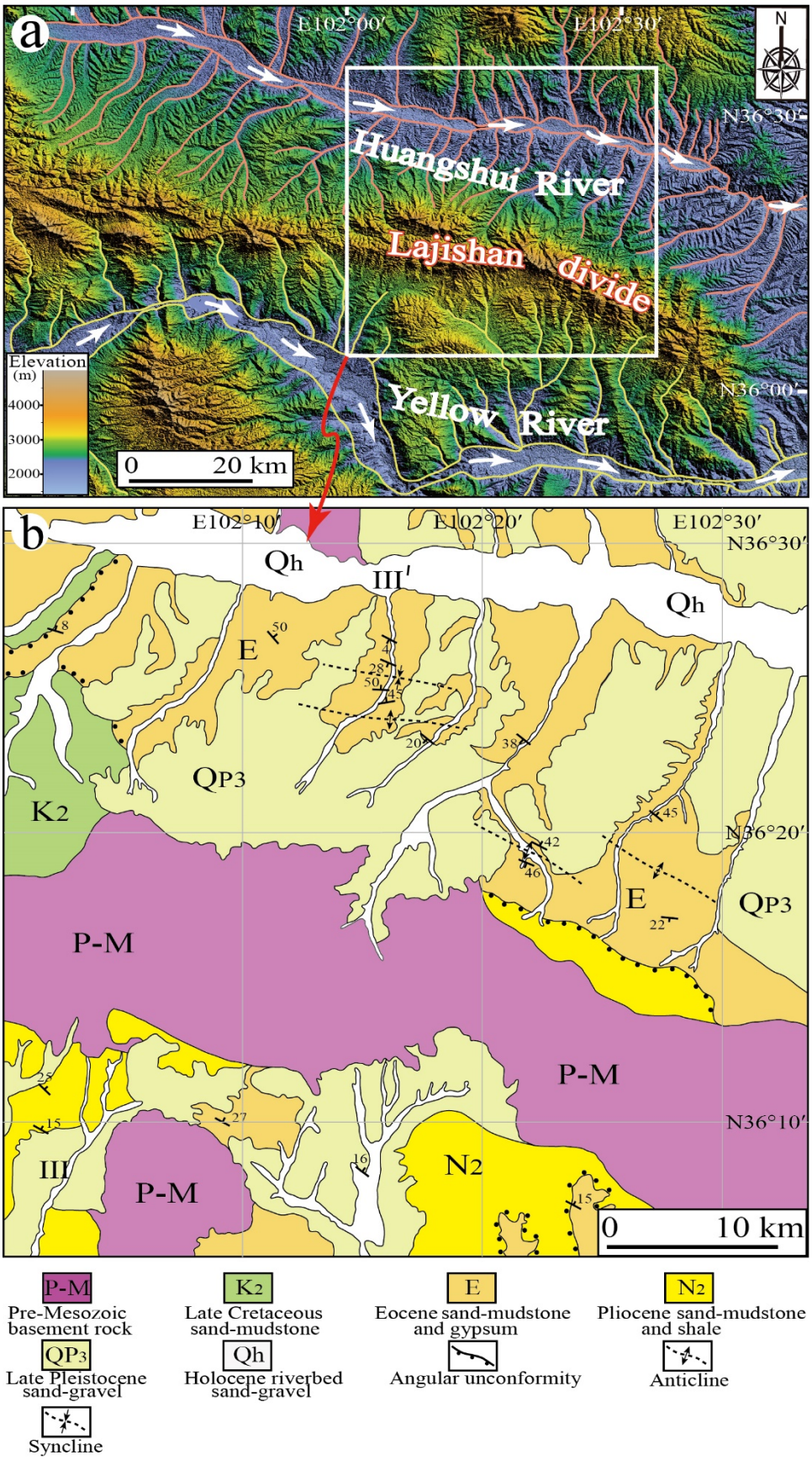
a
E102°00′
E102°30′
N
N36°30′
Huangshui River
Lajishan divide
Yellow River
N36°00′
Elevation (m)
4000
3000
2000
0 20 km
b
E102°10′
E102°20′
E102°30′
N36°30′
Qh
III′
E
QP3
K2
P-M
N36°20′
N2
III
N36°10′
0 10 km
P-M Pre-Mesozoic basement rock
K2 Late Cretaceous sand-mudstone
E Eocene sand-mudstone and gypsum
N2 Pliocene sand-mudstone and shale
QP3 Late Pleistocene sand-gravel
Qh Holocene riverbed sand-gravel
Angular unconformity
Anticline
Syncline

Fig. 4.6. Color-shaded relief map and geological map showing the topographic features and the geological structures at the Lajishan topographic divide. (a) Geomorphic image showing the topographic characteristics of the Lajishan topographic divide that separate the Huangshui River from the Yellow River (see Fig. 4.1b for location). (b) Geological map in the periphery of Lajishan topographic divide (Modified from the Qinghai BGMR, 2009). Note the anticline and syncline structures (broken line) developed in the late Cenozoic strata and deposits.

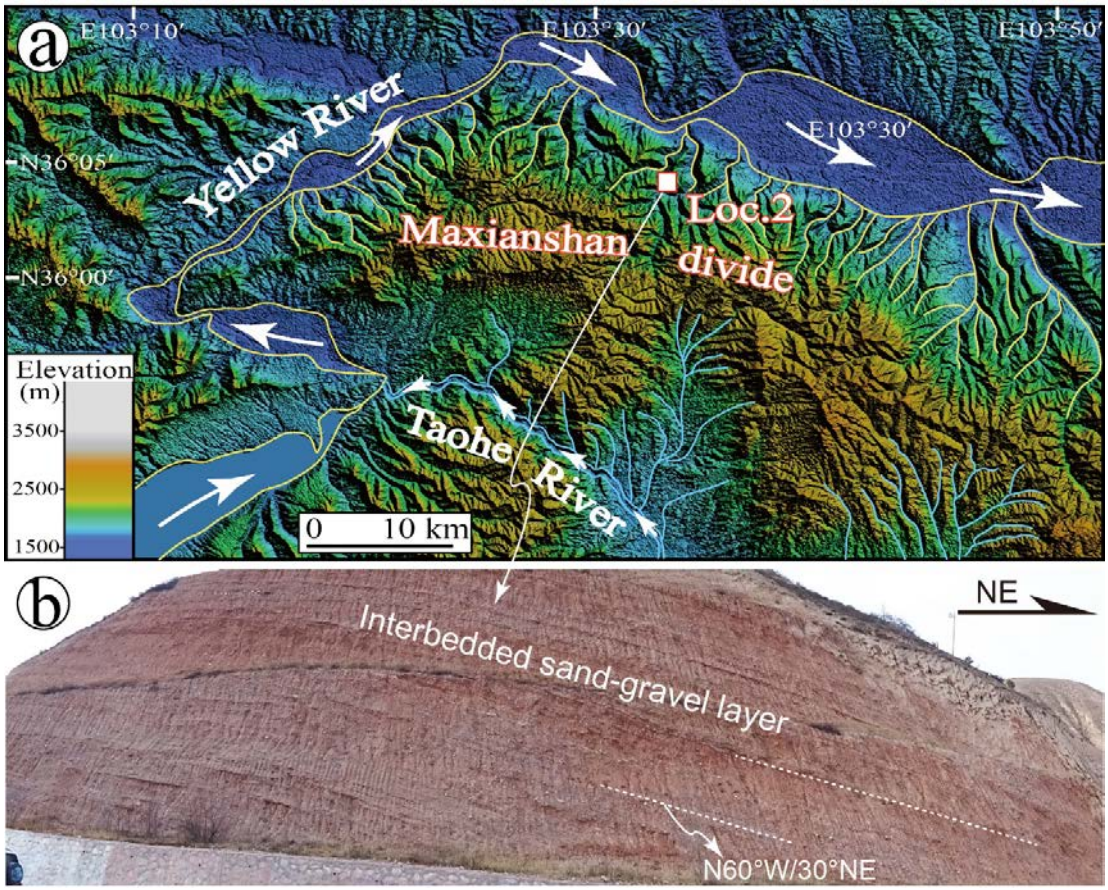

Fig. 4.7. Color-shaded relief map and field photograph showing the topographic features around the Maxianshan topographic divide and tectonic deformation developed within the conglomerate at Loc. 2 on the northern side of the divide. (a) The Maxianshan topographic divide that separates the Yellow River from the Taohe River as

shown by the drainage system distribution (see Fig. 4.1b for location). Note the change of channel width at the turning points of the Yellow River near this divide. (b) Arc-shape curved bedding structure developed within the brownish red conglomerate. Note the dipping direction of the strata is oriented NE-trending.

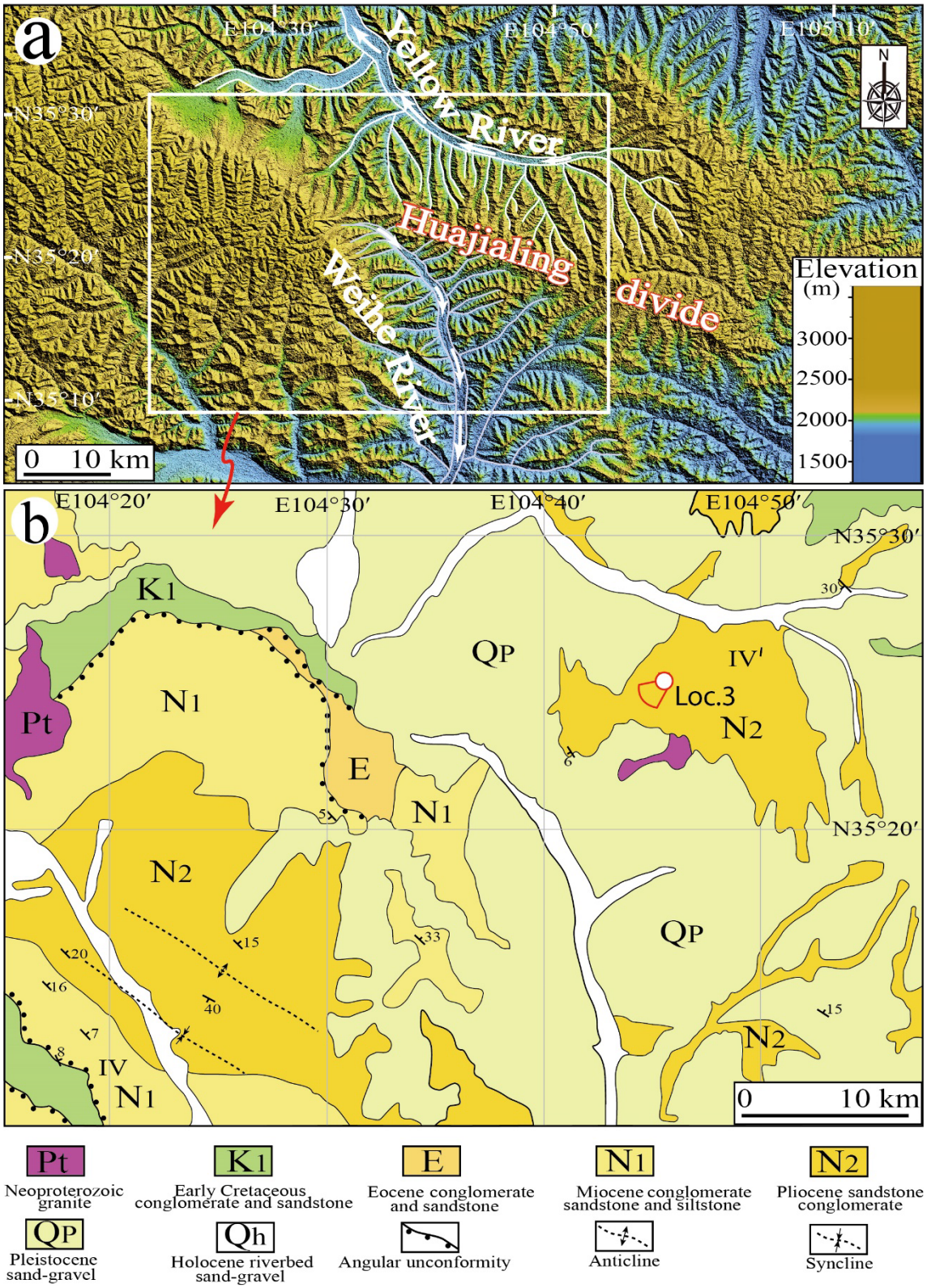

Fig. 4.8. Color-shaded relief map and geological map showing the topographic features and strata composition at the Huajialing topographic divide that separate the

Weihe River from the Yellow River. (a) Color-shaded relief map showing the topographic characteristics and drainage system distribution (see Fig. 4.1b for location). (b) Geological map in the periphery of the Huajialing divide (Modified from Gansu BGMR, 2006).

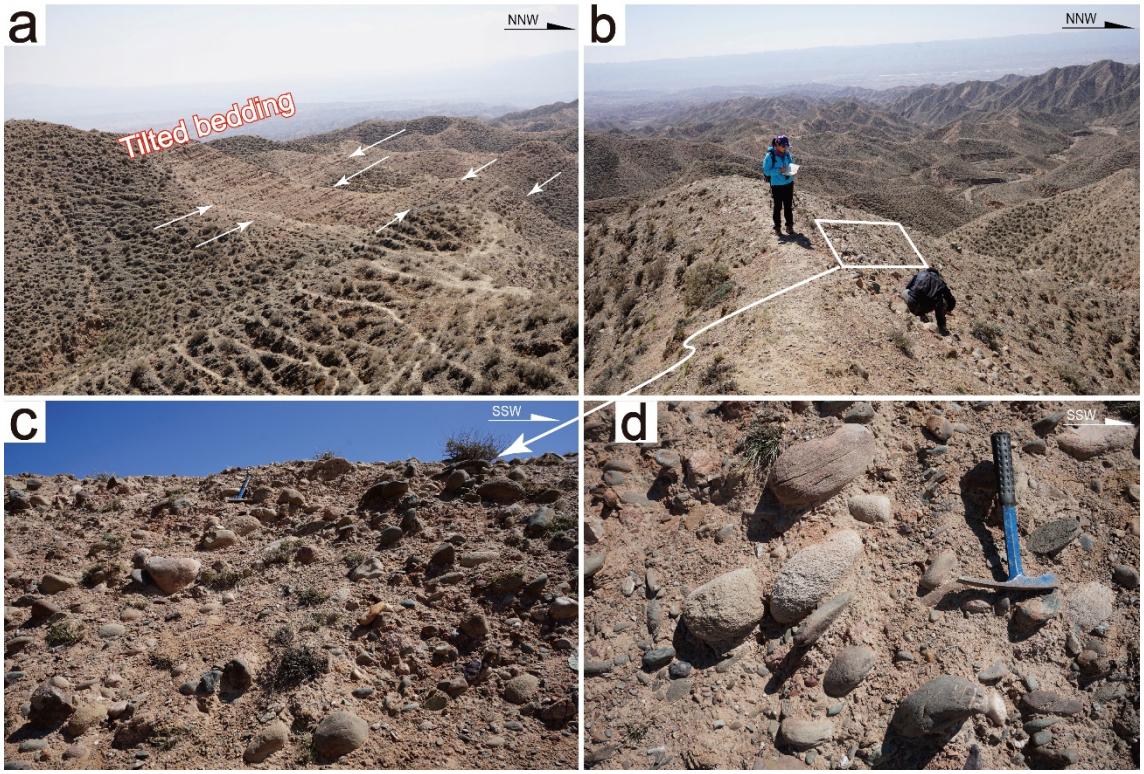

Fig. 4.9. Field photographs showing the strata attitude and deposits composition at Loc.3 in the Huajialing topographic divide (see Fig. 4.8b for location). (a) The tilted bedding structure developed within the terrace deposits as indicated by the white arrows. (b) Terrace deposits at the summit of Mountain, which is ~200 m higher than the riverbed, indicating a great uplift at the Huajialing area. (c) Fluvial pebbles with good roundness. (d) close-up view of fluvial pebbles.

Chapter 5. Late Pleistocene activity of the West Qinling Fault.

5.1. Abstract

A precise constraint of slip rate of active faults within and around the Tibetan Plateau will provide definite and explicit knowledge of the kinematics and dynamics of intracontinental processes. The WNW-trending West Qinling Fault (WQLF), the target of this study, is one of the major active strike-slip faults developed in the northeastern Tibetan Plateau. The interpretation and processing of three dimension (3D) topographic images and DEM data, together the field investigations and ^{14}C dating results reveal that i) the drainage systems, mountain ridges, alluvial fans and terraces have been systematically left-lateral deflected or offset by ~7 m up to hundreds of meters during the late Pleistocene–Holocene on WQLF in the northeastern Tibetan Plateau; ii) the late Pleistocene left-lateral strike-slip rate of the WQLF is estimated to be 2.0–2.6 mm/yr since the late Pleistocene; iii) compared to the well-studied active strike-slip faults developed in the northern and northeastern Tibetan Plateau such as the Altyn Tagh Fault and Kunlun Fault with high slip rate of > 10–20 mm/yr, the WQLF displays a characteristically low strike-slip rate of < 3 mm/yr. The low slip rate of the WQLF suggests that the strain was absorbed, partitioned and diffused by continuous crustal deformation in the northeastern Tibetan Plateau, rather than the localized deformation along strike-slip faults.

5.2. Introduction

Large-scale intracontinental strike-slip faults within and around the Tibetan Plateau play a critical role in absorbing and accommodating the tectonic deformation since the collision between the Indian and Eurasian plates (Yin and Harrison, 2000; Tapponnier et

al., 2001). In the northeastern marginal zone of the Tibetan Plateau, several strike-slip faults with length of larger than 500 km run through the margins and within the plateau interior, followed by the Kunlun Fault (e.g., Lin et al., 2002; Kirby and Harkins, 2013), WQLF (Li et al., 2007), and Haiyuan Fault (e.g., Zhang et al., 1988a, b; Ren et al., 2016) from south to north. The three left-lateral strike-slip faults display a subparallel geometry with the roughly consistent strike of WNW. Because modern large earthquakes frequently occurred on Kunlun Fault and Haiyuan Fault (e.g., the 2001 M_s 8.1 Central Kunlun earthquake and the 1920 M 8.5 Haiyuan earthquake), these two active faults have been the ongoing research focuses in the past two decades (Kirby et al., 2007; Ren et al., 2016). The basic parameters comprising the slip rate and recurrence interval of large earthquakes for these two strike-slip faults have been constrained well (Zhang et al., 1988a, b; Kirby et al., 2007).

Compared with the Kunlun and Haiyuan faults, the WQLF has been inadequately studied with few publications (Teng et al., 1994; Li et al., 2007), which severely hinders the comparison in slip rate among these strike-slip faults. The Kunlun Fault, as the source seismogenic fault of the 2001 M_s 8.1 central Kunlun earthquake, trends E–W to WNW–ESE with a total length of over 1200 km and exhibits an eastward diminished slip rate varying from 10–20 mm/yr at the western segment to ~3 mm/yr at its eastern tip (Shen et al., 2001., Kirby et al., 2007; Lin and Guo, 2008) The non-uniform along-strike slip rate indicates a diminishment toward the east at an average gradient of 1 mm/100 km (Lin and Guo, 2008), suggesting the eastward extrusion of central plateau probably terminated at the eastern tip of the Kunlun Fault. In addition, the Holocene strike-slip rate on the Haiyuan Fault was suggested to be 8 ± 2 mm/yr based on the analyses of deflected fluvial terrace (Zhang et al., 1988a), and the most recent

publication suggested a 4.5 mm/yr slip rate since the late Quaternary on the Haiyuan Fault (Li et al., 2009).

However, the overall deformational characteristics including the slip rate and the recurrence interval of large earthquakes for the 600-km-long WQLF are still unclear, although a previous study reported local deformation of a short fault segment (Li et al., 2007).

In order to advance the understanding of late Pleistocene activity on WQLF, the interpretation and processing of remote sensing images and DEM data, field investigations, and radiocarbon dating were conducted in this study. The role and active tectonic implications of the WQLF are discussed for the northeastern Tibetan Plateau.

5.3. Tectonic setting

In topography, the study area, located in the northeastern marginal zone of the Tibetan Plateau, occupies the transition belt from the high-elevation Tibetan Plateau to the low-elevation Ordos Block (Fig. 5.1a). The Yellow River, flows across the study area from the central Tibetan Plateau to Ordos Block (Fig. 5.1a). The Daxiahe River (DXHR) and Taohe River (THR), the tributaries of Yellow River, are cut and offset by WQLF with a distinct square bend (Fig. 5.1b). The densely-distributed drainage systems developed in this area make it possible to study the interaction between fault-displaced topographic features and active faulting.

The 600-km-long WQLF, striking E–W in the west and WNW–ESE in the east, developed along the topographic contact zone between Longzhong basin with an average elevation of ~1500–2500 m and West Qinling Range with elevations over 3000 m (Fig. 5.1). The West Qinling Range mainly consists of late Paleozoic or Triassic

marine-face sedimentary rocks, and the northern Longzhong Basin is composed of several secondary basins with a widely-distributed angle unconformity between Lower Cretaceous and Paleogene covered by Quaternary losses with varying thickness (Gansu BGMR, 1990)

Previous studies reveal that WQLF experienced a complex evolution history since its initiation as a frontal thrust fault in Paleogene (Clark et al., 2010). Due to the northeastward expansion of the Tibetan Plateau, the WQLF evolved into a dominated left-lateral strike-slip fault since late Quaternary (Li et al., 2007). As a mature seismogenic fault, large historic earthquakes repeatedly occurred on WQLF, including the AD 143 M 7.0 Gangu West earthquake, AD 734 M $\geq$ 7.0 Tianshui earthquake, (Earthquake Disaster Prevention Department of China Earthquake Administration [EDPDCEA], 1995), and the most recent (2013) Ms 6.6 Minxian–Zhangxian earthquake (China Earthquake Network Center [CENC], 2013), indicating the strong seismicity and potential seismic risk of the WQLF in the northeastern Tibetan Plateau. Therefore, the study characterizing the late Pleistocene activity of the WQLF is essential for exploring the theoretical significance of plateau expansion and assessing the potential seismic hazard in this area.

5.4. Tectonic geomorphology

The topographic features, as a carrier of tectonic geomorphology with well-preserved records to fault activity, are highly effective for assessing the deformation process and fault displacements due to repeated slipping events. Hence, topographic features are regarded as “paleoseismic fossil” (e.g., Koons, 1995; Lin and Guo, 2008). High-resolution Google Earth images and 30-m-resolution Shuttle Radar Topography Mission (SRTM) data released by NASA were used for processing three-dimensional

(3D) topographic maps in the process of topographic analysis. Using these topographic images, linear and surface topographic markers comprising stream channels, mountain ridges and alluvial terraces and fans could be recognized and identified on WQLF (Figs. 5.2, 5.3–5.4, 5.8–5.9).

As one of the most reliable geomorphic features, systematic deflection and/or offset of drainage systems along active strike-slip faults have been recognized and applied to characterize the deformational behavior and displacement accumulation (e.g., Matsuda, 1975; Huang, 1993; Ouchi, 2005; Yan and Lin, 2015). The Yellow River, developed in the northeastern marginal zone of the Tibetan plateau with several tributaries running through the study area. The Taohe River and Daxiahe River, the main tributaries of the Yellow River, change their flowing direction from northeastward to northwestward with a distinct square bend when passing through the WQLF (Figs. 5.1b and 5.2a).

In order to clarify the relationship between the fault displacement accumulated on the topographic features and the offset of drainage systems, the topographic image processed from DEM data was reconstructed by reversing the possible displacement along the active fault trace. During the process of adjusting the displacement amount, the fit degree for all the topographic features is the most critical factor to determine the maximum cumulative offset. A reasonable fit degree for the upstream and downstream of Daxiahe River and Taohe River, and other associated topographic features along WQLF was obtained after removing the ~18 km displacement clockwisely (Fig. 5.2b). The displacement of ~18 km recorded by the tributaries of Yellow River indicates an accumulation of left-lateral strike-slip offset due to the repeated fault slipping on WQLF. In addition, according to positively-related linear relationship between upstream length and offset amount (Matsuda, 1975), systematic deflection and/or offset of gullies and

rivers for which have a relatively short upstream length have useful information. As shown in the topographic images (Figs. 5.3 and 5.4a), the deflection and/or offset of gullies whose upstream lengths vary from tens to thousands of meters were analyzed. It is evident that these gullies have been systematically offset sinistrally along the main fault trace of the WQLF with the displacement amount varying from 70 m to 390 m as recorded by the eighteen representative gullies (Fig. 5.3). Fault scarps facing the upstream are continuously developed along the main fault trace, accompanying with the sinistral offset of gullies (Figs. 5.3 and 5.4).

In general, systematic deflection of stream channels reaches the assumption that old rivers accumulate larger offsets, young rivers accumulate smaller offsets. It would be of higher reliability to interpret the deflected stream channels with various magnitudes of offset amount. The maximum cumulative offset of ~18 km recorded by Yellow River and its tributaries and the offset of tens to hundreds of meters indicated by gullies mirror the cumulative process and nature of repeated fault slipping along active strike-slip fault.

The systematic deflection of stream channels is often accompanied by other active tectonic landforms such as deflected mountain ridges, terraces, alluvial fans and other associated typical topography such as fault saddles (Fig. 5.4c–d) and fault scarps facing the upstream and downstream (Fig. 5.4e–f).

5.5. Structural features

Geological and topographic information that record the deformation history of active faulting is generally preserved at the ground surface, associated sediments and fault damage zone (Yeats et al., 1997), which help understand the deformation characteristics,

slip sense and paleoseismic slipping produced by active faults. To observe the fault structure and determine the slip sense of the WQLF, three representative fault outcrops were excavated and smoothed. Generally, the main fault developed along the contact zone between basement rock and unconsolidated or poorly-consolidated sediments (Figs. 5.5–5.7). Occasionally, branch faults subparallel to the main fault developed within the sand-gravel deposits, and thus disturbed the bedding structure of sediments to be tilted (Fig. 5.7).

At Loc.1 (see Fig. 5.1b for location), the fault outcrop was discovered under a fault scarp and developed along the contact zone between basement rock and Quaternary sediments with a sharp boundary. The main fault plane strikes N55°E–N60°E and dips to the southwest with a dipping angle of 75°–80°, which can be traced for ~100 m eastward along the fault scarp. Between the contact zone, the fault damage zone is composed of cataclastic rocks comprising fault gouge and fault breccia with a width of ~40 cm (Fig. 5.5d). Striations on the main fault plane indicate a horizontal-slip is dominant with a ratio of horizontal versus vertical motion of approximately 2~3:1 with the southwest-side uplift (Fig. 5.5e).

At the western tip of the systematically deflected gullies at Loc.2, one fault outcrop was observed (Fig. 5.6, see Fig. 5.3b for location). A series of fault scarps facing uphill cut through the ground surface into highland with an explicit linear trace (Fig. 5.6a). The active fault developed along the contact zone between basement rock and late Quaternary colluvial deposits, and thrusted southward upon the sediments (Fig. 5.6b–c). The colluvial deposits composed of grayish-brown sand-gravel, light greyish silt-soil and surface soil formed the footwall of fault plane on the south side (Fig. 5.6c). The main fault plane strikes N75^{o} W–N82^{o} W and dips to the north with a steep dipping

angle of ~85°, on which the striations were observed and measured (Fig. 5.6d–e). These structural features indicate a strike-slip dominated movement with little thrust component. The organic soil sample collected from the colluvial deposits yielded the ^{14}C age of 12005–11760 yr Cal BP (sample C01) (Fig. 5.6c and Table 5.1), indicating the late Pleistocene fault activity on WQLF.

Analogously, the fault outcrop at Loc.3 was observed at the western end of the systematically deflected gullies similar with that at Loc.2 (see Fig. 5.3d for location). The main fault F1 was exposed along the contact zone between basement rock and alluvial deposits, which controlled the deposition and accumulation of alluvial sand-gravel (Fig. 5.7a–b). The sand-gravel deposits are mainly composed of the poorly-sorted angular pebbles varying in size from several millimeters to ~50 cm in diameter (Fig. 5.7c–d). The bedding structure of alluvial deposits could be defined by the graded sedimentary sequences and the re-oriented gravels. Between F2 and F3 faults, the bedding was disturbed to be tilted with a dipping angle of ~45° from the horizontal layer, the gravels bounded on the fault plane were dragged and re-oriented parallel or subparallel to the fault planes of F2 and F3 (Fig. 5.7e-f). In order to determine the deformation age of alluvial deposits, the fine-grained calcareous soil was collected from the sub-horizontal sand-gravel layer, yielding a ^{14}C age of 9595–9535 yr Cal BP (sample C02) (Fig. 5.7e and Table 5.1) and indicating the Holocene activity of the WQLF.

5.6. Dating of deformed geomorphic surface markers

On the basis of remote sensing interpretation and field observation, the deformed geomorphic surface markers that were offset by the activity of the WQLF were defined

through associated faulted landforms and structural analyses. Generally, the fault scarps that cut through an alluvial fan and terrace and that offset rivers or gullies could be observed. To determine the formation ages of the deformed geomorphic surface markers and calculate the slip rate of the WQLF, the sidewalls of fluvial terrace were excavated and smoothed to observe the sedimentary sequences (Figs. 5.8–5.9, see Fig. 5.1b for locations). Four samples of organic soil for radiocarbon dating were collected at the base of the dark soil layer and alluvial sand-gravel deposits in these two sites. Similar sedimentary sequences were observed in the two stratigraphic profiles characterized by the sedimentary transition from alluvial sand-gravel to fluvial terrace fine-grained soil. The upper part of sampling exposure is continuously deposited dark soil or yellow-brownish loess with rich organic material, and the lower part gradually transits to alluvial sand-gravel with a sedimentary boundary (Figs. 5.8–5.9). According to the basic principle of sedimentary geology, the alluvial fan deposits composed of angular gravels and companied with silt-sand generally accumulate at the outlet in the piedmont area. Subsequently, the stream channel starts to form with unceasing lateral erosion and deepening riverbed. The alluvial fan begins to evolve towards the alluvial terrace, the corresponding sediments change from the coarse-grained poorly-rounded gravels to the fine-grained soil, manifesting the abandonment of alluvial fan surface. Therefore, the radiocarbon dating results of organic soil samples collected at the bottom of dark soil layer have the temporal proximity with the abandonment age of alluvial fan and the initiation time of alluvial terrace considering the timely and continuous deposition.

The interpreted maps of these topographic images were achieved by analyzing the geomorphic features and elevation data. The different terrace surface could be discerned clearly after changing the viewing perspective and exaggerating the vertical scale,

which were also confirmed by field observations.

At site 1 between the Daxiahe River and Taohe River (Fig. 5.8, see Fig. 5.2a for location), the active fault trace could be defined by the continuously-developed fault scarps as shown in 3D topographic image (Fig. 5.8a). Offset gullies and mountain ridges with the typical scissoring structures characterized by the oppositely-dipping fault scarps was observed in the field (Fig. 5.8b), which can be traced continuously for ~200 m eastward to another typical site with deflection of a stream channel and fault scarps perpendicular to the water flow (Fig. 5.8c). The channel was horizontally offset of 6.9± 0.3 m in sinistral (Fig. 5.8d). The sidewall of terrace T1 was dug into the inside of 20 cm to reveal the fresh exposure wall. The sedimentary sequences gradually transform from coarse-grained sand-gravel to fine-grained dark soil. Two organic soil samples were collected at the top and bottom of alluvial sand-gravel at depths of ~0.9 m and 1.2 m, yielding the ^{14}C ages of 2350–2310 yr Cal BP (sample C05) and 2735–2470 yr Cal BP (sample C06), respectively (Fig. 5.8e, Table 5.1).

Similarly, at site 2 in the central section of WQLF (Fig. 5.9, see Fig. 5.2a for location), faulted geomorphology with systematic offset of gullies and terraces are well-preserved along the active fault trace (Fig. 5.9a–b). Continuously-distributed fault scarps perpendicular to the water flow cut through the terrace, accompanying the deflection of stream channels with the offset amount of tens of meters (Fig. 5.9b). The terrace and stream channel was horizontal offset about 35 ± 2 m along WQLF (Fig. 5.9c). Stratigraphic sequences indicate a similar transformation from alluvial sand-gravel to fluvial terrace soil as revealed by a naturally exposed outcrop wall. Two dark greyish organic soil samples were collected at the top and bottom of alluvial sand-gravel, which yielded the ages of 13480–13365 yr Cal BP and 17180–16975 yr Cal BP (samples C07

and C08) (Fig. 5.9f and Table 5.1), respectively.

5.7. Discussion

5.7.1. Late Pleistocene strike-slip rate

Using the displacement of fluvial terrace and the corresponding age of deformed geomorphic surface marker, the strike-slip rate of the WQLF could be constrained. At site 1, the dating result of sample C05 collected at the bottom of the dark soil layer is close to the formation age of alluvial terrace. Here, the time gap between the fluvial terrace formation and earliest soil deposition was ignored considering the timely deposition, which has been widely accepted by previous studies (Zhang et al., 1988a; Kirby et al., 2007; Cowgill et al., 2009; Li et al., 2016). That is, the displacement recorded by the fixed stream channel (D_C) and that accumulated by the contemporaneous fluvial terrace (D_T) has a roughly consistent offset amount after the abandonment of alluvial fan (Fig. 5.10). Thus, the age of sample C05 with the result of 2350–2310 yr Cal BP was suggested to be the formation age of alluvial terrace, earlier than the dating result of 2735–2470 yr Cal BP of sample C06 collected at the bottom sand-gravel layer. With the offset amount of 6.9 ± 0.3 m, the left-lateral strike-slip rate of the WQLF was estimated to be 2.5–3.0 mm/yr. Similarly, radiocarbon dating results of samples 07 and 08 collected at the top and bottom of sand-gravel layer at site 2 can constrain the formation timing of alluvial terrace. With the offset amount of 35 ± 1.8 m, the strike-slip rate of the WQLF was constrained to be 2.0–2.6 mm/yr (Table 5.2), which is comparable with the result reported from the local segment of WQLF (Li et al., 2007).

Although the slip rates obtained at these two sites have a similar value, the result of

2.0–2.6 mm/yr achieved at site 2 should have a higher reliability than that obtained at site 1 due to the larger offset amount accumulated by the river and fluvial terrace. The characteristic offset of ~7 m at site 1 was probably generated by one or two fault slipping events, however, the displacement of ~35 m at site 2 recorded more seismic cycles and fault slipping events. Therefore, the estimated slip rate obtained in site 2 has a large ambiguity and the true slip rate of WQLF should be 2.0–2.6 mm/yr.

The result demonstrates that the WQLF exhibits a relatively low strike-slip rate since late Pleistocene when compared with the western Kunlun Fault and Altyn Tagh Fault with a slip rate of 10–30 mm/yr (Kirby et al., 2007; Peltzer and Saucier, 1996). In addition, the strike-slip rate of the Kunlun Fault dramatically decreases eastward to ~3 mm/yr at its eastern tip near the WQLF with an average gradient of ~1 mm/100 km (Kirby and Harkins, 2013; Lin and Guo, 2008), displaying a non-uniform slip rate along different segments of active faults. Therefore, the result suggests that displacement along the Kunlun Fault is not propagated beyond the eastern margin of the Tibetan Plateau, although the western and central segment of Kunlun Fault is responsible for the eastward extrusion of central Tibetan Plateau (Kirby et al., 2007). The common characteristic of low strike-slip rate of the eastern KLF and WQLF is likely to result from roughly similar regional tectonic background in the northeastern Tibetan Plateau and the geodynamic role in absorbing and accommodating the plateau intracontinental deformation. Between the two regional-scale strike-slip faults, some secondary faults were also reported to have a low strike-slip rate of < 1 mm/yr (Han et al., 2001; Yu et al., 2012; Liu, 2012; Zheng et al., 2016).In the past two decades, the Global Navigation Satellite (GNSS) measurement has been widely applied to quantitatively constrain the velocity of block motion in the Tibetan Plateau (e.g., Wang et al., 2001; Zhang et al.,

2004), which provides a reference to estimate the slip rate of active faults. A left-lateral strike-slip rate of 2.0–2.5 mm/yr for the eastern KLF and 1–2 mm/yr for WQLF were suggested by the result of GPS obervations (Zhang et al., 2004; Zheng et al., 2016), which is comparable with that inferred from the geologic and geomorphologic evidence with the late Pleistocene strike-slip rate of 2.0–2.6 mm/yr as documented above.

5.7.2. Initial timing of left-lateral strike-slip faulting, maximum cumulative displacement and its tectonic implications

In the west Qinling mountainous area, most gullies or rivers generally developed only one or two level fluvial terraces under the joint effect of steep topographic relief and small stream order as revealed at sites 1–2. In geometry, most of these gullies intersect with the trace of the WQLF at a high angle even perpendicular to the general trend of the active fault, and were systematically offset and/or deflected in sinistral when crossing the WQLF with the displacement amount of smaller than hundreds of meters in general, tending to concentrate in the range of several meters to dozens of meters.

A previous study reported that the WQLF has experienced a long-term tectonic evolution since the Caledonian period (Clark et al., 2010). Low-temperature thermo-chronology results including apatite and zircon (U–Th)/He and apatite fission-track ages can provide constraints on the faulting time by recording the exhumation events from the shallow crust. Increased exhumation rates were discovered at ~8–5 Ma on the eastern segment of the Kunlun Fault and ~10–8 Ma along the eastern tip of the Haiyuan Fault in Liupanshan area (Zheng et al., 2006), manifesting a roughly consistent deformation age of the Kunlun Fault and the Haiyuan Fault. The result probably suggests that the present-day geometric and kinematic configuration of these

active faults in the northeastern Tibetan Plateau has been established since middle Miocene (Jolivet et al., 2003; Duvall et al., 2013). The WQLF, located between the Kunlun Fault and the Haiyuan Fault, is oriented parallel or subparallel to them with the identical slip sense of left-lateral motion. Therefore, it could be assumed that these three faults should have a generally synchronous initiation time of left-lateral faulting under a similar tectonic setting in the northeastern Tibetan Plateau. It is the northeastward growth and expansion of the Tibetan Plateau that causes the left-lateral strike-slip faulting on these WNW-trending active faults under the NE- to ENE-trending compressive stress (Zhang et al., 2004). These large-scale strike-slip faults bounding the plateau margins appear to exhibit a nearly simultaneous response to the collisionbetween the Indian and Eurasian plates, and the initiation time of left-lateral shearing concentrated on the largest range of ~13–5 Ma (Wang et al., 2009). Thereby, the left-lateral strike-slip activity of the WQLF is likely to have started since ~13–5 Ma.

The maximum cumulative offset recorded by the tributaries of Yellow River was suggested to be ~18 km as discussed above (Fig. 5.2). On the other hand, the bending of mainstream channel of Yellow River is not so evident as these two tributaries. The Yellow River changed its flowing direction from northward to northwestward, and then turned to the northeast when travelling across the WQLF (Fig. 5.1b). As reported by previous studies, the morphology of stream channels where they cross a fault varies significantly from place to place on the active fault (Wallace, 1968). Apart from the influence of tectonic movement, the geometric pattern of channels could be strongly affected and re-shaped due to the difference of local conditions such as local geology, channel density, width of crush zone, slope gradient, stream incision and sedimentation, regional aggradation or degradation associated with subsidence or uplift (Huang, 1993;

Matsuda, 2004). Therefore, it is indeed difficult to make an authentic and objective assessment about which factor affected the morphology of stream channel at the deflected point. With the assumption that the slip rate of the WQLF is generally steady in this range of 2.0–2.6 mm/yr since its initiation as a left-lateral strike-slip fault during the past ~13–5 Ma, the total accumulated displacement on WQLF is estimated to be 10–34 km. The result is comparable with the maximum cumulative offset of ~18 km recorded by the Yellow River drainage systems.

In the previously-published paper (Chen and Lin, 2019a), the small scale geological map (1:1500000) was modified and reconstructed to restore the maximum cumulative displacement on the WQLF. However, oversimplication was done in the geological reconstruction to match deflected points at both sides of the WQLF. Therefore, there should a large uncertainty in the estimation of the cumulative displacement given in Chen and Lin (2019a). More work need to be done to confirm the maximum cumulative offset on the WQLF in the future.

5.8. Conclusions

Based on the analyses of displaced late Pleistocene geomorphic features andcorresponding radiocarbon dating results, the late Pleistocene left-lateral strike-slip rate of the WQLF was determined. Integrating the regional active tectonic characteristics of the northeastern Tibetan Plateau, the following conclusions are obtained:

1) Mountain ridges, gullies and late Pleistocene alluvial fans and terraces have been systematically deflected and/or offset sinistrally on the WQLF.

2) The late Pleistocene–Holocene strike-slip rate of the WQLF is estimated to be 2.0–

2.6 mm/yr. Compared to other major active strike-slip faults such as the Altyn Tagh Fault and the Kunlun Fault with high slip rate of > 10–20 mm/yr in the northern and northeastern Tibetan Plateau, the WQLF exhibits a relatively low strike-slip rate of < 3 mm/yr, which might be related to the limited convergence transfer owing to the fact that most of the strain energy has been absorbed and diffused by continuous crustal deformation in the northeastern marginal zone of the Tibetan Plateau, rather than only the localized deformation along strike-slip faults.

Table 5.1. Radiocarbon dating results.

Sample Code	Beta ID[a]	Conventional ages[b] (yr BP)	Calibrated calendar Age[c] (Cal BP)	Description
C01	474005	10,180 ± 30	12005-11760	Organic soil
C02	474007	8620 ± 30	9595–9535	calcareous soil
C05	473990	2300 ± 30	2350-2310	Organic soil
C06	473991	2500 ± 30	2735-2470	Organic soil
C07	464315	11,600 ± 40	13480-13365	Organic soil
C08	464316	14,050 ± 40	17180-16975	Organic soil

[a]Samples were analyzed at Beta Analytic Inc., USA.

[b]Radiocarbon ages were measured using AMS and are referenced to the year A.D. 1950. The analytical uncertainties are reported at 2σ.

[C]Dendrochronologically calibrated calendar age by Method A from CALIB Radiocarbon Calibration Version 7.0 (Stuiver and Reimer, 1993).

Table 5.2. Dating ages of deformed geomorphic surface markers and the corresponding offset amounts.

Locations	Geomorphic features	Conventional ages (yr BP)	Calibrated calendar age (Cal BP)	Offset amount (m)	Slip rate (mm/yr)
Site 1	Terrace	2300 ± 30	2350-2310	6.9 ± 0.3	3.0 ± 0.1
Site 2	Terrace	11,600 ± 40	13480-13365	35.0 ± 1.8	2.6 ± 0.1

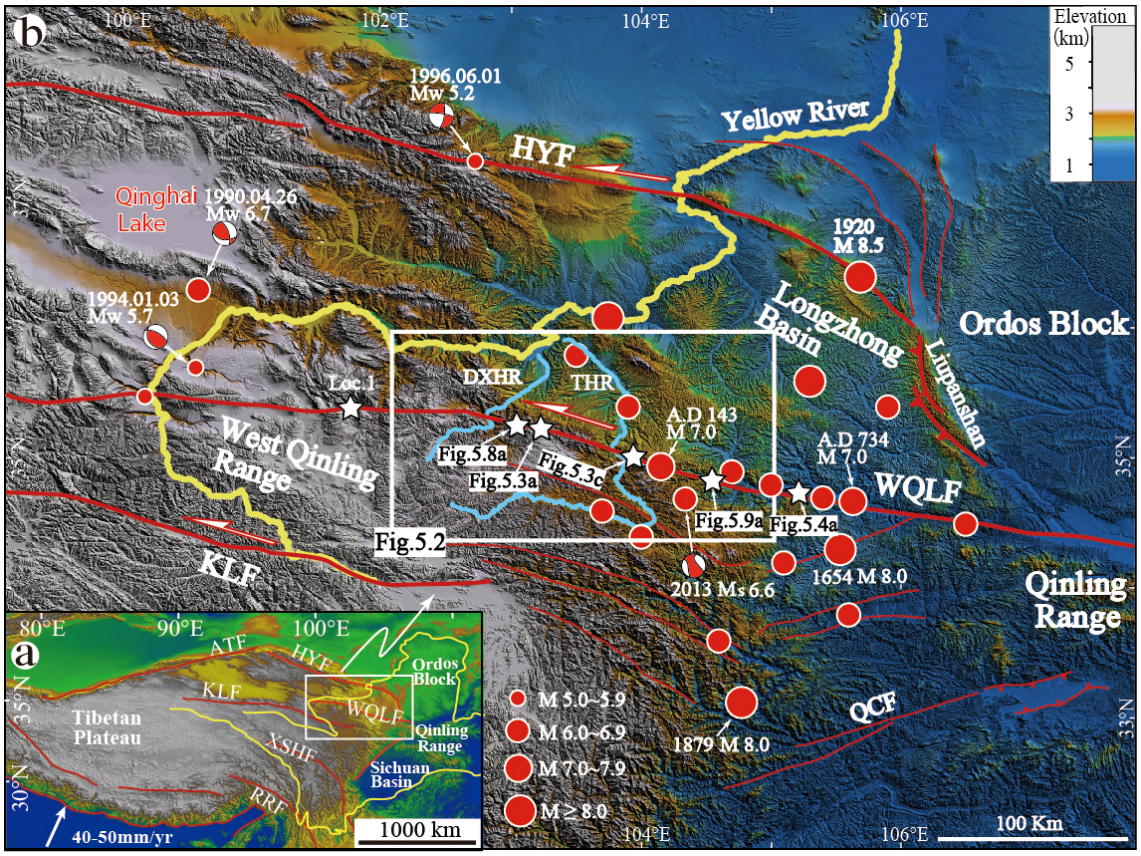

Fig. 5.1. Tectonic background and topographic features of the study area. (a) Color-shaded relief map showing the location of the study area and the major active faults within and surrounding the Tibetan Plateau. Motion velocity of the Indian plate is cited from Zhang et al. (2004). (b) Color-shaded relief map showing the topographic and tectonic features of the study area. Historic earthquake information is from the Earthquake Disaster Prevention Department of China Earthquake Administration catalogue (EDPDCEA, 1995) and focal mechanism are from the Global Harvard CMT catalogue (http://www.globalcmt.org). Note the offset and/or deflection of Daxiahe River and Taohe River. The acronyms used in the figure are defined as follows: ATF: Altyn Tagh Fault; KLF: Kunlun Fault; HYF: Haiyuan Fault; WQLF: West Qinling Fault; QCF; Qingchuan Fault; XSHF: Xianshuihe Fault; RRF: Red River Fault; THR; Taohe River; DXHR: Daxiahe River.

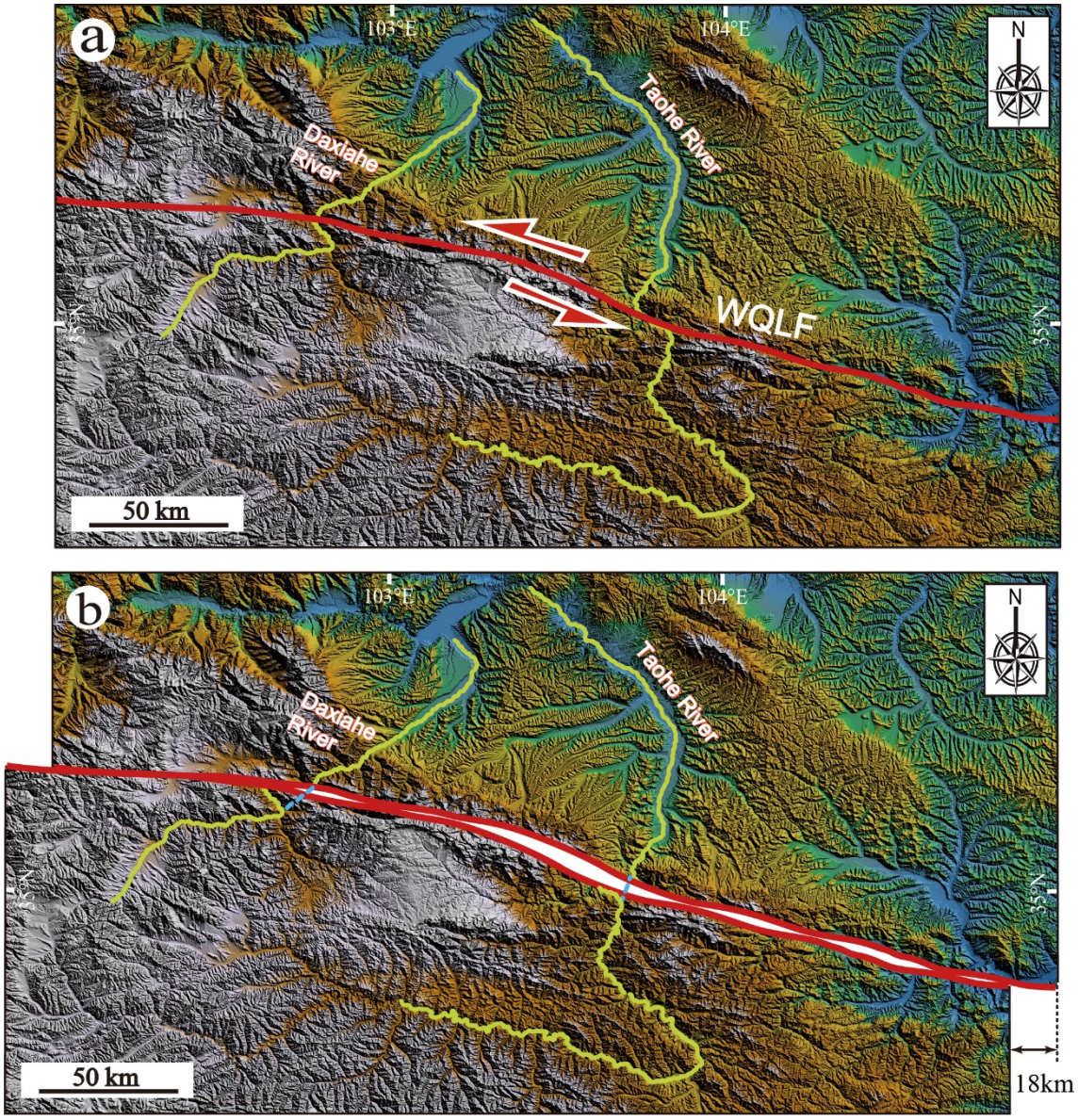

Fig. 5.2. Color-shaded relief maps showing the reconstructed process of deflected drainage systems. (a) STRM 30 PLUS 30-m-resolution color-shaded relief map showing the topography and the main tributaries of Yellow River drainage systems (see Fig. 5.1b for location). (b) Restored drainage systems after removing the ~18 km sinistral displacement along the WQLF.

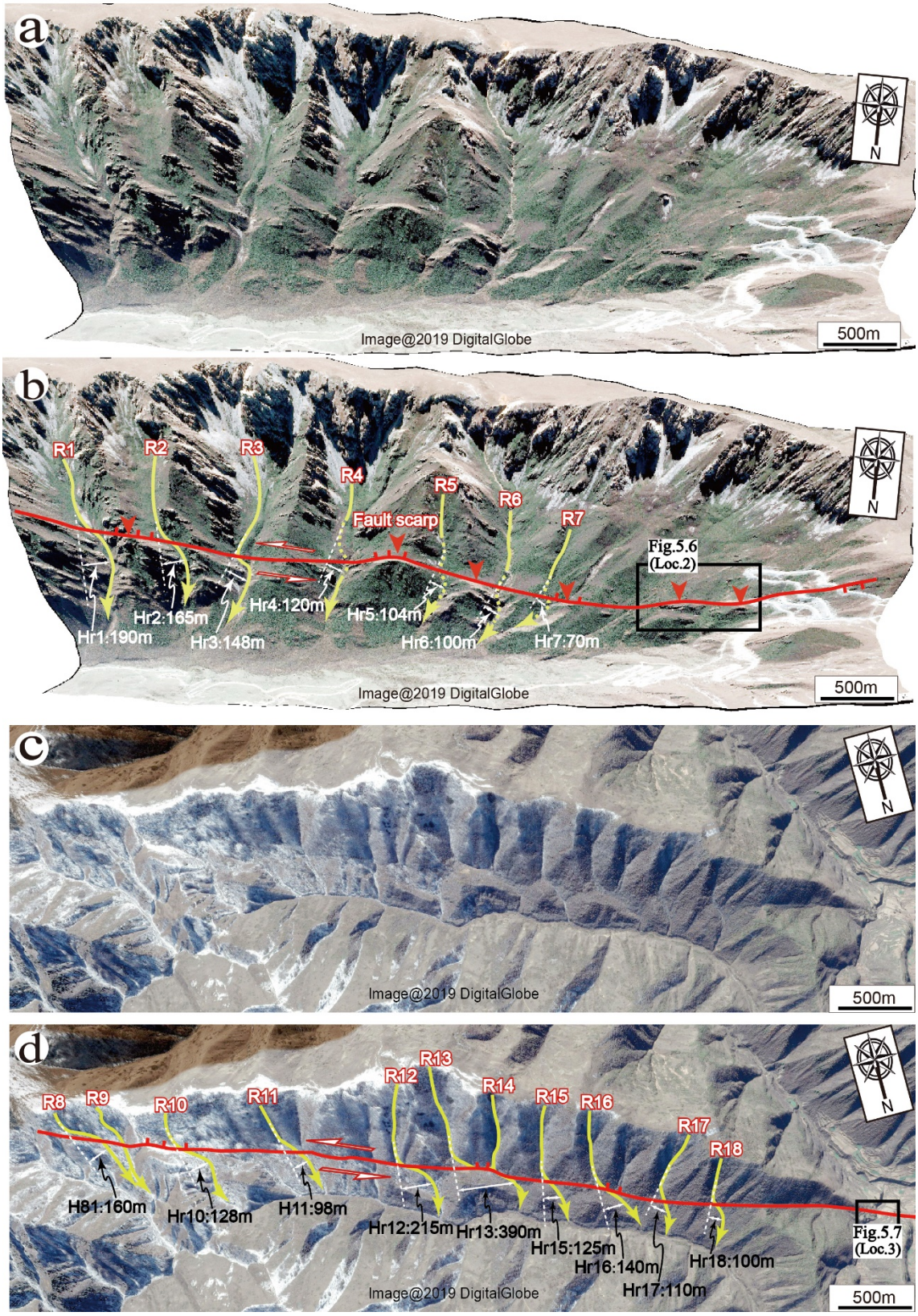

Fig. 5.3. Google Earth images showing systematic offset of gullies along the

WQLF with displacement amounts varying from 70 m to 390 m (see Fig. 5.1b for location). R1–R18 are deflected stream channels and Hr1–Hr18 are corresponding offset amounts. Short red lines indicate the dipping direction of the fault scarps. (a) and (c) are the original Google Earth images, and (b) and (d) are the corresponding interpreted maps.

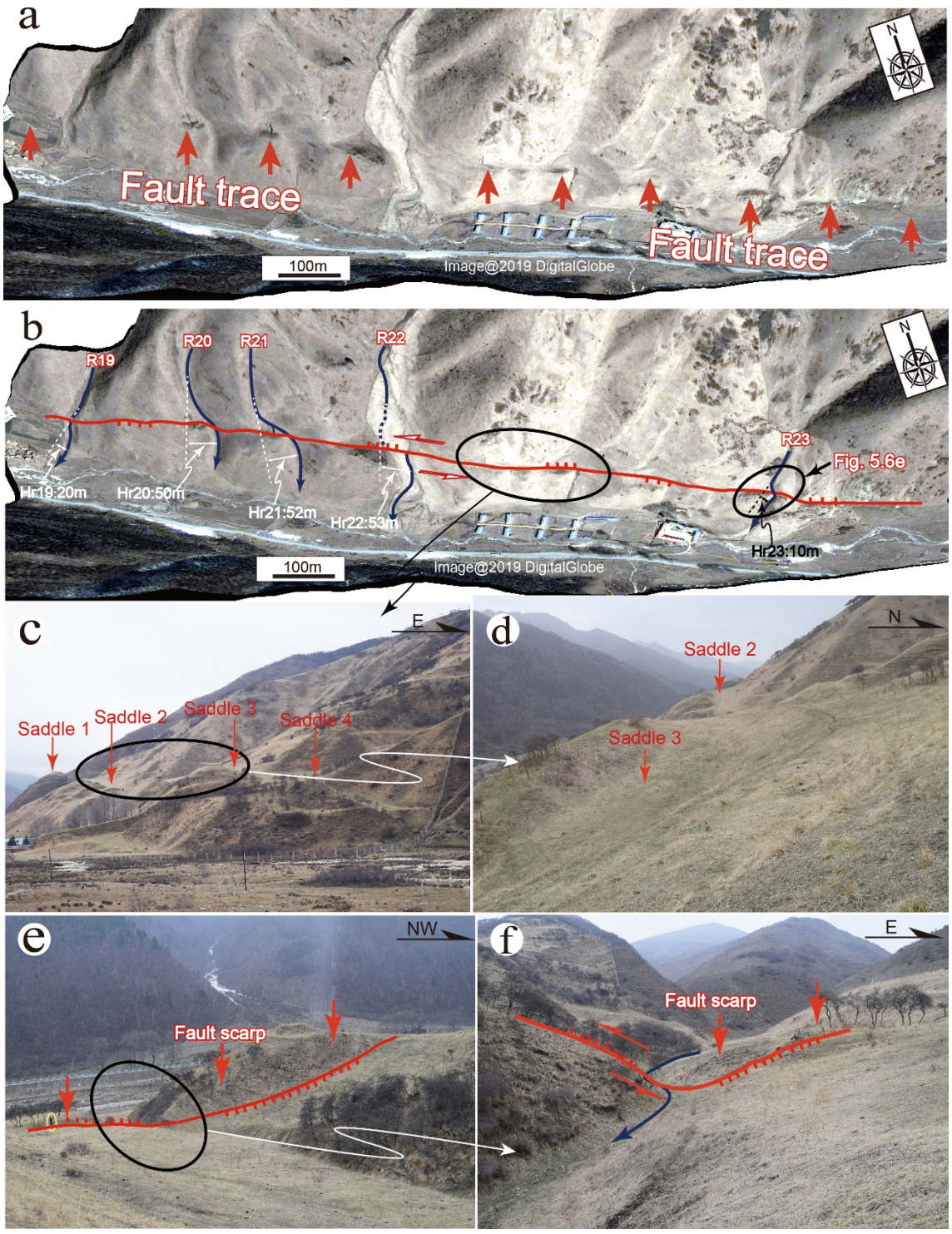

Fig. 5.4. 3D Google Earth images and photographs showing tectonic landforms and field outcrops associated with left-lateral faulting of the WQLF (see Fig. 5.1 for location). (a) Google Earth image showing the active fault trace along the WQLF. (b)

Systematic offset of geomorphological markers including stream channels and mountain ridges. R19–R23 are deflected stream channels and Hr19–Hr23 are corresponding offset amounts. (c) Continuous faulted saddles. (d) Close-up view of saddles 2 and 3. (e–f) Offset gully and fault scarps. Short red line indicates the facing direction of the fault scarp. The blue line with arrow indicates the stream channel.

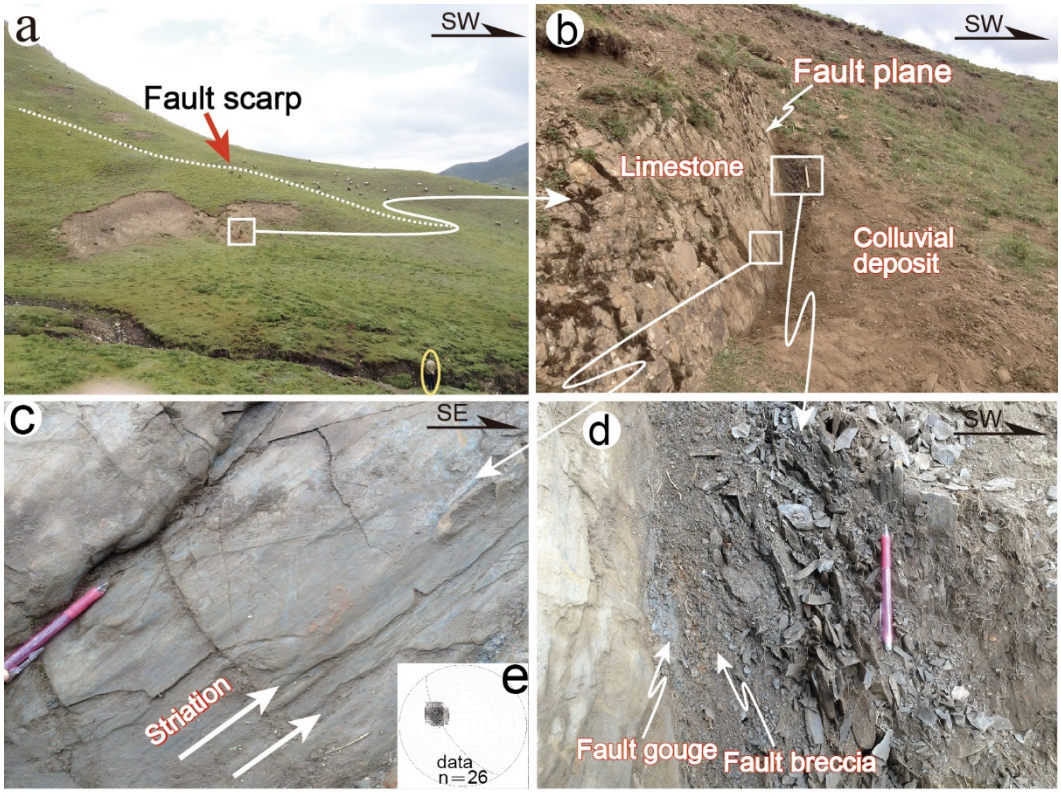

Fig. 5.5. Field photographs showing the fault outcrop observed at Loc. 1 (see Fig. 5.1b for location). (a) Overview of the fault outcrop developed along the fault scarp. The white dotted line indicates the topographic slope, note the change of slope angle. (b) Active fault developed along the contact zone between the basement rock and the colluvial deposits. (c) Striations on the main fault plane showing the principal strike-slip motion with thrust component along the WQLF. (d) Fault damage zone consisting of fault gouge and fault breccia. (e) Stereographic projection of the striations measured on the main fault plane.

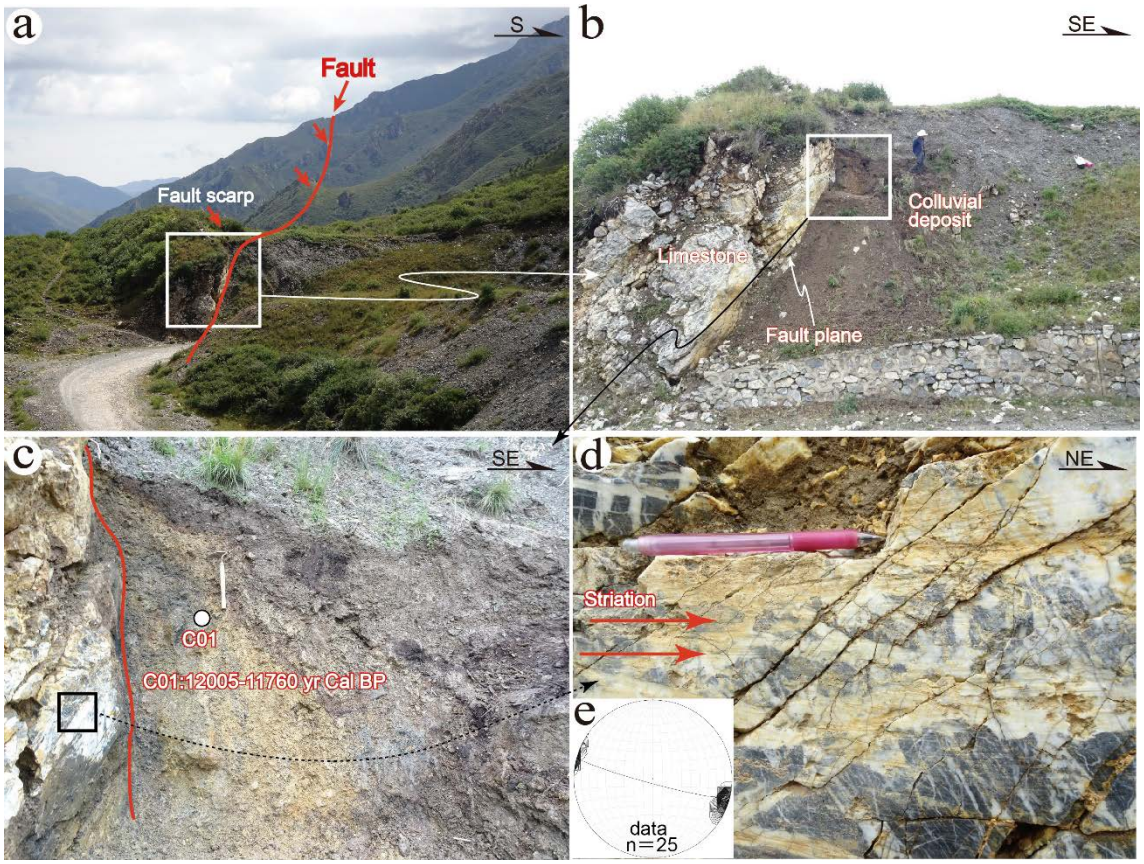

Fig. 5.6. Field photographs showing the fault outcrop observed at Loc. 2 (see Fig. 5.3b for location) (a) Active fault developed along the contact zone between the basement marble and the late Quaternary sediments with lineament fault scarps extending into the highland. (b) Photographs showing the exposure position along the contact zone. (c) Close-up view of (b) showing the structural features of the fault zone. (d) Striations on the main fault plane showing the dominated strike-slip motion of the WQLF. (e) Stereo projection of the striations measured on the main fault plane.

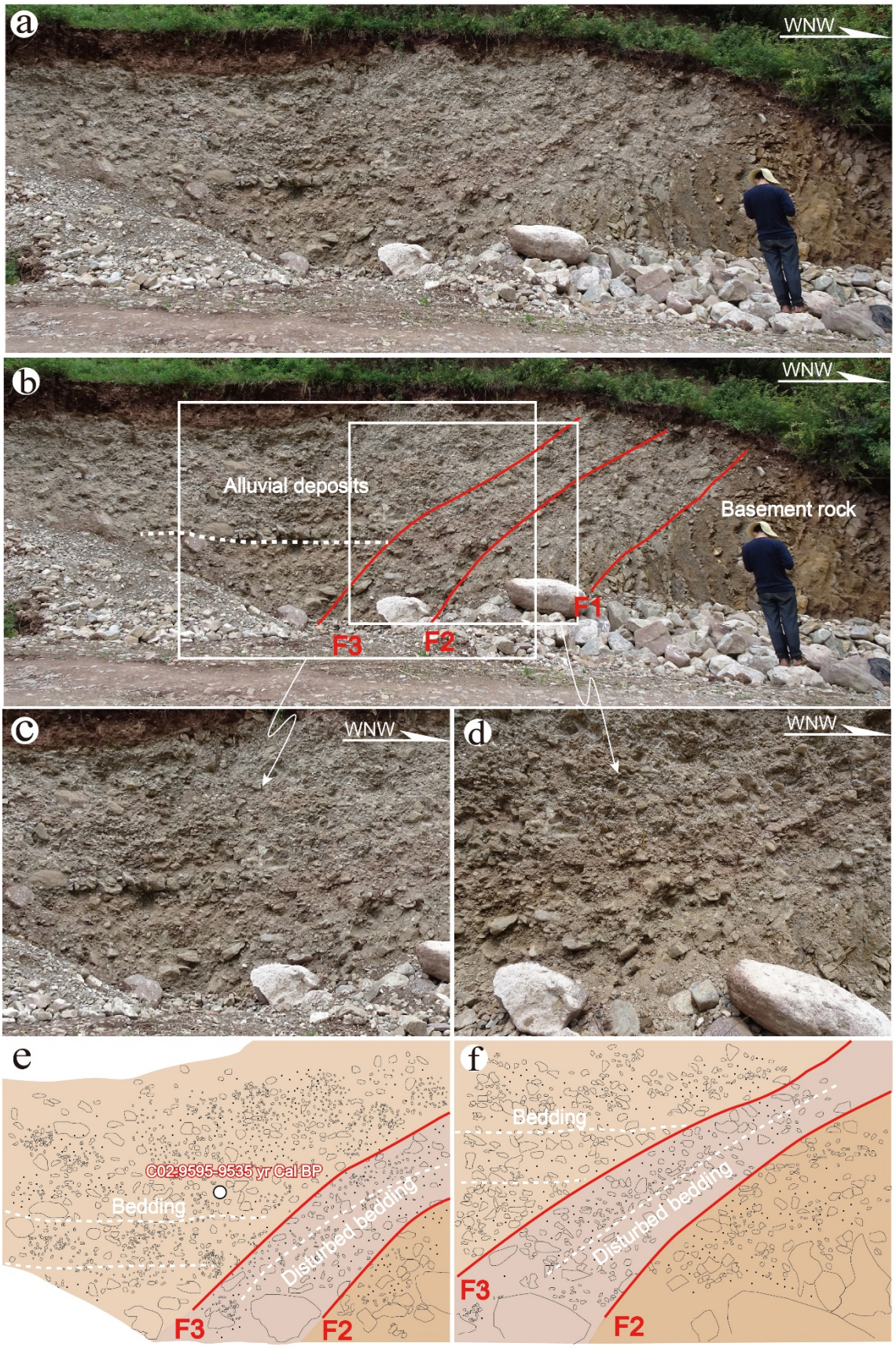
a
WNW
b
WNW
Alluvial deposits
Basement rock
F1
F3
F2
c
WNW
d
WNW
e
C02:9595-9535 yr Cal BP
Bedding
Disturbed bedding
F3
F2
f
Bedding
Disturbed bedding
F3
F2

Fig. 5.7. Field photographs showing the fault outcrop observed at Loc. 3 (see Fig. 5.3d for location) (a) Photographs showing the overview of field outcrop. (b) Interpreted map showing the faults. (c) Disturbed bedding structure due to the activity of the F2 and F3 faults. (d) Gravels bounded on the F2 and F3 faults were dragged and re-oriented parallel to the fault plane. (e) Sketch of (c). (f) Sketch of (d). The white dotted line indicates the bedding of alluvial fan deposits.

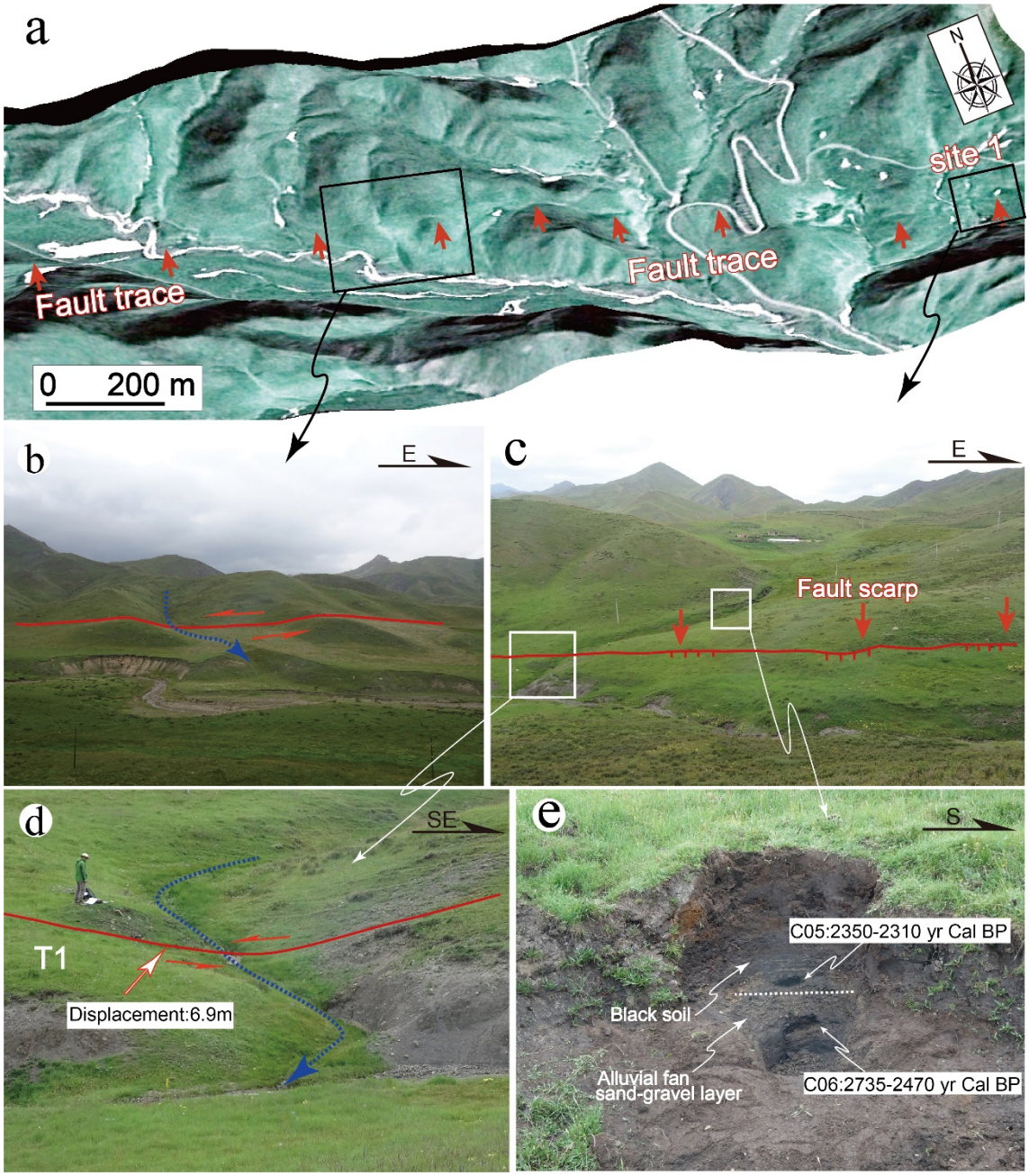

Fig. 5.8. 3D topographic image and field photographs showing associated tectonic geomorphology along the WQLF. (a) 3D topographic image showing the active fault trace indicated by fault scarps, offset gullies and mountain ridges (see Fig. 5.2a for location). (b) Offset gullies and mountain ridges. (c–d) Field outcrops of fault scarps and an offset stream channel. (e) Sedimentary sequences of terrace deposits and ^{14}C

sampling locations. The blue dotted line in (b) and (d) indicate the stream channel and the white dotted line in (e) represent the abandoned boundary of the alluvial fan deposit.

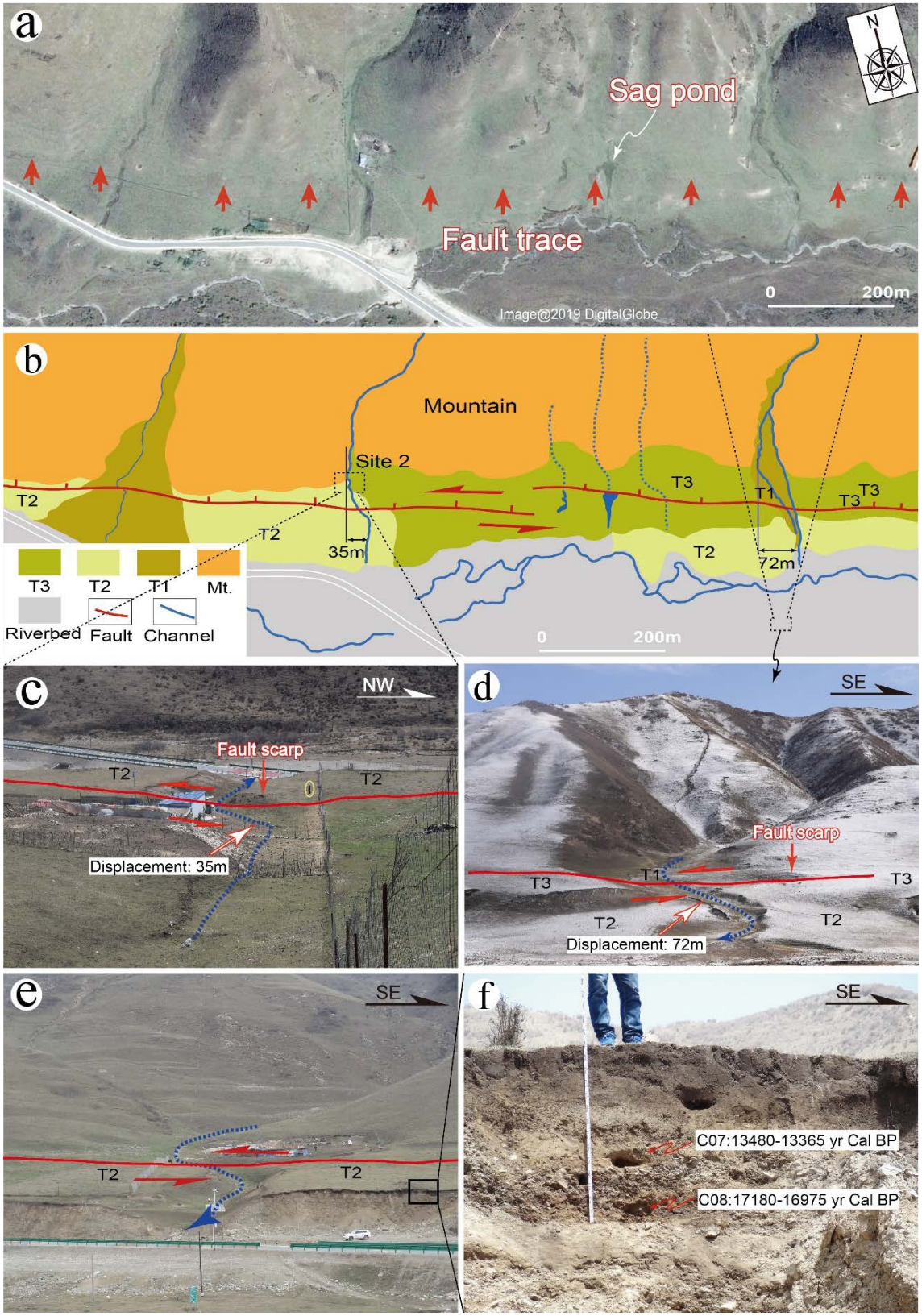

Fig. 5.9. Google Earth image and field photographs showing the faulted landforms

and field outcrop. (a) Active fault trace indicated by the fault scarps and systematic deflection and/or offset of stream channels (see Fig. 5.2a for location). (b) Interpreted geomorphic map of (a). The short red line indicates the facing direction of fault scarp. (c–d) Photographs showing the offset stream channels and terrace with the offset amount of 35 m and 72 m, respectively. Noting the fault scarp perpendicular to the water flow. (e–f) ^{14}C sampling sites and sedimentary sequences of terrace deposit.

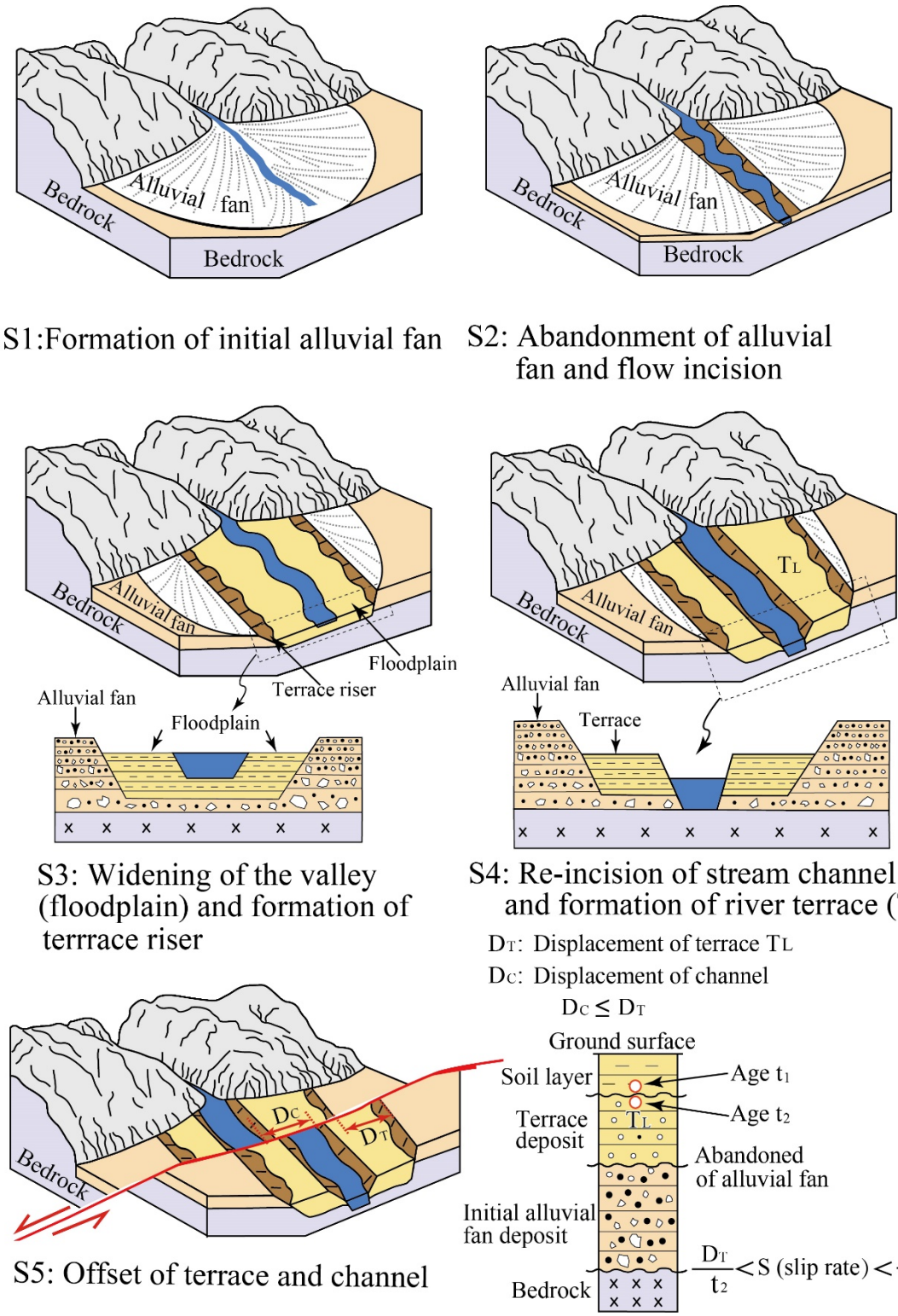

Fig. 5.10. Schematic diagram to explain the principle of calculating slip rate. D_c and D_T represent the offset of the stream channel and the terrace T_L, respectively. t_1 and t_2 represent the corresponding ages of geomorphic surface marker. S means the slip rate of

the strike-slip fault. In general, $D_c \leq D_T$, but D_c is considered to be close to D_T in the causes of Figs. 5.8 and 5.9, because the streams are well trapped in the incised channels.

Chapter 6. Paleoseismic study on the West Qinling Fault

6.1. Abstract

The West Qinling Fault (WQLF), one important active strike-slip fault in the northeastern Tibetan Plateau, has frequently triggered large historical earthquakes. Topographic analysis associating with active faulting and trench excavations, together with radiocarbon dating results reveal the followings: i) the most recent surface-rupturing earthquake (E1) occurred after 760–471 yr Cal BP. If no other large historic earthquakes are missing in the catalogue, this event can only correspond to the 1654 M 8.0 Tianshui earthquake., in this case, the source seismogenic fault of the 1654 Tianshui earthquake is not the Lixian–Luojiabao fault (LLF) as previously reported, but the WQLF is. ii) the penultimate large earthquake (E2) occurred in the period of 2693–760 yr Cal BP. iii) the third recent large earthquake (E3) occurred in the period of 10229–6032 yr Cal BP with a higher probability in this range of 9005–8596 yr Cal BP. iv) Given the wide time-span for E3 and the recurrence discipline of characteristic fault, another paleoearthquake possibly occurred in the period of 8596–6032 yr Cal BP. Then, the above E3 becomes E4 and occurred in the period of 9005–8596 yr Cal BP. Therefore, three or four large earthquakes occurred during the past ~9000 years on WQLF, suggesting an average recurrence interval of large earthquakes of 2250–3000 years. The findings concerning with the recurrence interval of large earthquakes on WQLF would provide valuable information for the re-assessment of seismic potential, also for a better understanding of earthquake mechanism and geodynamic implications

in the northeastern Tibetan Plateau.

6.2. Introduction

The identification of source seismogenic fault of prehistoric or historic large earthquakes is an important research of active tectonics and source mechanisms. Due to the lacking of detailed historical and instrumental records and the long-term destruction and degradation resulting from human activities, it become difficult to recognize the coseismic surface rupture generated by individual historic large earthquake.

In contrast to the instrumentally-recorded modern earthquakes, the study of prehistoric or historic large-magnitude earthquakes relies mainly on the analyses of historical documents and field geological observations (Yeats et al., 1997). The geologic and geomorphological records associated with large morphogenic earthquakes can provide direct evidence of coseismic ground deformation, and therefore, can help assess the active tectonic characteristics and deformational behaviors of active faults (e.g., Wesnousky et al., 1984; Lin and Guo, 2008; Ren et al., 2018).

On 21 July 1654, the M 8.0 Tianshui earthquake struck the southern Tianshui city in Gansu province, China, resulting in enormous damage and huge casualties including more than 30000 deaths and uncountable injured and missing population (Lanzhou Institute of Seismology, SSB, 1993). The epicenter of this earthquake was identified in the transition zone between the Tibetan Plateau and the Ordos Block in the northeastern marginal zone of the Tibetan Plateau (Fig. 6.1). Based on the inferred seismic intensity map estimated from the building damage, a NE to NNE-trending long axis of seismic intensity was obtained (EDPDCEA, 1995). Under this background, previous studies deemed that the ENE-trending LLF, a left-lateral strike-slip fault with a total length of ca. 150 km, is the source seismogenic fault of the 1654 M 8.0 Tianshui earthquake

(Lanzhou Institute of Seismology, SSB, 1993; Han et al., 2001; Su et al., 2013; Yang et al., 2015; Yuan et al., 2017). Although the late Pleistocene–Holocene tectonic activity occurred on LLF was reported, the absolute and consolidated evidence indicating that the LLF is the source seismogenic fault of the 1654 Tianshui earthquake is still lacking. The details concerning with the surface deformation features including the coseismic surface rupture length produced by this earthquake are still unclear due to the lack of historical records and geological data. Furthermore, the 1654 Tianshui earthquake occurred in Ming dynasty with an elapsed time of ~360 years, the accurate records and comparison of building damage that were used to infer the seismic intensity may need to be re-examined.

The WQLF, as a mature active fault, is one of the main active strike-slip faults in the northeastern Tibetan Plateau, having produced many large earthquakes of magnitude ≥ 7.0 recorded by the instrumental and historical documents as documented in Chapter 4 and 5 (EDPDCEA, 1995).

In this study, the detailed topographic analyses of remote sensing images along the WQLF are presented. Based on the field observations, trench excavations and radiocarbon dating results, the main seismogenic fault of the 1654 M 8.0 Tianshui earthquake and the recurrence interval of large earthquakes on the WQLF are discussed.

6.3. Tectonic setting

The study area is located in the northeastern marginal zone of the Tibetan Plateau (Fig. 6.1b). The WQLF, striking WNW–ESE in the east segment and nearly E–W in the west segment with a total length of ~600 km, bounds the Longzhong Basin in the north with an average elevation of ~2000 m and the West Qinling Range in the south with

elevations higher than 3000 m as stated in Chapter 5 (Fig. 6.1b).

Historical records documented that large earthquakes of magnitude ≥ 7.0 including the AD 143 M 7.0 Gangu West earthquake, AD 734 M ≥ 7.0 Tianshui earthquake repeatedly occurred on the WQLF (Fig. 6.1b, EDPDCEA, 1995), indicating the attributes as a mature active fault. Based on the analyses of displaced geomorphic surface markers and radiocarbon dating results, the slip rate of the WQLF since late Pleistocene was estimated to be 2.0–2.6 mm/yr as documented in Chapter 5.

The LLF, striking ENE–WSW with a total length of ~150 km, is a left-lateral strike-slip fault composed of three right-stepping sub-segments (Han et al., 2001; Su et al., 2013). The average horizontal and vertical slip rate of LLF was reported to be 0.95 mm/yr and 0.35 mm/yr with the ratio of nearly 3:1 (Han et al., 2001). Apart from the 1654 M 8.0 Tianshui earthquake, no any other definable large earthquakes even minor earthquakes have ever occurred on the LLF according to the instrumental and historical records (Lanzhou Institute of Seismology, SSB, 1993).

6.4. Faulted geomorphology

To determine the trench sites and quantitatively assess the recent activity of the WQLF, the high-resolution Google Earth images and 3D topographic images are used to identify the active fault trace and the associated geomorphic features (Figs. 6.2–6.4). The offset amount of geomorphic markers can be directly measured from the images by recovering the offset rivers or gullies, mountain ridges, terraces and alluvial fans along the active fault trace indicated by fault scarps (Fig. 6.2–6.4). Typical tectonic geomorphic features associating with strike-slip faulting such as fault saddle and sag pond were observed at the sites where the offset rivers, gullies and fault scarps

facing-upstream were preserved well (Fig. 6.2).

The 3D reconstruction of remote sensing images is an excellent manner to contrast the abnormal topography, especially in discerning the vertical topographic relief. At the eastern segment of the WQLF, the main fault can be traced for ~2 km eastward along the continuously-distributed fault scarps facing the uphill (Fig. 6.2a, see Fig. 6.1b for location). Typical faulted landforms comprising the systematically offset gullies and mountain ridges, fault saddle and sag pond could be observed on the hillside (Fig. 6.2b–c). To the east, deflection of two gullies were observed with an offset amount of about 42 m and 10 m, respectively (Fig. 6.3a and c). In addition, several beheaded gullies bounded by WQLF developed in the south side of the active fault trace (Fig. 6.3b). The fault scarp extended eastward to the site where the latest alluvial fan surface was ruptured, indicating the most recent faulting event (Fig. 6.3d). To confirm that the topographic response was surely caused by faulting and identify the paleoseismic faulting events, one outcrop and two trenches were excavated and smoothed in the field. The details are shown below.

6.5. Outcrop observations

In the east, a fault outcrop was discovered under a fault scarp developed in piedmont area (Fig. 6.4a, see Fig. 6.1b for location). The active fault trace of the WQLF could be clearly defined by the continuously-distributed fault scarp facing-uphill as revealed by the 3D topographic image (Fig. 6.4a). The fault outcrop is developed at the site where the topographic slope sharply changes (Fig. 6.4b). The outcrop wall is mainly composed of brownish cataclastic basement rocks, colluvial coarse-grained gravels, light to dark grey soil layer and the overlying surface soil. Foliation structure developed in the

cataclastic basement rocks is parallel to the fault F1. Two colluvial wedges infilled by the poorly-sorted angular pebbles varying in the size from several millimeters to ~20 cm in diameter were bounded by F2 and F3 faults and their branches. Radiocarbon samples collected from the two colluvial wedges yield the 14C calibrated ages of 9700–9550 yr Cal BP and 9125–9005 yr Cal BP, respectively (sample C10 and C11, Table 6.1). The F2 and F3 faults terminate at the bottom of light grey soil layer, and overlain by the dark grey soil. The 14C sample was collected from the dark grey soil, yielding an age of 8595–8460 yr Cal BP (sample C09, Table 6.1). Therefore, the fault slipping event at this site is suggested to occur in the period of 9005–8595 yr Cal BP between the ages of the samples C11 and C09, close to or slightly after 9005 yr Cal BP.

6.6. Trench investigations

Before excavating trenches, the detailed filed investigation was conducted to observe the topographic characteristics associated with the active strike-slip faulting. A typical fault saddle bounded by the oppositely-facing fault scarps was observed (Fig. 6.5a, see Fig. 6.3a for location). The fault scarps with distinctly different vertical drop at the east side of the fault saddle were discovered, indicating repeated fault slipping on the WQLF (Fig. 6.5b). These fault scarps could be traced eastward over 2 km to the sites where the two trenches were excavated on both sides of the deflected gully (Fig. 6.5c, see Fig. 6.3c for location). In the east, the structural bulge or push-up structure similar to a coseismic mole track was observed (Fig. 6.5d).

Geomorphological, stratigraphic and structural features associated with seismic faulting are often used as indicators to identify paleoseismic events (Yeats et al., 1997; Lin et al., 2006). Among these markers, fault scarps developed on a young alluvial fan

and terrace, scarp-derived colluvium, infilled fissures, upward terminations of fault planes, offset and disturbance of sedimentary layers are the most widely-accepted criteria to identify the occurrence of paleoearthquakes (Lin and Guo, 2008), which are also used in this study. In order to constrain the timing of paleoseismic events, radiocarbon dating samples were collected and the dating process was undertaken at BETA Analysis Inc., USA, using the accelerator mass spectrometry (AMS) method (Table 6.1).

6.6.1. Trench 1

Trench 1 was excavated across the fault scarp developed on the basement rock in August, 2018 when the vegetation flourished (see Fig. 6.3c for location). The sedimentary units exposed in this trench are relatively simple with the composition of basement rock and overlain dark soil. (Fig. 6.6c–f). Three faults are identified in the exposure walls in this trench. In the west wall, the basement rock was pushed up into the dark soil layer along fault F1 and its branch, leading to the falling and filling of dark soil material into the footwall (Fig. 6.6c). The fault F2 cuts through the basement rock into the surface soil, forming a sharp contact between the basement rock and dark soil, and leading to the thickened accumulation of soil material on the north side of fault F2. At the bottom of fault F2, a foliation structure parallel to the fault planes of F2 and F3 was observed in the cataclastic basement (Fig. 6.6c). Similar deformational characteristics could be observed on the east wall (Fig. 6.6d). One organic soil sample was collected at the bottom of the thickened dark soil, yielding a 14C calibrated age of 664–552 yr Cal BP (sample C12, Table 6.1).

6.6.2. Trench 2

Trench 2 was excavated across the fault scarp facing-upstream, perpendicular to the general striking of the main fault trace with a length of ~12 m and a width of 10 m in November, 2018 (Fig. 6.7a, see Fig. 6.3c for location). The ~1 m vertical drop at the north side of fault scarp could be observed (Fig. 6.6a–b). The deposits exposed in this trench mainly consist of unconsolidated alluvial sand-gravel and surface silt-soil that could be divided into 17 sedimentary units based on the differences in color, material composition, layering structures and radiocarbon dating ages (Fig. 6.7b). Unit 1 is composed of the surface soil on which the vegetation grew densely. Units 2–3 consist of light or dark gray soil that contain rich organic materials, yielding the calibrated radiocarbon ages in the range of 760–461 yr Cal BP (samples C14–17, Table 6.1). Units 4–5 are composed of brownish gray to yellowish gray sandy soil and poorly-sorted gravels. Two radiocarbon samples were collected in unit 5 after clearing away the superficial materials, and yielded the ages of 3345–2693 yr Cal BP (samples C18–19, Table 6.1). Units 6–7 consist of yellowish or brownish grey soil-sand-gravel without bedding structure. Unit 8 consists of gray sandy soil with gravels varying from few to tens of centimeters in diameter, yielding a ^{14}C age of 6032–5934 yr Cal BP (sample C22, Table 6.1). Unit 9 composed of alluvial soil-sand-gravel was covered by unit 8, and was dated to be 10420–10229 yr Cal BP (sample C20, Table 6.1). Units 10–11 are composed of light-grey soil-gravel sediments without bedding structure. Unit 12 consists of yellowish grey sand-gravel at the bottom of trench wall. Most of these gravels have a poor roundness and large diameter. A sample collected at this unit yielded a ^{14}C age of 9600–9483 yr Cal BP (sample C21, Table 6.1). Units 13–16 consist of mud-gravel, sand-gravel and soil-sand with varying colors. Unit 17 is composed of the cataclastic

basement rock with foliation structure, similar with that exposed in trench 1.

According to the stratigraphic and structural features, six faults are identified in this trench. The sedimentary layers of units 7, 9–12 and 16 are offset by fault F1 and overlain by unit 6. The units 2–5 and 9–12 are cut by F2 and F3 faults with distinct vertical offset, leading to the formation of graben structure bounded by F2 and F3. The northern boundary fault F2 was defined by different sediment compositions with coarse-grained sand-gravel in unit 4 in the north and thick dark grey soil in unit 2 in the south (Fig. 6.8a). The southern boundary fault F3 was identified by the sharp change in sediment color, contrasting by the northern reddish brown sand-gravel of unit 5 and the southern yellowish grey sediments of unit 8 (Fig. 6.8b), which might be traced downward into the bottom of the trench where the basement rock from the alluvial fan deposits are bounded (Fig. 6.8d). The cataclastic basement rock with foliation structure similar with that exposed in trench 1 was observed at the bottom of this trench in unit 17 (Fig. 6.8d). The sedimentary layers of units 8–12 are offset by fault F4, which extends into the cataclastic basement rocks. Units 9–14 are cut by fault F5, and overlain by the sedimentary layer of unit 8. Units11–15 were cut by fault F6 and covered by unit 10. All these faults have a nearly upright fault planes.

6.7. Identification of Paleoseismic events

Large paleo- and historical- earthquakes that ruptured the ground surface generally leave evidence of coseismic deformation preserved in sedimentary layers. Based on the structural features including fault structures, deformation and offset of the sedimentary layers with radiocarbon dating results, four paleoearthquakes (E1–E4) are identified from the trench results on the WQLF as illustrated by the schematic diagram of Fig. 6.9.

The details are discussed below.

6.7.1. Event 1

In trench 1, the fault F1 and F2 on both walls cut through the yellowish-brown basement marble into the ground surface, leading to the distinctly thickened accumulation of dark grey soil due to the disturbance of fault slipping (Fig. 6.6c–f). The deformation characteristic and the dating result of sample C12 collected at the bottom of thickened dark soil indicate a fault slipping event occurred after 664–552 yr Cal BP on the WQLF.

In trench 2, the graben structure bounded by F2 and F3 faults was verified by the distinctly thickened accumulation of dark grey soil of unit 2 and vertical offset of unit 5 and units 9–12 (Fig. 6.7). The injection veins infilled by the dark to grey organic soil in the graben structure were observed (Fig. 6.8c). Radiocarbon dating samples collected from the injection veins in unit 3 (samples C15–C17, 760–471 yr Cal BP) have a comparable age with the overlying soil layer of unit 2 (sample C14, 664–552 yr Cal BP), indicating that the injection materials in unit 3 are likely to be sourced from the overlain sediments of unit 2 (Figs. 6.7b and 6.8c). These dating results manifest that the injection veins formed after the age of 471 yr Cal BP (sample C16) during the process of coseismic surface deformation.

6.7.2. Event 2

In trench 2, the sedimentary layers of unit 5 and units 9–12 were cut by F2 and F3 faults, forming a graben structure bounded by these two faults (Fig. 6.7b). The uniform offset of unit 5 and units 9–12 in vertical direction indicates that the deformation was caused by a single faulting event (Fig. 6.7b). The ^{14}C dating samples from unit 5 gave

ages in this range of 3345–2693 yr Cal BP (sample C18 and C19, Table 6.1). The graben structure bounded F2 and F3 faults was infilled by the thickened alluvial fan deposits and dark grey soil layer. The sample collected from the bottom of unit 3 yielded the age of 760–672 yr Cal BP (sample C17, Table 6.1). Therefore, the faulting event occurred after the deposition of unit 5, prior to the deposition of unit 3 in the period of 2693–760 yr Cal BP. The slipping event is distinguished from Event 1 by the distinctly different vertical offset between units 2-3 and units 5, 9–12 (Fig. 6.7b).

6.7.3. Event 3

As shown in trench 2, the F1 and F5 faults cut the sedimentary layers of unit 7, units 9–14 and unit 16, and were overlain by unit 6 and unit 8, respectively (Fig. 6.7b). Unit 6 and 8 have a similar sedimentary composition and structure characterized by the yellowish gray sand-gravel with the poorly-sorted angular pebbles varying from a few millimeters to 30 cm in diameter, suggesting that these two units probably have a similar sedimentary ages. Units 9–11 were offset by F5 fault with a continuous vertical displacement of ~2 m, which was probably produced by one or two fault slipping events given the 1-m-long vertical offset produced by Event 2 as stated above. The F5 fault terminated at the top of unit 9 dated to be 10420–10229 yr Cal BP (sample C20, Table 6.1) and was covered by unit 8 with the age of 6032–5934 yr Cal BP (sample C22, Table 6.1). Thus, the timing of the third faulting event is constrained in the period of10229–6032 yr Cal BP.

6.7.4. Another inferred event (Event 4)

There is a wide time-span of ~4000 years between unit 9 with the age of 10420–

10229 yr Cal BP (sample C20, Table 6.1) and unit 8 with the age of 6032–5934 yr Cal BP (sample C22, Table 6.1). The sedimentary layers of unit 11 and units 13–15 were cut by F6 fault but overlain by unit 10, indicating that the slipping event occurred after the formation of unit 11 but before the deposition of unit 10. Due to the lack of reliable dating results of unit 10 and 11, more work is required to confirm this event.

6.8. Discussion

6.8.1. Timing and Recurrence interval of large earthquakes on the WQLF

Large earthquakes generally repeatedly occur on mature active faults (Liu et al., 2007). Coseismic surface deformation generated by fault slipping events and the corresponding dating constraints of each paleo- and historical earthquake make it possible to build a precise timing of the paleoseismic events, especially for large historical earthquakes with a short elapsed time. The investigations focusing on the coseismic surface rupture and the associated faulting-derived topography generally can provide direct evidence for identifying these large historical earthquakes (Pantosti et al., 1996; Shao et al., 2017). Such samples have been widely reported by previous studies worldwide.

Similarly, the analyses of outcrop observations and trench excavations as presented in this chapter, together with the results of radiocarbon dating, provide new evidence for Holocene faulting events occurred on the WQLF. In order to determine the timing of paleoseismic events, radiocarbon samples were collected from alluvial fan deposits composed of soil, silt and gravels in trench 2. It was snowing heavily when the radiocarbon samples were taken in trench 2 in last November, thus there is an uncertainty about the completely exact sampling locations, but the basic sites could be

guaranteed. These samples were processed by the Beta Radiocarbon Laboratory and the results were calibrated using Oxcal 4.2 (Ramsey, 2009). Strictly speaking, these dating results should be older than the true ages of sediments where they firstly deposited due to fluvial transport. Therefore, these ages should be regarded as the lower bounds for the associated deposits. Actually, the transport time of alluvial fan deposits from original locations to the present sites driven by water flow is considered to be very short when compared with the deposition ages of alluvial fan deposits, especially for regions where a steep topographic relief are developed as presented around trench 2. The transported deposits were rapidly covered by subsequent sediments again, which guarantees the relative stability and freshness of alluvial fan deposits. Although this problem has been realized by most researchers, no feasible ways can be used to solve the difficulty due to the unchangeable nature. Considering the relatively short transport time, the dating results of alluvial fan deposits are commonly accepted as the in-situ deposition time to some extent (McCalpin, 2009; TRoux-Mallouf et al., 2016; Galli et al., 2018; Sancar et al., 2019).

In trench 1, the deformation features of dark soil associated with faulting and the dating result of sample C12 indicate that the most recent surface-rupturing event on the WQLF occurred after 664–552 yr Cal BP (Fig. 6.6c and e). The coseismic deformation characterized by the injection veins in trench 2 yielded the age results of 760–471 yr Cal BP (samples C15–C17, Table 6.1), strongly manifesting that the most recent surface-rupturing earthquake occurred after 760–471 yr Cal BP. The results obtained in these two trenches consistently suggest that a large earthquake (E1) capable of producing surface rupture occurred on the WQLF after 760–471 yr Cal BP.

Prior to the most recent event, the penultimate faulting event (E2) that offset the

sedimentary layers of unit 5 and units 9–12 can be placed in the period of 2693–760 yr Cal BP from the samples C19 and C17 (Fig. 6.7b), after the deposition of unit 5 but before the deposition of units 2–3 (stages 7–9 in Fig. 6.9). The formation of the graben structure exposed in trench 2 may be relevant with the two faulting events (E1 and E2) that accumulated the vertical offset.

Before E2, the timing of the third earthquake event (E3) revealed by trench 2 is constrained in the period of 10229–6032 yr Cal BP between sample C22 and C20, after the deposition of unit 9 but prior to the deposition of unit 8 (stages 5–7 in Fig. 6.9). This event is discerned by the vertical displacement of units 9–11 with an offset mount of ~2 m. Integrating the result of outcrop observations (Fig. 6.4), this event could be further constrained in this range of 9005–8596 yr Cal BP.

The oldest determined earthquake event (E4) revealed by trench 2 is loosely constrained in the time after the deposition of unit 11 but before the deposition of unit 10 (stages 1–4 in Fig. 6.9). Due to the lacking of reliable dating results, this event needs to be further confirmed by the future work. Given the wide time-span of ~4000 years (10229–6032 yr Cal BP) for E3, there is a big possibility that the true E4 occurred in this range of 9005–8596 yr Cal BP, and thus the E3 occurred between 8596 and 6032. The estimation might be more reasonable when taking the recurrence principle of characteristic faults into consideration. For the characteristic faults, the recurrence interval of large earthquakes is generally relatively stable. The time interval between E2 and E1 is about 2200–2300 years. Therefore, the E3 possibly occur in the early stage of 10229–6032 yr Cal BP, and the E4 occurred in this range of 9005–8596 yr Cal BP. In this case, it means at least four large earthquakes occurred in the past ~9000 years, suggesting an average recurrence interval of ~2250 years. The root for causing that is

the old dating result of 10420–10229 yr Cal BP of unit 9 (sample C20, Table 6.1), which is older than the underlying sedimentary layer of unit 12 (sample C21, Table 6.1). The duplicate of sample C20 will be re-examined and dated again by the future work.

The reconstruction of these four paleoseismic events was achieved by reversing from the current state to the last stage step by step (Fig. 6.9). Due to the complex influence of deposition, erosion, pre-existing topography such as slope even the possible flood deposits, it is indeed difficult to reproduce the true situations of each stage. In addition, the WQLF was mainly dominated by strike-slip motion with little vertical component as documented in Chapter 5, which increases the difficulty to restore each stage based solely on the vertical offset of sedimentary units. Some uncertainties were inferred during the reconstruction process of paleoseismic events (Fig. 6.9).

The paleoseismic study revealed by the outcrop and trench results identified at least three or four large paleoearthquakes in the past ~9000 years on the WQLF, suggesting an average recurrence interval of large earthquakes of 2250–3000 years. The result is consistent with the previous report of 2200 years' recurrence interval based on the analyses of deposition rhythm (Li, 2005).

The detailed field investigations and topographic analyses as documented in Chapter 5 support the viewpoint that the alluvial fans and terraces have been systematically left-laterally deflected or offset by ~7 m to tens of meters during the late Pleistocene–Holocene on the WQLF in the northeastern marginal zone of the Tibetan Plateau. The offset of ~7 m recorded by the terrace with the age of 2350–2310 yr Cal BP (sample C05, Table 5.2) probably represent the characteristic left-lateral displacement produced by individual earthquake (Figs. 5.8). The characteristic offset and the corresponding age corroborate with the cumulative offset of ~35 m in the alluvial terrace which was dated

to be 13480–13365 yr Cal BP (sample C07, Table 5.2), suggesting at least five or six paleoearthquakes occurred on the WQLF in the past ~13000 years with an average recurrence interval of 2200–2600 years. The result is consistent with that estimated from the analyses of outcrop observations and trench excavations with the average recurrence interval of 2250–3000 years.

6.8.2. Seismic activities on LLF and WQLF

The fact that the large intracontinental recurring earthquakes generally occur on the pre-existing mature active faults has been widely accepted by most geologists and seismologists (Liu et al., 2007). That is, the faults which have repeatedly triggered large earthquakes generally have a long-term seismic activities and thus probably record large cumulative displacement, such as the San Andreas Fault (Brune et al., 1969; Scholz, 2000; Jolivet et al., 2015), Kunlun Fault (Lin et al., 2002), and Longmenshan thrust belt (Hubbard and Shaw, 2009; Xu et al., 2009).

Han et al (2001) ever reported the late Pleistocene activity of LLF based on the field investigations. Fault scarps, deflected stream channels, earthquake- induced landslides and liquefactions were observed along LLF. The lowest fluvial terrace developed in this area which contains the red ceramic fragments with the characteristic age of 3–5 ka was offset by LLF (Yang et al., 2015). However, no large historical earthquakes even minor earthquakes ever occurred on this fault according to the historic records, apart from the 1654 M 8.0 Tianshui earthquake (EDPDCEA, 1995). The result contradicts with the knowledge that the seismogenic fault generally repeatedly triggered earthquakes.

All large historic earthquakes with magnitude $\geq$ 6.0 occurred in this area were checked according to the document catalogue (EDPDCEA, 1995). Two large historic earthquakes with magnitude of M 7.0 occurred on the WQLF in AD 143 and AD 743,

demonstrating that large earthquakes have repeatedly occurred on the WQLF. As documented in Chapter 5, the drainage systems, mountain ridges, alluvial fans, and terraces have been systematically deflected or offset by ~7 m up to hundreds of meters during the late Pleistocene–Holocene, as well as the maximum cumulative offset of 18 km recorded by the Yellow River drainage systems, indicating the long-term fault slipping on the WQLF. Until today, there is no geological and geophysical evidence showing the creep movement occurred on WQLF and other main active faults developed in the Tibetan Plateau. Therefore, the total horizontal displacement of 18 km on the WQLF is suggested to be the maximum cumulative displacement produced by the repeated fault slipping since the late Cenozoic as with these three or four paleoearthquakes occurred in the past ~9000 years on the WQLF.

According to the above analyses, the event E1 occurred after 760–471 yr Cal BP. After checking all the historic earthquakes occurred in the study area, only the 1654 M 8.0 Tianshui earthquake possibly corresponds to the event E1. Given the incompleteness of historic records, however, it is also likely that a large earthquake unrecorded in the historical document occurred near the site of trench 2 on the WQLF after 760–471 yr Cal BP. In Japan, the earthquake magnitude which can produce the surface rupture is generally larger than M 6.5. Therefore, in this case, an earthquake with magnitude larger than 6.5 was considered to occur near trench 2.

Therefore, if the historic earthquake records since Ming dynasty are complete and no other large earthquakes are missing, the event E1 can correspond to the 1654 M 8.0 Tianshui earthquake based on the above analyses.

6.9. Conclusions

Based on the analyses of tectonic geomorphology, trench excavations, ^{14}C dating results, together with the re-examination of historical documents, the following conclusions concerning with the paleo- and historic earthquakes occurred on WQLF can be drawn.

1) The most recent surface-rupturing earthquake (E1) occurred after 760–471 yr Cal BP. If the historic earthquake records are complete and no other large earthquakes capable of producing surface rupture are missing, E1 can only corresponds to the 1654 M 8.0 Tianshui earthquake, which means that the 1654 M 8.0 Tianshui earthquake was caused by WQLF but not LLF as previously reported.

2) The penultimate large earthquake (E2) occurred in the period of 2693–760 yr Cal BP.

3) The third recent large earthquake (E3) occurred in the period of 10229–6032 yr Cal BP, more probably in the range of 9005–8596 yr Cal BP.

4) There is a possibility that the fourth earthquake event (E4) occurred in the period of 9005–8595 yr Cal BP, and E3 occurred in the range of 8596–6032 yr Cal BP. Therefore, at least three or four large earthquakes have repeatedly occurred on the WQLF in the past ~9000 years, suggesting an average recurrence interval of 2250–3000 years.

Table 6.1. Radiocarbon dating results.

Sample Code	Beta ID[a]	Conventional Age[b] (yr BP)	Calibrated Age[c] (Cal BP)	Calibrated Calendar Age[c] (BC/AD)	Description
C09	473998	7770 ± 30	8595-8460	BC6645–BC6510	Organic soil
C10	473997	8690 ± 30	9700-9550	BC7750–BC7600	Organic soil
C11	473996	8120 ± 30	9125-9005	BC7175–BC7055	Organic soil
C12	504693	630 ± 30	664-552	AD1286–AD1398	Organic soil
C13	514573	140 ± 30	281-270	AD1669–AD1780	Organic soil
C14	514574	630 ± 30	664-552	AD1286–AD1398	Organic soil
C15	514575	550 ± 30	564-516	AD1386–AD1434	Organic soil
C16	514576	450 ± 30	536-471	AD1414–AD1479	Organic soil
C17	514577	790 ± 30	760-672	AD1190–AD1278	Organic soil
C18	514578	3030± 30	3345-3144	BC1396–BC1195	Organic soil
C19	514579	2550 ± 30	2750-2693	BC801–BC744	Organic soil
C20	514580	9150± 30	10420-10229	BC8471–BC8280	Organic soil
C21	514581	8570 ± 40	9600-9483	BC7651–BC7534	Organic soil
C22	514587	5260± 30	6032-5934	BC4083–BC3985	Organic soil

[a]Samples were analyzed at Beta Analytic Inc., USA.

[b]Radiocarbon ages were measured using AMS and are referenced to the year A.D. 1950. The analytical uncertainties are reported at 2σ.

[c]Dendrochronologically calibrated calendar age by Method A from CALIB Radiocarbon Calibration Version 7.0 (Stuiver and Reimer, 1993).

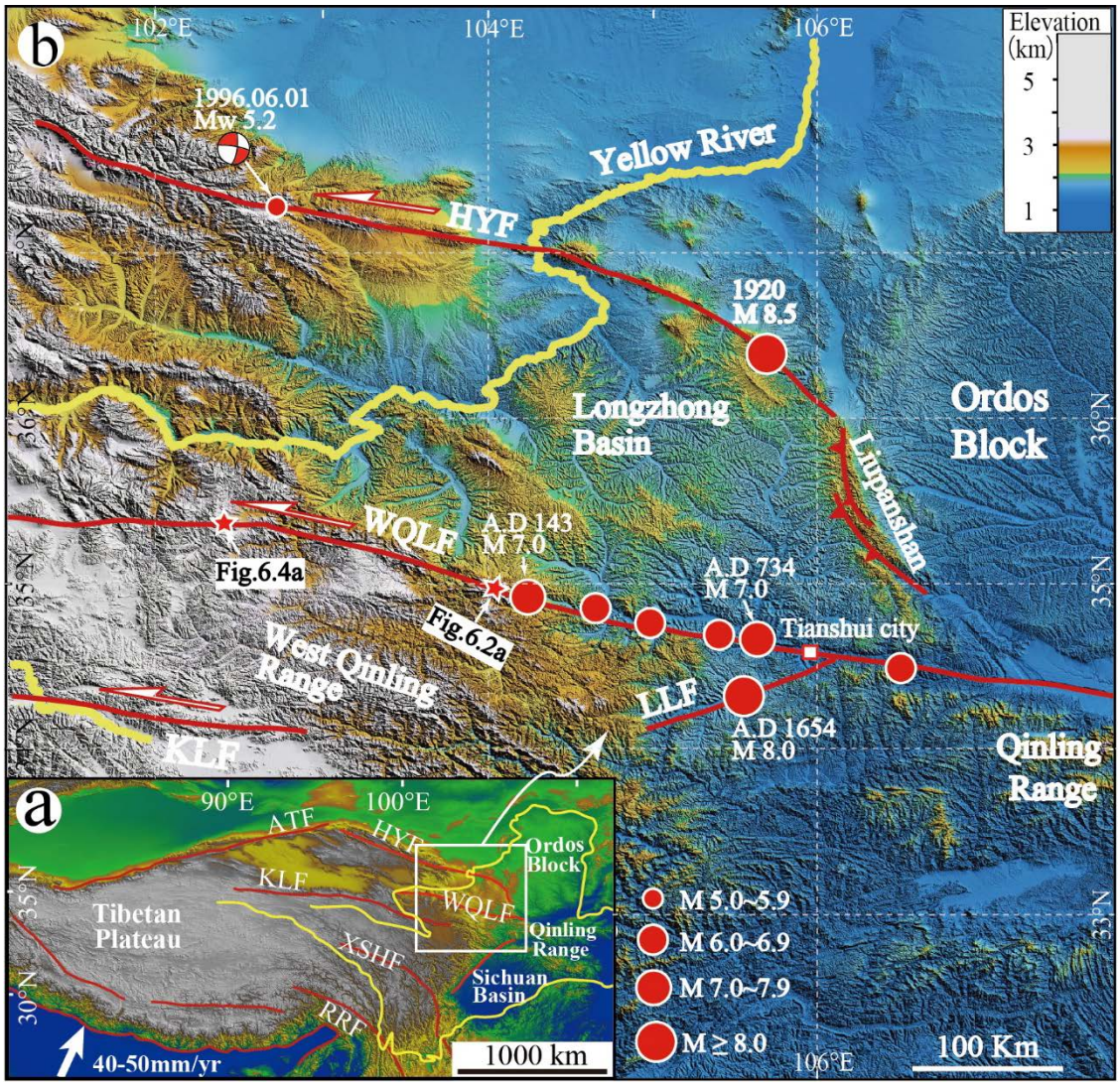

Fig. 6.1. Color-shaded relief map showing the topographic and tectonic setting of the study area. (a) Index map showing the location and the major active faults within and surrounding the Tibetan Plateau. The motion velocity of the Indian Plate is cited from Zhang et al (2004). (b) Color-shaded relief map showing the topographic features and tectonic setting of the study area. Historic earthquake information is from the Earthquake Disaster Prevention Department of China Earthquake Administration catalogue (EDPDCEA, 1995) and the focal mechanism is from the Global Harvard CMT catalogue (http://www.globalcmt.org). The acronyms used in the figure are defined as follows: ATF: Altyn Tagh Fault; KLF: Kunlun Fault; HYF: Haiyuan Fault;

WQLF: West Qinling Fault; XSHF: Xianshuihe Fault; RRF: Red River Fault.

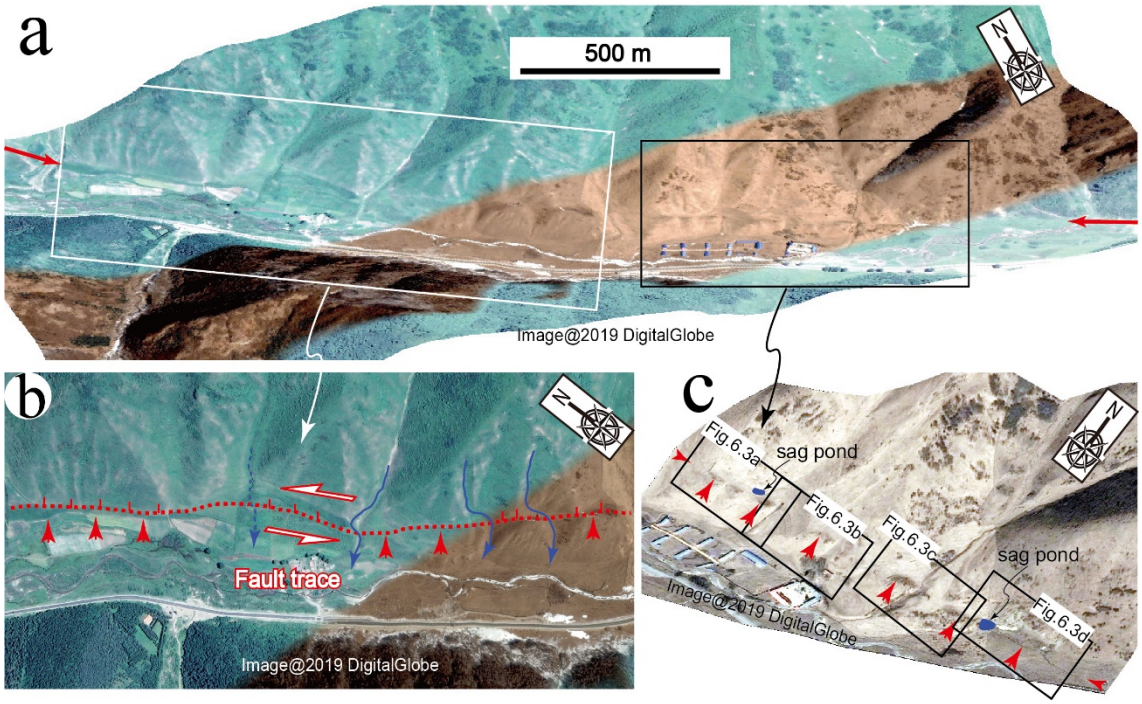

Fig. 6.2. 3D Google Earth images showing the tectonic landforms associated with active strike-slip faulting along the WQLF. (a) Overview of the tectonic landforms (see Fig. 6.1b for location). (b) The active fault trace indicated by the systematical offset of stream channels and fault scarps. The red dotted line indicates the trace of active fault, and short red arrows indicate the fault scarp and the dipping direction of fault scarp. (c) The related topography including fault scarps, saddles and sag ponds.

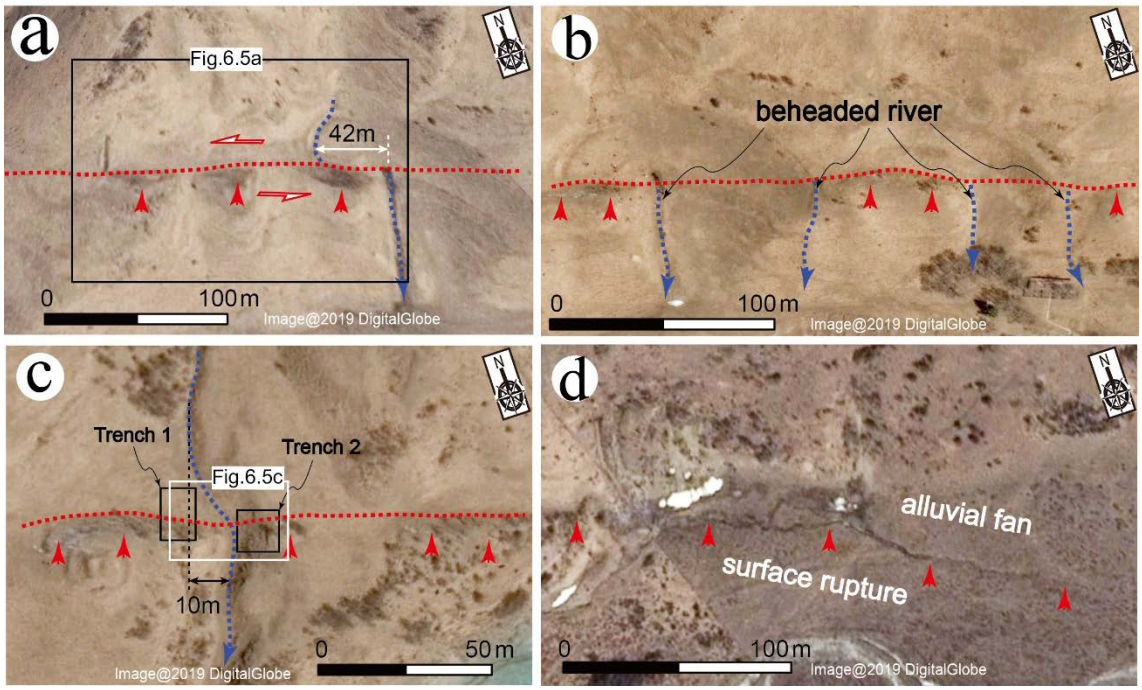

Fig. 6.3. Google Earth images showing the tectonic landforms associated with active strike-slip faulting along the WQLF (see Fig. 6.2c for locations). (a) Continuous fault scarps facing the uphill and the gully with an offset of ~42 m. (b) Beheaded rivers bounded by the active fault. (c) Fault scarps and trench locations with a gully deflected by ~10 m. (d) Surface rupture on an alluvial fan. The red dotted line indicates the trace of active fault and short red arrows indicate the fault scarp.

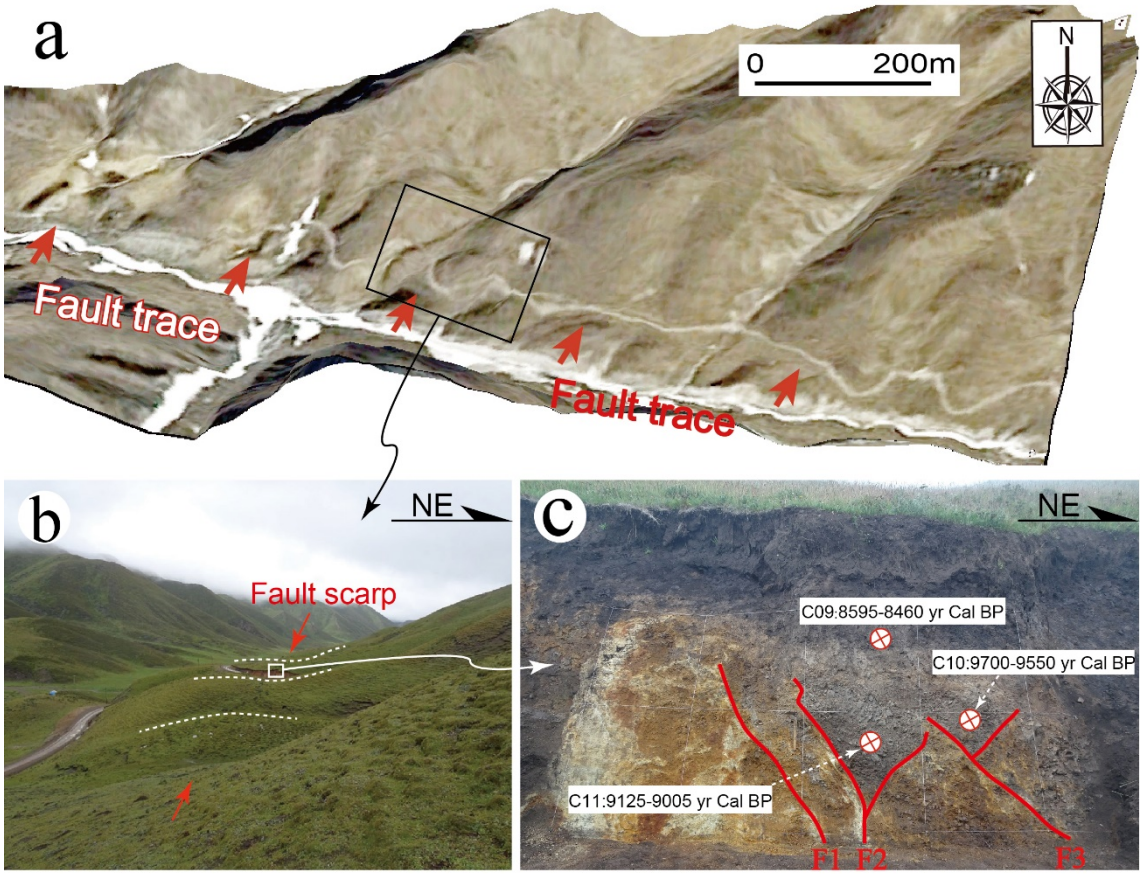

Fig. 6.4. 3D topographic image and field photographs showing the active fault trace and the field overview of tectonic landform and outcrop. (a) 3D view showing the active fault trace indicated by the fault scarps facing the uphill (see Fig. 6.1b for location). (b) Field photograph showing the fault scarps developed in a piedmont area. The white dashed line indicates the topographic surface slope. (c) Fault outcrop showing the formation of colluvial wedges bounded by the active faults (F1-F3), indicating a faulting event occurred in the period between 9125-8460 yr Cal BP from the samples of C11 and C09.

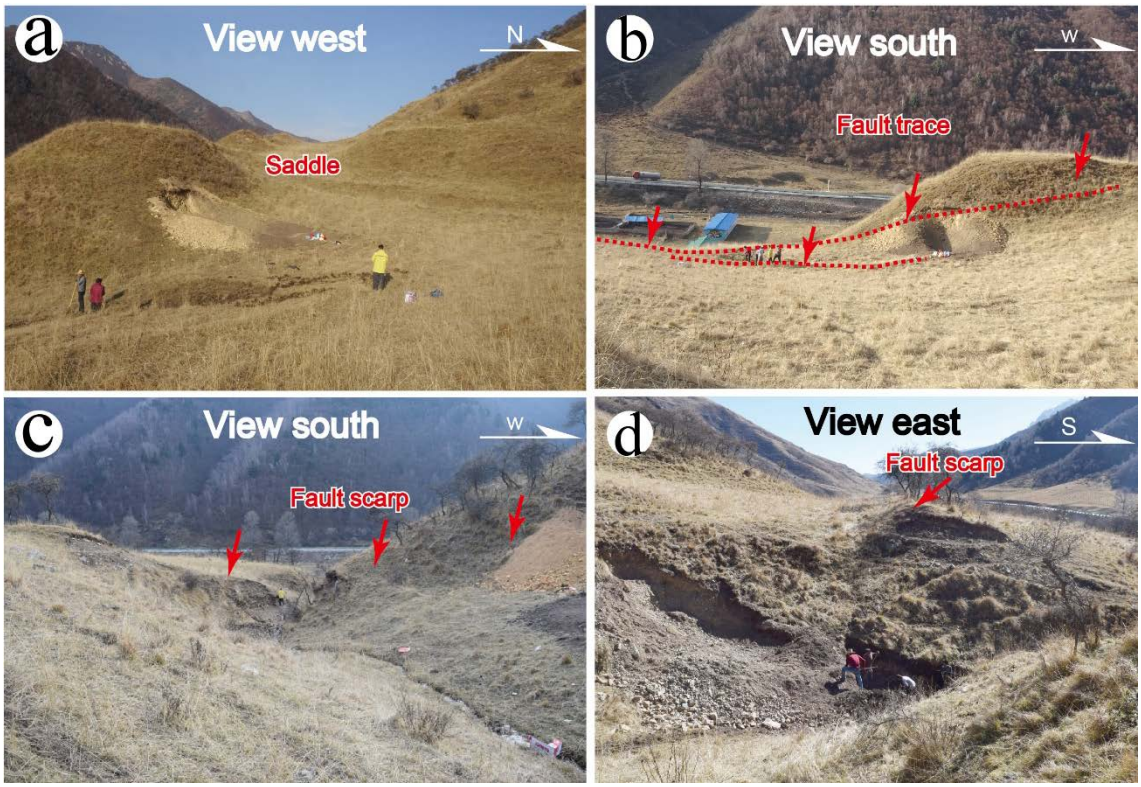

Fig. 6.5. Photographs showing the overview of tectonic landforms associated with the active strike-slip faulting. (a) Field photograph showing the faulted saddle geomorphology (see Fig. 6.3a for location). (b) Fault scarps facing the uphill. The red dashed line ndicates the active fault trace, the same location as (a). (c) Photographs showing the fault scarps facing the upstream of gully (see Fig. 6.3c for location). (d) Push-up structure occurred on the alluvial fan deposits, the same location as (c).

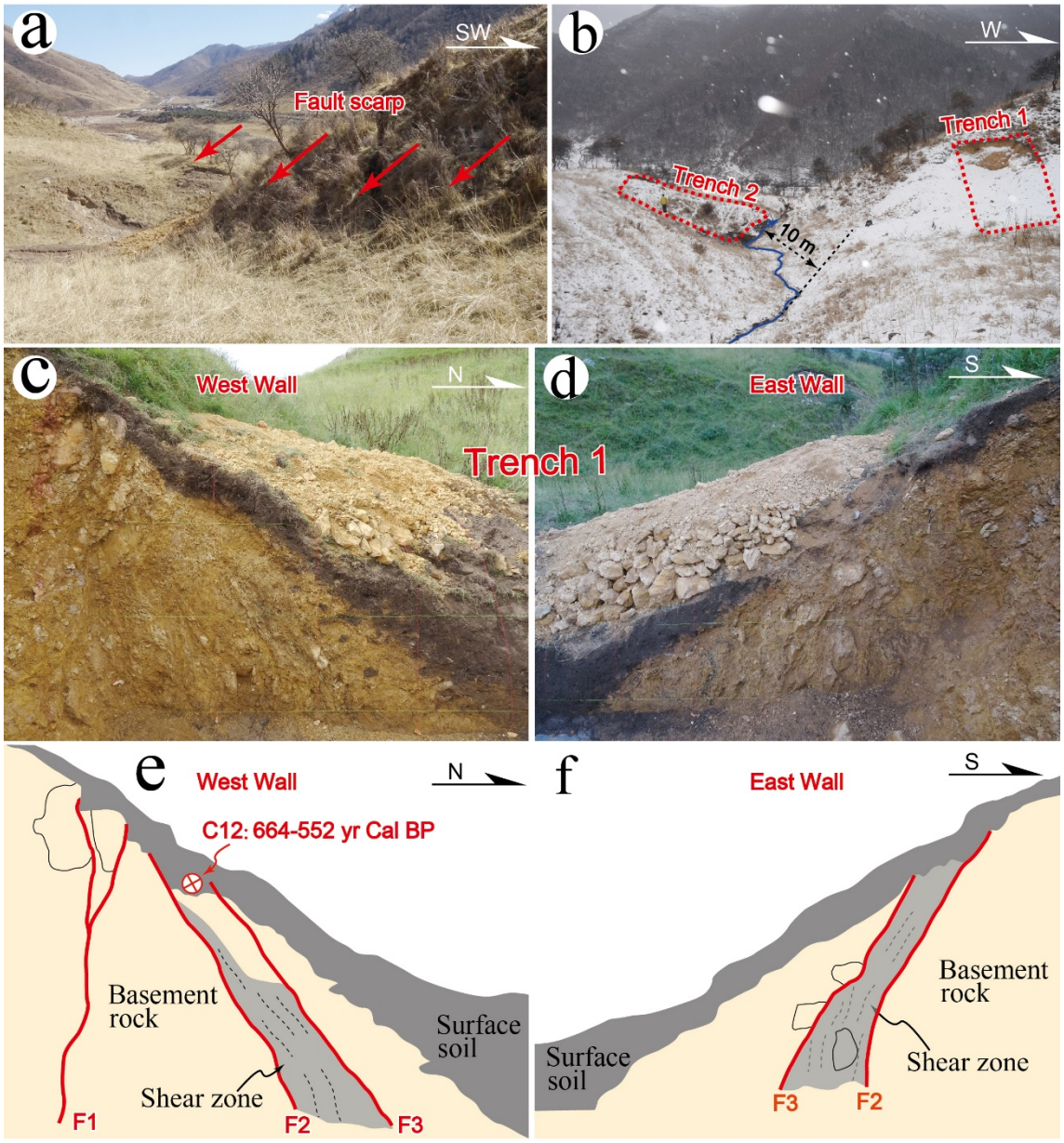

Fig. 6.6. Field photographs showing the topographic features and the outcrop walls in Trench 1. (a) Field photograph showing the overview of faulted geomorphology characterized by the fault scarps developed on both flanks of gully with the sinistral displacement of ~10 m, the same location as Fig. 6.5c. (b) The frontal view of trench locations (see Fig. 6.3c for trench locations), a ~10 m left-lateral offset of gully was observed between these two trenches. (c) West wall of Trench 1. (d) East wall of Trench 1. (e) Sketch of (c). (f) Sketch of (d).

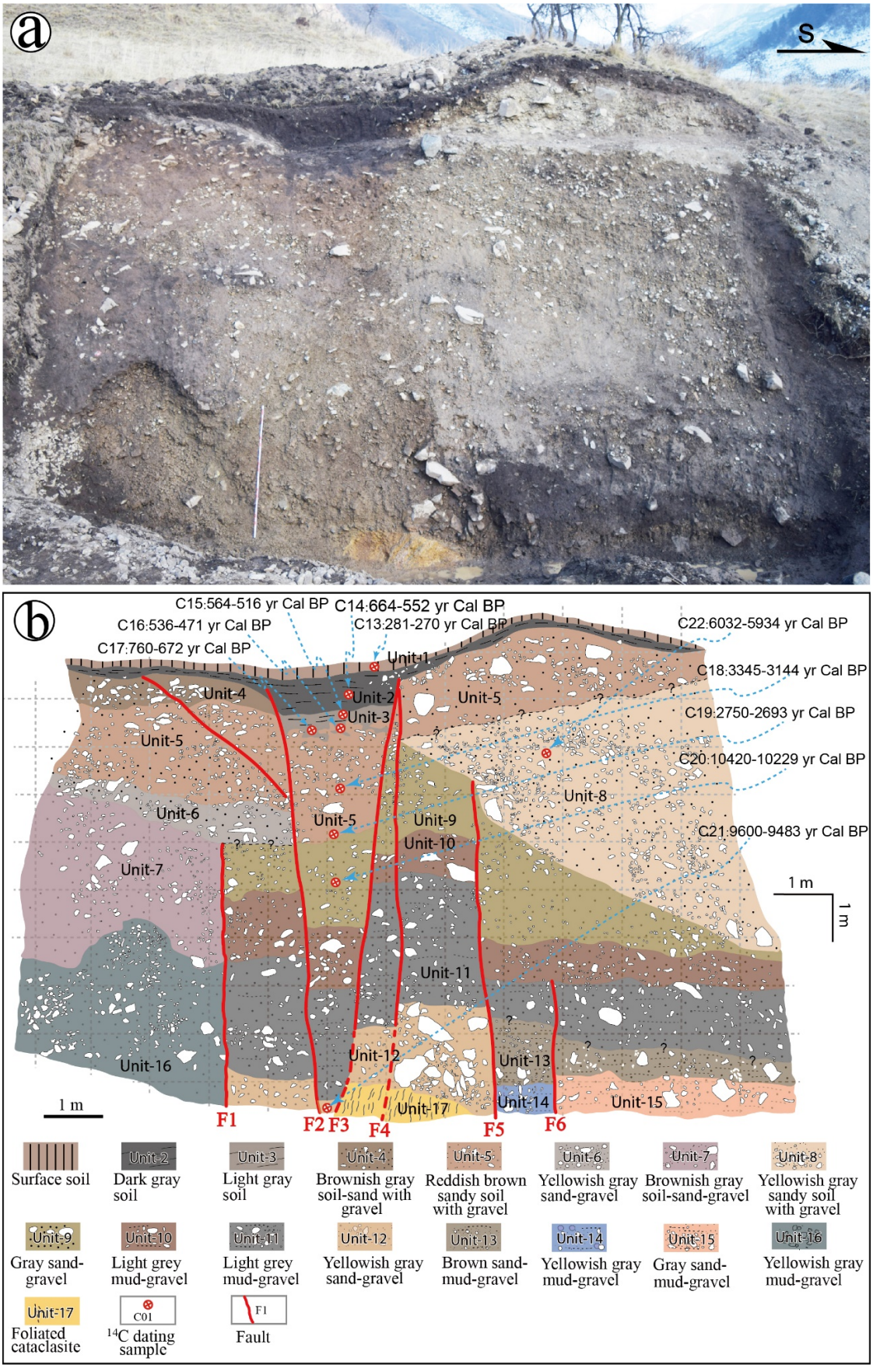
a
S
b
C15:564-516 yr Cal BP
C14:664-552 yr Cal BP
C16:536-471 yr Cal BP
C13:281-270 yr Cal BP
C17:760-672 yr Cal BP
C22:6032-5934 yr Cal BP
C18:3345-3144 yr Cal BP
C19:2750-2693 yr Cal BP
C20:10420-10229 yr Cal BP
C21:9600-9483 yr Cal BP
Unit-1
Unit-2
Unit-3
Unit-4
Unit-5
Unit-6
Unit-7
Unit-8
Unit-9
Unit-10
Unit-11
Unit-12
Unit-13
Unit-14
Unit-15
Unit-16
Unit-17
F1
F2
F3
F4
F5
F6
1 m
1 m
Surface soil
Dark gray soil
Light gray soil
Brownish gray soil-sand with gravel
Reddish brown sandy soil with gravel
Yellowish gray sand-gravel
Brownish gray soil-sand-gravel
Yellowish gray sandy soil with gravel
Gray sand-gravel
Light grey mud-gravel
Light grey mud-gravel
Yellowish gray sand-gravel
Brown sand-mud-gravel
Yellowish gray mud-gravel
Gray sand-mud-gravel
Yellowish gray mud-gravel
Foliated cataclasite
C01
14C dating sample
Fault

Fig. 6.7. Field photograph and sketch of Trench 2. (a) Photograph and (b) the corresponding sketch of Trench 2. The sampling locations may not be exactly accurate due to heavy snow, but the basic accuracy is guaranteed with uncertainty of about 10 cm in the vertical and 20 cm in the horizontal directions.

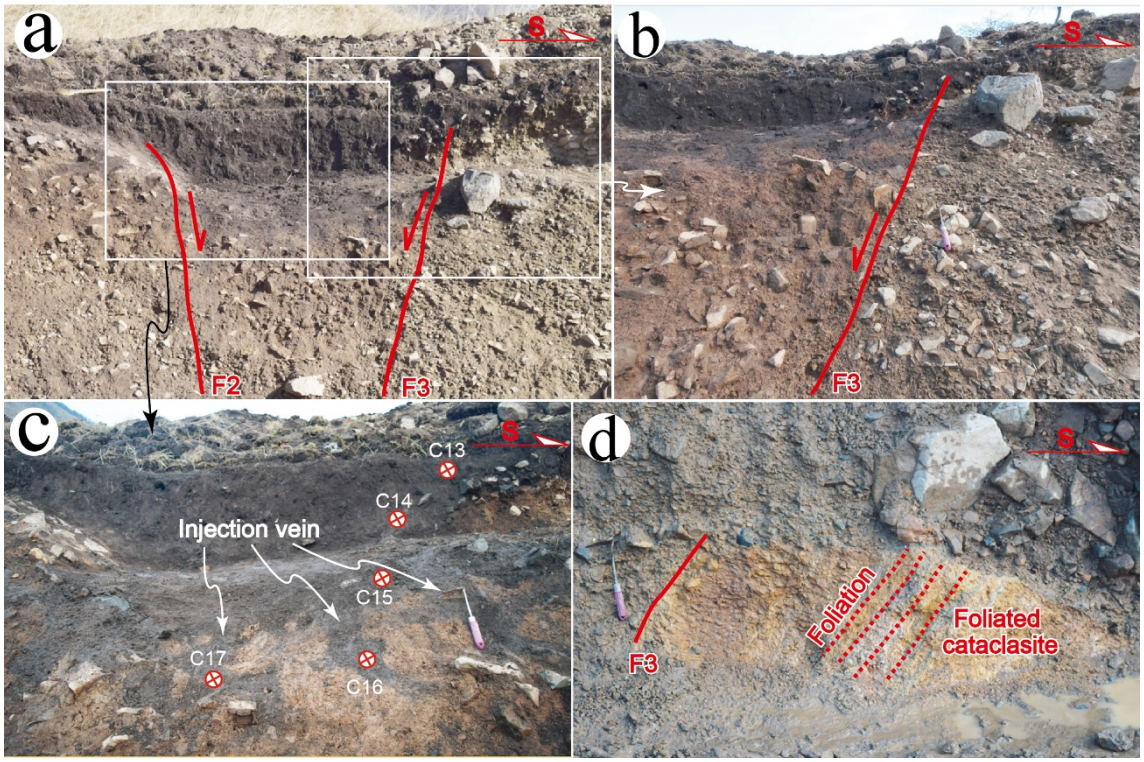

Fig. 6.8. Photographs showing the deformational characteristics of the sedimentary units in Trench 2. (a) Graben structure developed between fault F2 and fault F3, causing the thickened accumulation of dark-grey organic soil and related alluvial deposits. (b) The extremely different color difference between the both sides of fault F3. (c) Injection veins filled by the grey to dark soil and the associated sampling locations. (d) The fault F3 bounded the alluvial deposits and basement rock. Foliation structures developed in the cataclasitic rock. The red dashed line indicates the foliation structure.

① Initial state

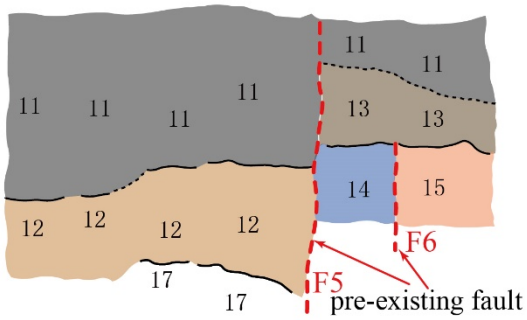

A pre-existing topographic solpe was inferred before unit 11 deposited

② Event E4

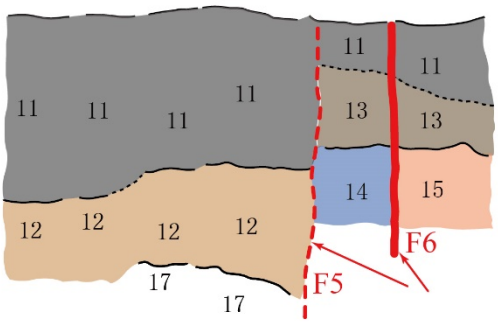

Slipping on fault F6

③ Deposition of unit 10

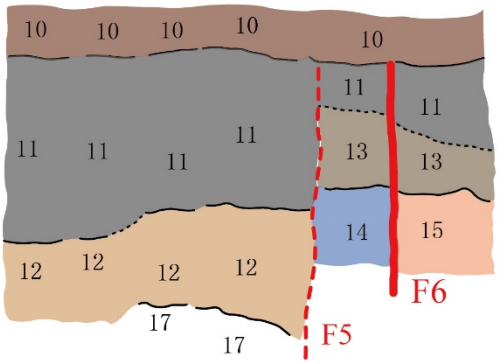

④ Erosion of unit 10 and deposition of unit 9

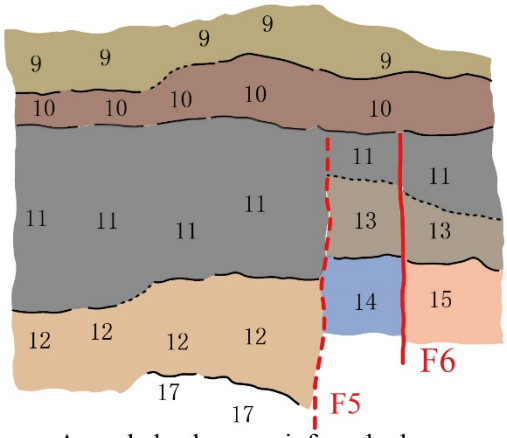

A eroded solpe was inferred when unit 9 deposited

⑤ Erosion of unit 9
and deposition of unit 6

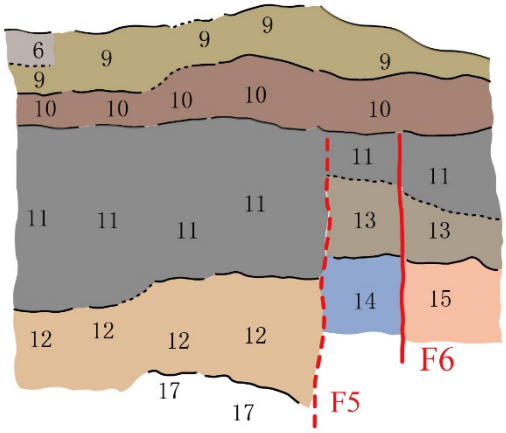

⑥ Event E3

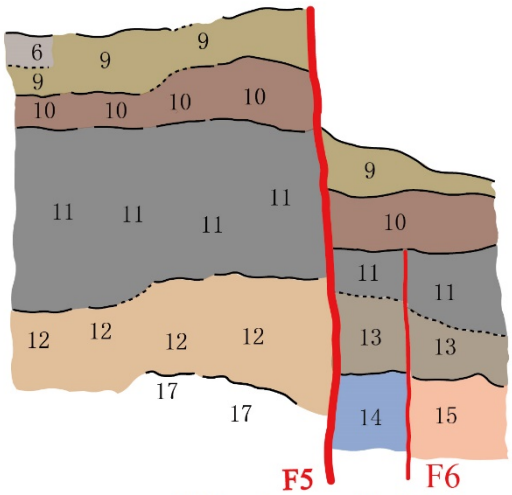

Slipping on fault F5

⑦ Deposition and erosion of Unit 8
then deposition of Unit 5

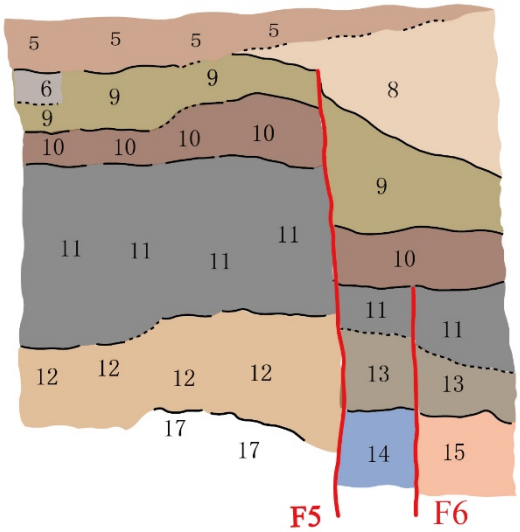

Slipping on fault F5 steepened the slope between unit 8 and unit 9

⑧ Event E2

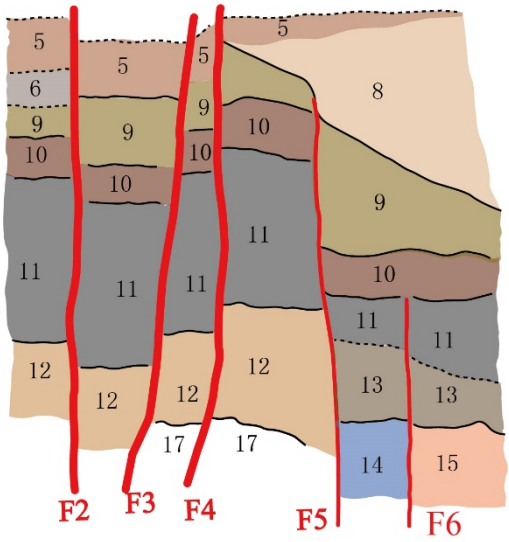

Slipping on faults F2-F4

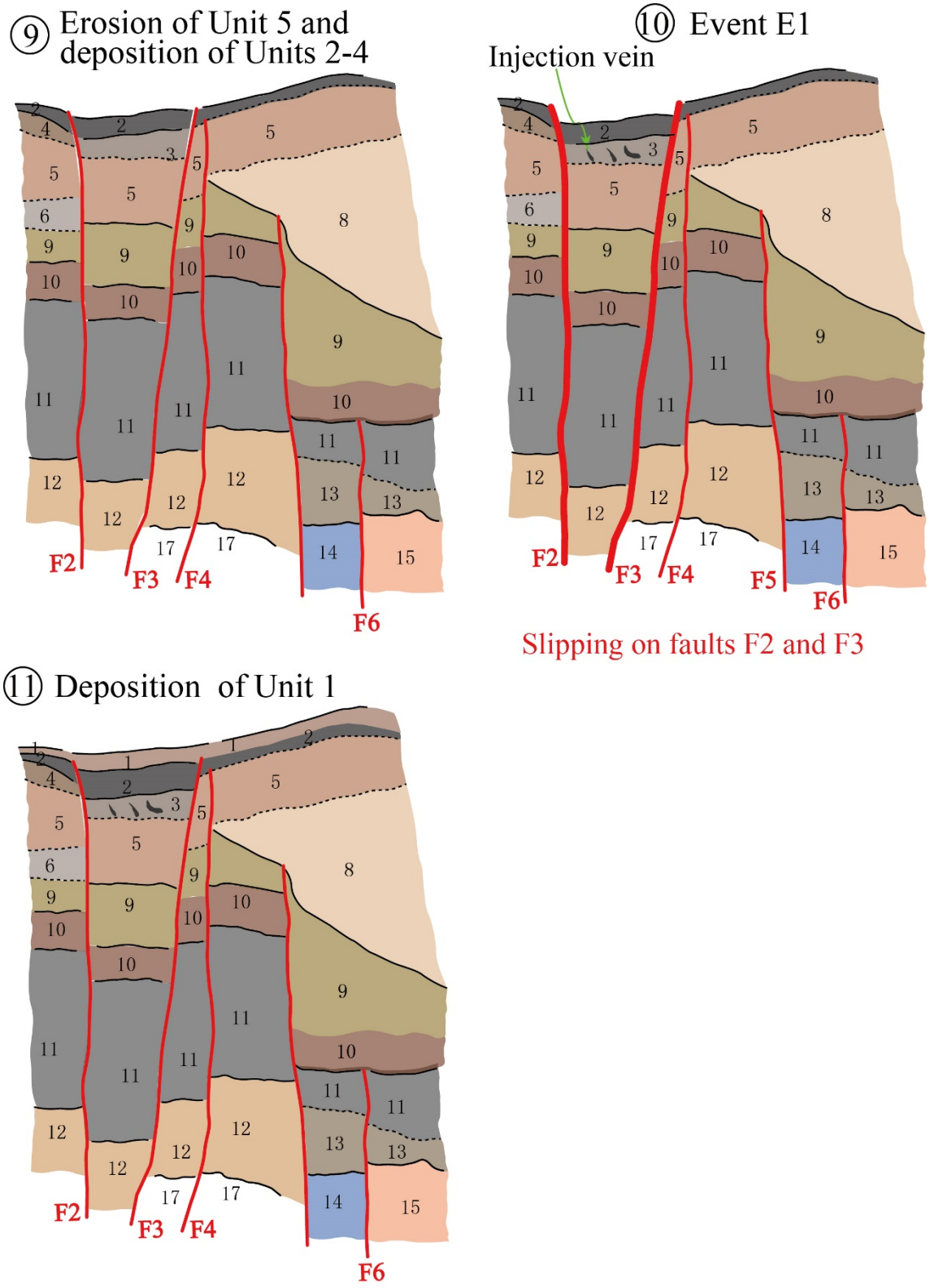

Fig. 6.9. Schematic diagram to explain the timing and processes of the paleoseismic events from E4 to E1. The thick fault line indicates the slipping fault when the

paleoearthquake occurred. The dashed line represents the inferred boundary of sedimentary unit or topographic surface. The Numbers ①-⑪ represent the evolution stages of paleoseismic events including the deposition, erosion and faulting.

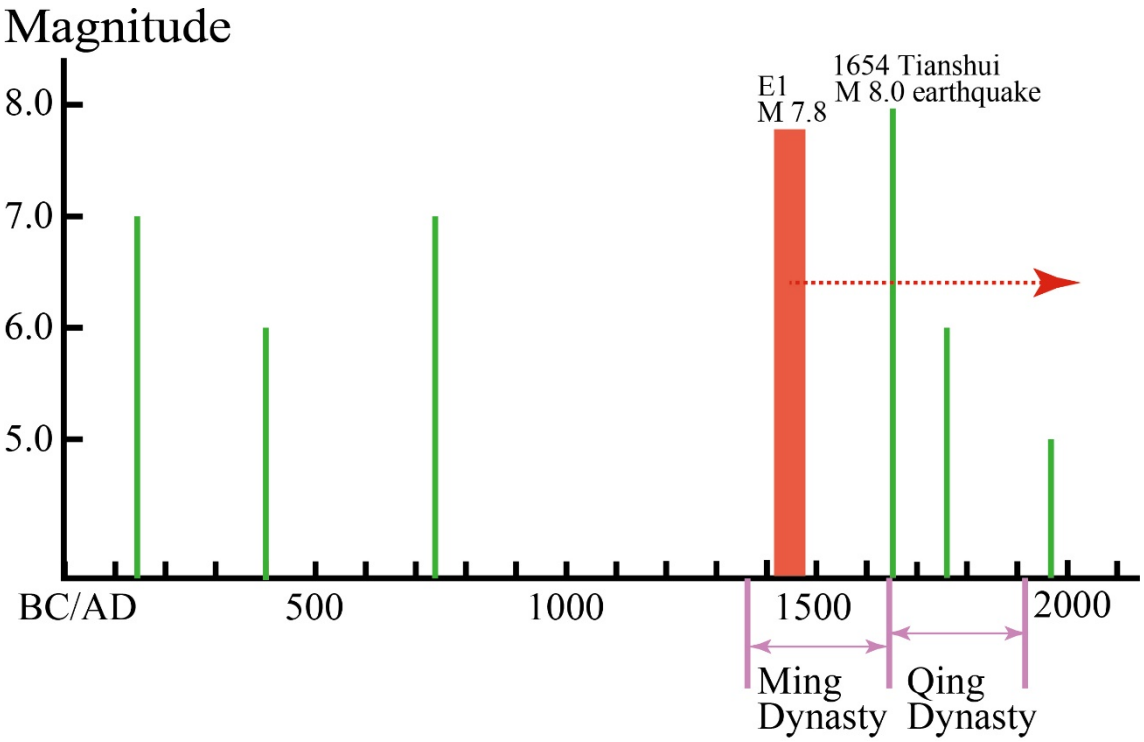

Fig. 6.10. The historic earthquakes occurred on WQLF (Earthquake Disaster Prevention Department of China Earthquake Administration catalogue (EDPDCEA, 1995). The red column indicates the paleoseismic event E1 occurred after AD1414–AD1479, the magnitude is inferred from the empirical relationship between the surface rupture length and the Magnitude (Wells and Coppersmith, 1994).

Chapter 7. Discussion

7.1. Active tectonic characteristics in the NE Tibetan Plateau

The northeastern Tibetan Plateau, as a frontal belt of the outward expansion of the Tibetan Plateau, is one of the most sensitive regions to respond to active tectonic processes associated with the collision and convergence between the Indian and Eurasian plates. In order to quantitatively describe and assess the active tectonic characteristics in the northeastern Tibetan Plateau, slip rates, maximum cumulative offset on major strike-slip faults, and deformational patterns are the most fundamental factors to constrain the geometry, kinematics and geodynamic mechanism of the northeastern Tibetan Plateau.

Two end-member models have been proposed to explain the plateau deformation and outward expansion of the Tibetan Plateau. The controversy between these two models focuses on the discrepancy whether the plateau strain energy has been mostly absorbed by the localized deformation along the first-order strike-slip faults as expressed by the eastward material extrusion in the Tibetan Plateau (e.g., Tapponnier et l., 1982). On the other hand, other researchers argued that the crustal shortening has absorbed by main strain accumulation as reflected by thrust and fold deformation in the northeastern Tibetan Plateau (England and Houseman, 1986). Therefore, the spatial complexity of active tectonic deformation in the northeastern Tibetan Plateau can be defined to this extent how the strain energy is partitioned between localized deformation on the major active strike-slip faults and continuously-distributed crustal deformation diffused in the lithosphere (Loveless and Meade, 2011). Specifically, the main debate has been focused on whether the regional-scale left-lateral strike-slip faults comprising the Altyn Tagh

Fault, Kunlun Fault, Haiyuan Fault and West Qinling Fault in the northern and northeastern Tibetan Plateau have acted as the rigid-block boundaries that absorbed the majority of strain energy (Tapponnier et al., 2001; Shen et al., 2005; Thatcher, 2007).

The slip rate and maximum cumulative offset on the major strike-slip faults can provide an important reference to assess the above debate. Recent publications have reported that the strike-slip rate on the left-lateral Kunlun Fault diminishes eastward from larger than 10 mm/yr at the western and central segment to smaller than 2 mm/yr at its eastern tip (Kirby et al., 2007; Lin and Guo, 2008), suggesting any extrusion of the Tibetan lithosphere accomplished by the slip along the Kunlun Fault must be absorbed by internal deformation of the plateau surrounding the fault tip (Kirby et al., 2007). Coincidentally, the Altyn Tagh Fault, the northern edge of the Tibetan Plateau, also displays a diminished slip rate toward the east from 9–14 mm/yr at the central segment to ~4 mm/yr at its eastern tip (Cowgill et al., 2009). The slip rate on the Kunlun Fault and Altyn Tagh Fault at their eastern segments with characteristically low values of ~3–4 mm/yr is at the same order with the Haiyuan Fault, the outmost active strike-slip fault of the northeastern Tibetan Plateau with the Holocene slip rate of ~4.5±1.0 mm/yr (Li et al., 2009). For some secondary strike-slip faults between the Kunlun Fault and Haiyuan Fault, trending NW- and NE-striking, a low slip rate of ~1 mm/yr were also reported (Zheng et al., 2016). The WQLF, the target fault in this study, sandwiched between the Kunlun Fault and the Haiyuan Fault, behaved as a left-lateral strike-slip fault with a late Pleistocene slip rate of 2.0–2.6 mm/yr since the late Pleistocene as documented in Chapter 5. The result well corroborates the relatively low slip rates of other three regional-scale strike-slip faults in the northern and northeastern Tibetan Plateau (the eastern tips of the Altyn Tagn Fault and the Kunlun Fault, and the Haiyuan Fault). Thus,

it seems that all the main strike-slip faults developed in this area share the common feature of characteristically low strike-slip rates.

In the recent two decades, the GPS data have been widely applied to constrain the velocity vector of block motion in the Tibetan Plateau. The approach provides an opportunity to compare the strike-slip rate inferred from the geological and topographic evidence with that estimated from GPS measurement, also help understand the crustal motion across major active faults in the northeastern Tibetan Plateau. The low strike-slip rates as documented above are supported by the result of GPS observations. The slip rate of Altyn Tagh Fault within the area of 89–100^{o} E was reported to be 4–16 mm/yr with a decrease from the western section to the east (Zhang et al., 2004., Gan et al., 2007), similar with the Kunlun Fault varying from 14 to 2 mm/yr in the area of 96–100^{o} E (Wang et al., 2001). Moreover, the GPS observation also show that the WQLF has a low left-lateral slip rate of 1–2 mm/yr (Zheng et al., 2016), in accordance with the geologic result reported in this study.

Geological evidence and GPS observations consistently indicate that the active strike-slip faults in the northeastern Tibetan Plateau have a characteristically low slip rate and terminate at their eastern tips. However, the result contradicts with the large-scale tectonic extrusion along the main strike-slip faults that demands a high slip rate as previously-reported (Tapponnier et al., 1982). The eastward extrusion of plateau material might be very limited and was confined at the eastern tip of these strike-slip faults.

In addition, controversy about the distance of the block extrusion along the major strike-slip faults within the Tibetan plateau has been another extensive research topic in the past two decades (e.g., Houseman and England, 1993; Tapponnier et al., 2001; Jade

et al., 2004; Loveless and Meade, 2011). Previous studies deemed that the displacement could reach up to hundreds to thousands of kilometers to the east (e.g., Tapponnier et al., 2001). However, the viewpoint has been challenged and questioned by more and more publications.

Fu and Awata (2007) suggested that the maximum cumulative offset on the Kunlun Fault recorded by the basement rocks is ca. 100 km in the past 10±2 Ma. However, Burchfiel et al (1989, 1991) reported that only 10.5–15.5 km offset had occurred on the Haiyuan Fault through matching the offset geological markers on both sides of this fault. Afterwards, the total displacement along the Haiyuan Fault was estimated to be ~60 km by summing the offsets of three classes of pull-apart basins forming in different periods (Ding et al., 2004). In the southeastern margin of the Tibetan Plateau, the active strike-slip Ganzi–Yushu–Xianshuihe Fault extends for ca. 800 km from the central plateau with the geometry of projecting northeastward (Fig. 3.1). The maximum accumulated displacement recorded by the Yangtze River and its three tributaries in the past 13–5 Ma was suggested to be ~60 km (Yan and Lin, 2015), consistent with the total offset accumulated on the Haiyuan Fault. Evidence for larger offset along the Altyn Tagh Fault, however, does appear to be more robust (Yue et al., 2003; Cowgill et al., 2003). The statistical result based on the analyses of systematically deflected stream channels reported the maximum offset of ca. 72 km on the Altyn Tagh Fault (Chen and Yan, 2019). The maximum cumulative offset of ~18 km recorded by the Yellow River drainage systems on the WQLF also supports the limited horizontal displacement in the northeastern Tibetan Plateau as presented in this study.

From the perspective of seismic activities, the limited extrusion also seems to be

more rational when taking the characteristic displacement generated by individual earthquake and recurrence interval of large earthquakes into consideration. As proposed above, the coseismic horizontal displacement produced by individual intraplate earthquake is generally smaller than 10 m (Lin et al., 2002). We can assume that if the distance of tectonic extrusion reaches up to thousands of kilometers as suggested by Tapponnier et al (1982), that is, there were at least one hundred thousand large earthquakes capable of producing surface rupture ever occurred on the major strike-slip faults in the past 13–5 Ma, suggesting the average recurrence interval of large earthquakes in this range of 50–130 years. The less than 100 years' recurrence interval is obviously contradictory with the historical records (EDPDCEA, 1995) and modern seismic observations, also contravening with the previous studies of millennial recurrence interval of large earthquakes on the eastern Kunlun Fault (Lin and Guo, 2008) and Haiyuan Fault (Zhang et al., 1988b), and the result obtained in this study of 2250–3000 years' recurrence interval on WQLF as documented in Chapter 6. In addition, besides the horizontal displacement on the major strike-slip faults, the northeastward tectonic shortening in the northeastern Tibetan Plateau was discerned and emphasized by many studies (Burchfiel et al., 1991; Zhang et al., 2004; Lease et al., 2012). A 6.2 mm/yr north-northeast–south-southwest tectonic shortening across the Kunlun Fault was suggested by the geodetic and GPS data (Gan et al., 2007), indicating a significant compressive deformation in the northeastern marginal zone of the Tibetan Plateau. Recent seismic reflection analyses and balanced cross-section restoration indicate that the crustal shortening is significant enough to generate the current elevation and crustal thickness of the eastern and northeastern Tibetan Plateau (Hubbard and Shaw, 2009). Shortening estimate across the northern Qilian Shan indicates that the shortening

magnitude and strain were 33±6 km and 52±4% (Zuza et al., 2016), which is comparable with the strain value of 40–55% obtained from the seismic reflection profiles across the Qilianshan frontal thrust system (Yang et al., 2007). In the West Qinling Range of the northeastern Tibetan Plateau, the present-day crustal thickness of 45–55 km can also be reconciled with 10–12% crustal shortening strain and pure shear crustal thickening (Lease et al., 2012), suggesting that the crustal shortening can adequately generate the observed crustal thickness.

The presence of the regional-scale left-stepping en echelon topographic divides formed by tectonic uplifting might be the best example to illuminate the ongoing northeastward shortening of the Tibetan Plateau as presented in this study.

Several models have been proposed to explain the formation and development of fault-related fold, including the fault-bend (Suppe, 1983), pure-shear fault-bend (Suppe et al., 2004), and detachment folding (Epard and Groshong, 1995) models. Unlike these models, the regional-scale flexural folds formed between the HYF and WQLF, where no fault developed, indicating the off-fault deformation across the active fault zone from one to another. The spatial configuration of the four regional-scale topographic divides displays a left-stepping geometric pattern, indicating a left-lateral shearing between the HYF and WQLF (Figs. 4.1). However, it should be noted that the formation of these topographic divides is possibly caused by other tectonism such as thrusting, rather than the flexural folding alone. A part of field outcrops such as wavelike topography reported in the previously-published paper (Chen and Lin, 2019b) possibly formed by erosion are needed to be re-examined in a future study. Based on the topographic analyses and field observations, it is found that tectonic tilting and uplifting are still active in the northeastern Tibetan Plateau and that these topographic divides are still growing.

Therefore, there are various possible mechanisms to form these en echelon ridge crests; further confirmation of the true processes remains as a future work.

The maximum compressive stress inferred from the geologic structure and field observation indicates the NE–SW- to ENE–WSW-trending compression, possibly in associated with the northeastward expansion of the Tibetan Plateau (Fig. 7.1). The structural style presented in this study is similar with the wrench tectonics characterized by a zone of distributed shear featured by the en echelon folds in the region near the San Andreas Fault (Mount and Suppe, 1987). In deep structure, the lithospheric section across the North China Block and the Tibetan Plateau indicates that the lithospheric mantle of both blocks subducted to each other, yielding a NE–SW-trending compressive stress in the northeastern Tibetan Plateau (Tapponnier et al., 2001). The preexisting mechanically-weak suture zone was reactivated in the late Cenozoic, resulting in the left-lateral strike-slip initiation of these regional-scale strike-slip faults. The coupling relationship between the deep process and shallow surface deformation supports the knowledge of the northeastward growth and expansion of the Tibetan Plateau in order to accommodate the ongoing convergence between the Indian and Eurasian plates (Fig. 7.1).

7.2. Deformation mechanism of active tectonics

How was the northeastern Tibetan Plateau constructed and evolved in response to the ongoing Indian–Eurasian convergence since 65–55 Ma, which is fundamental in understanding the active tectonics of the northeastern Tibetan Plateau during the process of plateau outward expansion (Yin, 2006; Lease et al., 2012). The modern crustal motion revealed by the densely-distributed GPS networks in the Tibetan Plateau can

help constrain the active tectonic deformation of the northeastern Tibetan Plateau. GPS velocity decreases northeastward in the Tibetan Plateau with a relatively smooth gradient across the major active strike-slip faults (Zhang et al., 2004). No distinct velocity gap could be discerned from one side to another side of active faults, manifesting the continuous deformation between the major strike-slip faults and adjacent blocks (Zhang et al., 2004). The velocity magnitude drops from ~40 mm/yr in the Himalayan collisional zone to several millimeters per year in the northeastern margin, suggesting that most of the strain energy has been absorbed and partitioned by internal material deformation within the Tibetan Plateau. The NE-trending tectonic compressive stress in the northeastern Tibetan Plateau is discerned from the GPS observations (Zhang et al., 2004), which is also supported by the focal mechanisms and fault plane solutions of earthquakes that occurred in this area. The result is consistent with the report that 70%–94% of the India's convergence has been consumed by lithospheric shortening and topographic uplift (Shen et al., 2000, Wang et al., 2001). Large earthquakes frequently occurred on the main active strike-slip faults in the northeastern Tibetan Plateau. The orientation of the P-axes inferred from tens of large earthquakes was N24^{o} E–N50^{o} E, roughly perpendicular to the regional topographic contours and therefore parallel to the topographic gradients (Monlar et al., 1989). In fact, the orientation of P-axes in the marginal zones of the Tibetan Plateau varies from N–S-trending in the north to NE-trending in the northeastern margin, to E–W-trending in the Longmenshan Thrust Belt in the eastern margin, and to SE-trending in the Yungui Plateau in the southeastern margin, radiating from the collisional belt and surely related to the ongoing convergence between the Indian and Eurasian Plates (England and Houseman, 1986; Zhang et al., 2004).

The regional axis of the maximum compressive stress inferred from the geological structures and flexural folds developed in the late Cenozoic strata and deposits trends NE–SE to ENE–WSW as documented in Chapter 4, consistent with the results of GPS observations and focal mechanisms. Thus, the geological and geophysical evidence reaches the consensus that the active tectonics of the northeastern Tibetan Plateau is dominated by the NE–SW to ENE–WSW compressive stress, which is responsible for the left-lateral strike-slip motion of the major active faults and the formation of left-stepping en echelon topographic divides.

Finally, the active tectonic deformation in the northeastern Tibetan Plateau is suggested to be dominated by the tectonic compression associated with flexural folding and partially partitioned by the limited strike-slip displacement along the major strike-slip faults associated with the active faulting in the northeastern marginal zone of the Tibetan Plateau that has being caused by the ongoing northeastward expansion of the plateau accommodating the Indian–Eurasian plates' continental collision and convergence (Fig. 7.1).

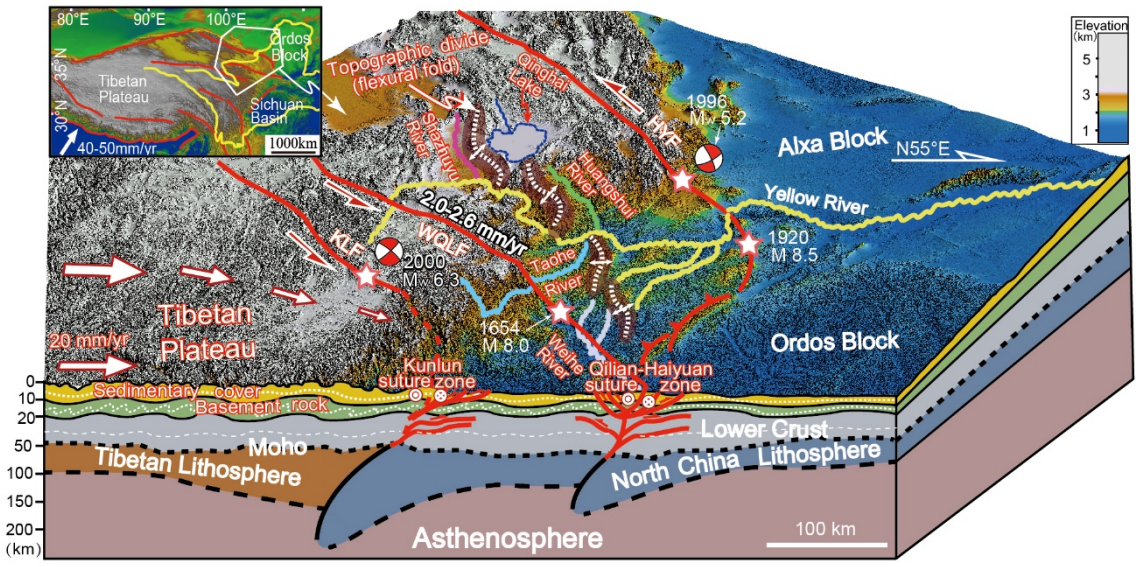

Fig. 7.1. Geodynamic model showing the active tectonic characteristics associated

with active flexural folding and faulting in the northeastern marginal zone of the Tibetan Plateau. Note the left-stepping en echelon topographic divides separating the Yellow River drainage systems and the low slip rate of 2.0–2.6 mm/yr on WQLF. The focal mechanisms are from the Global Harvard CMT catalogue (http://www.globalcmt.org). GPS data shown by arrows are modified from Zhang et al. (2004) and the lithospheric structures are modified from Tapponnier et al. (2001) and Ye et al. (2015). The white dashed line indicates the axis of topographic divide.

Chapter 8. Summary and conclusions

Based on the topographic and geological investigations and analyses carried out in this study, the main conclusions are summarized as follows:

1. The WNW-trending left-stepping en echelon topographic divides developed between the Haiyuan Fault and the West Qinling Fault separate the tributary drainage systems of the Yellow River, which lay the basic framework of the drainage system networks in the northeastern Tibetan Plateau. The late Cenozoic strata and deposits distributed on both sides of these divides has been tilted and folded, and the latest fluvial deposits are also tilted, manifesting that the tectonic tiling and uplifting near these divides are still active. The regional axis of the maximum compressive stress inferred from the associated fold deformation trends NE-SW to ENE–WSW. These results demonstrate that the formation of these topographic divides separating the Yellow River drainage systems in the northeastern Tibetan Plateau is likely to be associated with the flexural folding and uplifting under the northeastward compressive stress, corresponding to the ongoing northeastward compression accommodating the Indian–Eurasian continental convergence and collision.

2. The late Pleistocene–Holocene left-lateral strike-slip rate of the WQLF is estimated to be 2.0–2.6 mm/yr. Compared to other major active strike-slip faults developed in the northern and northeastern Tibetan Plateau such as the Altyn Tagh Fault and the Kunlun Fault with a high slip rate of > 10–20 mm/yr, the WQLF exhibits a relatively low slip rate of < 3 mm/yr, which is possibly related to the limited convergence transfer owing to the fact that most of the strain energy has been absorbed and partitioned by continuous crustal deformation in the northeastern marginal zone of the Tibetan Plateau, rather than the localized deformation along the active faults.

3. The result of paleoseismic study shows that: i) at least three or four large earthquakes have repeatedly occurred on WQLF in the past ~9000 years, suggesting the average recurrence interval of large earthquakes of 2250–3000 years; ii) There is a possibility that an unrecorded historic earthquake (E1) capable of producing surface rupture occurred near the trench 2 after 760–471 yr Cal BP. If not, the most recent surface-rupturing earthquake (E1) can correspond to the 1654 M 8.0 Tianshui earthquake, suggesting that the WQLF is the source seismogenic fault of the 1654 Tianshui earthquake, but not the LLF as previously reported; iii) the penultimate large earthquake occurred in the period of 2693–760 yr Cal BP; iv) the third recent large earthquake (E3) occurred in the period of 10229–6032 yr Cal BP, probably in the range of 9005–8596 yr Cal BP; v) Given the wide time-span for E3 and the recurrence discipline of characteristic fault, an inferred paleoearthquake possibly occurred in the period of 8596–6032 yr Cal BP, and the above E3 correspondingly become into E4 that occurred in the period of 9005–8596 yr Cal BP.

The detailed field observations and topographic analyses carried out in this study reveal that the present-day active tectonic deformation in the northeastern marginal zone of the Tibetan Plateau is mainly dominated by the flexural folding and left-lateral strike-slip faulting under the NE-trending compressive stress, and that the strain energy is absorbed and partitioned by the crustal shortening, topographic uplift, and the eastward extrusion along the major strike-slip faults.

GPS data of topographic images and field sites

Outcrops/Field photographs	Longitude	Latitude	Description
Fig. 4.4b	98º 50´23.37˝	36º 52´26.92˝	Central position
Fig. 4.4c	99º 52´31.26˝	36º 51´33.81˝	Central position
Fig. 4.4d	98º 46´59.48˝	36º 53´53.04˝	Central position
Fig. 4.4e	100º 51´53.80˝	36º 29´47.04˝	Central position
Fig. 4.5a	98º 54´11.85˝	36º 50´23.81˝	Central position
Fig. 4.5b	98º 54´15.83˝	36º 50´25.83˝	Central position
Fig. 4.5d	98º 54´14.37˝	36º 50´28.15˝	GPS160
Fig. 4.7b	103º 34´17.24˝	36º 05´33.74˝	GPS142
Fig. 4.9a	104º 43´53.45˝	35º 22´35.38˝	GPS107
Fig. 5.3 R1	103º 13´03.72˝	35º 12´19.73˝	Deflected point
Fig. 5.3 R2	103º 12´43.66˝	35º 12´20.09˝	Deflected point
Fig. 5.3 R3	103º 12´26.36˝	35º 12´22.11˝	Deflected point

Fig. 5.3 R4	103º 12´00.83˝	35º 12´20.23˝	Deflected point
Fig. 5.3 R5	103º 11´34.63˝	35º 12´23.12˝	Deflected point
Fig. 5.3 R6	103º 11´19.13˝	35º 12´27.01˝	Deflected point
Fig. 5.3 R7	103º 11´05.94˝	35º 12´29.23˝	Deflected point
Fig. 5.3 R8	103º 56´53.47˝	34º 59´25.83˝	Deflected point
Fig. 5.3 R9	103º 56´45.84˝	34º 59´30.33˝	Deflected point
Fig. 5.3 R10	103º 56´09.19˝	34º 59´41.34˝	Deflected point
Fig. 5.3 R11	103º 55´48.21˝	34º 59´45.04˝	Deflected point
Fig. 5.3 R12	103º 55´27.50˝	34º 59´54.17˝	Deflected point
Fig. 5.3 R13	103º 55´13.85˝	34º 59´56.48˝	Deflected point
Fig. 5.3 R14	103º 55´05.30˝	35º 00´02.18˝	Deflected point
Fig. 5.3 R15	103º 54´52.93˝	35º 00´08.46˝	Deflected point
Fig. 5.3 R16	103º 54´38.55˝	35º 00´15.79˝	Deflected point
Fig. 5.3 R17	103º 54´23.72˝	35º 00´21.68˝	Deflected point

Fig. 5.5 R18	103º 54´08.54″	35º 00´27.73″	Deflected point
Fig. 5.4 R19	104º 00´53.02″	34º 57´31.35″	Deflected point
Fig. 5.4 R20	104º 01´02.52″	34º 57´26.98″	Deflected point
Fig. 5.4 R21	104º 01´06.99″	34º 57´24.65″	Deflected point
Fig. 5.4 R22	104º 01´13.02″	34º 57´22.45″	Deflected point
Fig. 5.4 R23	104º 01´36.06″	34º 57´12.73″	Deflected point
Fig. 5.5a	102º 09´30.37″	35º 20´41.35″	CQ018
Fig. 5.6a	103º 10´20.13″	35º 12´29.56″	CQ059
Fig. 5.7a	103º 52´38.71″	35º 00´53.49″	CQ073
Fig. 5.9e	102º 11´55.51″	35º 19´50.90″	CQ005
Fig. 5.10f	102º 12´29.21″	35º 19´37.94″	CQ002
Fig. 6.2a	104º 01´12.05″	34º 57´23.10″	Central position
Fig. 6.3a	104º 01´22.67″	34º 57´18.49″	Central position
Fig. 6.3b	104º 01´29.18″	34º 57´15.63″	Central position

Fig. 6.3c	104º 01´35.54″	34º 57´13.09″	Central position
Fig. 6.3d	104º 01´44.01″	34º 57´10.46″	Central position
Fig. 6.4c	102º 07´54.25″	38º 21´09.58″	CQ027
Fig. 6.5a	104º 01´24.31″	34º 57´17.51″	
Fig. 6.5c	104º 01´36.16″	34º 57´12.74″	
Fig. 6.5d	104º 01´35.83″	34º 57´13.46″	
Fig. 6.6a	104º 01´33.97″	34º 57´13.87″	
Fig. 6.6b	104º 01´35.72″	34º 57´13.77″	
Fig. 6.6c	104º 01´35.10″	34º 57´13.36″	Trench 01 West Wall
Fig. 6.6d	104º 01´35.10″	34º 57´13.36″	Trench 01 East Wall
Fig. 6.7a	104º 01´35.84″	34º 57´13.11″	Trench 02

Citations for published work:

The main subject matters of this thesis have been published in the in the international journals *Geomorphology* and *Journal of Asian Earth Sciences*, respectively, as follows:

Chen, P., Lin, A., 2019. Topographic divides formed by active flexural folding in the NE marginal zone of the Tibetan Plateau. Geomorphology 332, 1–9.

Chen, P., Lin, A., 2019. Tectonic topography and Late Pleistocene activity of the West Qinling Fault, northeastern Tibetan Plateau. Journal of Asian Earth Sciences. 176, 68–78.

References:

Agnew, D.C., Sieh, K.E., 1978. A documentary study of the felt effects of the great California earthquake of 1857. Bulletin of Seismological Society of America. 68, 1717–1729.

Allen, C.R., Gillespie, A.R., Han, Y., Sieh, K.E., Zhang, B., Zhu, C., 1984. Red River and associated faults, Yunnan Province, China: Quaternary geology, slip rates, and seismic hazard. Geological Society of America Bulletin. 95, 686–700.

Ando, K., 1972. On the amounts of offset stream channels along the strike-slip faults in the Miura Peninsula, Izu Peninsula and Yamasaki regions. Geographical Review of Japan. 45, 716−725 (in Japanese with English abstract).

Armijo, R., Tapponnier, P., Han, T., 1989. Late Cenozoic right-lateral strike-slip faulting in southern Tibet. Journal of Geophysical Research. 94, 2787–838.

Avouac, J.P., Burov, E.B., 1996. Erosion as a driving mechanism of intracontinental mountain growth. Journal of Geophysical Research. 101, 17747–69.

Bai, R., Li, T.J., Huang, Y.F., Li, J.Y., Wang, G.Q., 2015. An efficient and comprehensive method for drainage network extraction from DEM with billions of pixels using a size-balanced binary search tree. Geomorphology 238, 56–67.

Beck, R.A., Burbank, D.W., Sercombe, W.J., Riley, G.W., Barndt, J.K., Berry, J.R., Afzal, J., Khan, A.M., Jurgen, H., Metje, J., Cheema, A., Shafique, N.A., Lawrence, R.D., Khan, M.A., 1995. Stratigraphic evidence for an early collision between northwest India and Asia. Nature 373, 55–58.

Bendick, R., Bilham, R., Freymueller, J., Larson, K., Yin, G., 2000, Geodetic evidence for a low slip rate in the Altyn Tagh fault system. Nature 404, 69–72.

Bird, P., 1991, Lateral extrusion of lower crust from under high topography in the

isostatic limit. Journal of Geophysical Research. 96, 10,275–10,286.

Brookfield, M.E., 1998. The evolution of the great river systems of southern Asia during the Cenozoic India-Asia collision: rivers draining southwards. Geomorphology 22, 285–312. https://doi.org/10.1016/j.geomorph.2008.01.003.

Brune, J.N., Henyey, T.L., Roy, R.F., 1969. Heat flow, stress, and rate of slip along the San Andreas Fault, California. Journal of Geophysical Research. 74, 3821–3827.

Bull, W.B., 1964. Geomorphology of Segmented Alluvial Fans in Western Fresno County, California, Professional Paper 352E, 89–129., United States Geological Survey, Washington, DC.

Burbank, D.W., Anderson, R.S., 2012. Tectonic geomorphology, 2nd edition., 38 pp., Wiley, West Sussex, U.K.

Burchfiel, B.C., Deng, Q.D., Molnar, P., Royden, L., Wang, Y.P., Zhang, P.Z., Zhang, W.Q., 1989. Intracrustal detachment zones of continental deformation. Geology 17, 448–452.

Burchfiel, B.C., Zhang, P.Z., Wang, Y.P., Zhang, W.Q., Song, F.M., Deng, Q.D., Monlar, P., Royden, L., 1991. Geology of the Haiyuan fault zone, Ningxia-Hui Autonomous Region, China, and its relation to the evolution of the northeastern margin of the Tibetan Plateau. Tectonics 10, 1091–1110. https://doi.org/10.1029/90TC02685.

Burchfiel, B.C., Chen, Z.L., Liu, Y.P., Royden, L.H., 1995. Tectonics of the Longmen Shan and adjacent regions, central China. International Geology Review. 37, 661–735.

Burnett, A.W., Schumm, S.A.,1983. Alluvial-river response to neo-tectonic deformation in Louisiana and Mississippi. Science 222, 49–50.

Catalano, S., Torrisi, S., Tortorici, G., Romagnoli, G., 2011. Active folding along a

rift-flank: the Catania region case history (SE Sicily). Journal of Geodynamics. 51, 52–63.

Champagnac, J.D., Yuan, D.Y., Ge, W.P., Molnar, P., Zheng, W.J., 2010. Slip rate at the northeastern front of the Qilian Shan, China. Terra Nova. 22, 180–187.

Chen, P., Lin, A., 2019a. Tectonic topography and Late Pleistocene activity of the West Qinling Fault, northeastern Tibetan Plateau. Journal of Asian Earth Sciences. 176, 68–78.

Chen, P., Lin, A., 2019b. Topographic divides formed by active flexural folding in the NE marginal zone of the Tibetan Plateau. Geomorphology 332, 1-9.

Chen, P., Yan, B., 2019. Systematic deflection and offset of drainage systems along the Altyn Tagh Fault in the northern Tibetan Plateau. Geomorphology (under review).

Chen, T., Zhang, P., Liu, J., Li, C., Ren, Z., Hudnut, K., 2014. The quantitative study of tectonic geomorphology of Haiyuan fault based on airborne LiDAR. Chinese Science Bulletin. 59, 2396–2409.

Chen, X., Yin, A., Gehrels, G.E., Cowgill, E.S., Grove, M., Harrison, T.M., and Wang, X.F., 2003. Two phases of Mesozoic north-south extension in the eastern Altyn Tagh range, northern Tibetan Plateau. Tectonics 22, 1053.

Chen, Z., Burchfiel, B.C., Liu, Y., King, R.W., Royden, L.H., Tang, W., Wang, E., Zhao, J., Zhang, X., 2000. Global Positioning System measurements from eastern Tibet and their implications for India/Eurasia intercontinental deformation. Journal of Geophysical Research. 105, 16215–16227.

Chengdu Institute of Geology and Mineral Resources, Chinese Academy of Geological Sciences., 1988. Geological map of Tibetan Plateau and adjacent region (scale 1:1500000). Geological Publishing House, Beijing.

Chevalier, M.L., Ryerson, F.J., Tapponnier, P., Finkel, R.C., Van der Woerd, J., Li, H.B., Liu, Q., 2005. Slip-rate measurements on the Karakorum fault may imply secular variations in fault motion. Science 307, 411–414.

China Earthquake Network Center (CENC), 2013. The 2013 Ms 6.6 earthquake occurred in the boundary area between Minxian and Zhangixan, Gansu Province, China. http://news.ceic.ac.cn/CC20130722074555.html (last accessed 1 Sep. 2018).

Clark, M.K., Royden, L.H., 2000, Topographic ooze: Building the eastern margin of Tibet by lower crustal flow: Geology 28, 703–706.

Clark, M.K., Schoenbohm, L.M., Royden, L.H., Whipple, K.X., Burchfiel, B.C., Zhang, X., Tang, W., Wang, E., Chen, L., 2004. Surface uplift, tectonics, and erosion of eastern Tibet from large-scale drainage patterns. Tectonics 23, 1–20. https://doi.org/10.1029/2002TC001402.

Clark, M.K., Farley, K.A., Zheng, D.W., Wang, Z.C., Duvall, A.R., 2010. Early Cenozoic faulting of the northern Tibetan Plateau margin from apatite (U-Th)/He ages. Earth and Planetary Sciences Letter. 296, 78–88.

Cowgill, E., Yin, A., Harrison, T.M., Feng, W.X. 2003. Reconstruction of the Altyn Tagh fault based on U–Pb geochronology: Role of backthrusts, mantle sutures and heterogeneous crustal strength in the forming the Tibetan plateau. Journal Geophysical Reserch. 108, doi:10.1029/2002JB002080.

Cowgill, E., Gold, R.D., Chen, X., Wang, X., Arrowsmith, J.R., Southon, J., 2009. Low Quaternary slip rate reconciles geodetic and geologic rates along the Altyn Tagh fault, northwestern Tibet. Geology 37, 647–650.

Craddock, W., Kirby, E., and Zhang, H., 2011, Late Miocene–Pliocene range growth in the interior of the northeastern Tibetan Plateau. Lithosphere 3, 420–438.

Dewey, J.F., Burke, K., 1973. Tibetan, Variscan and Precambrian basement reactivation: products of continental collision. Journal of Geology. 81, 683–692.

Dewey, J.F., Shackleton, R.M., Chang, C.F., Sun, Y.Y., 1988. The tectonic evolution of the Tibetan Plateau. Philosophical Transactions of the Royal Society of London. Series A, Mathematical and Physical Sciences. 327, 379–413.

Ding, G.Y., Chen, J., Tian, Q.J., Shen, X.H., Xing, C.Q. Wei, K.B., 2004. Active faults and magnitudes of left-lateral displacement along the northern margin of the Tibetan Plateau. Tectonophysics 380, 243–260,

Duvall, A.R., Clark, M.K., Kirby, E., Farley, K.A., Craddock, W.H., Li, C.Y., Yuan, D.Y., 2013. Low-temperature thermo-chronometry along the Kunlun and Haiyuan Faults, NE Tibetan Plateau: Evidence for kinematic change during late-stage orogenesis. Tectonics 32, 1190–1211.

Earthquake Disaster Prevention Department of China Earthquake Administration (EDPDCEA), 1995. Catalogue of Chinese Historical Strong Earthquakes. Seismological Press, Beijing, pp. 497–499 (in Chinese with English abstract).

England, P., Houseman, G., 1986. Finite strain calculations of continental deformation 2. Comparison with the India-Asia collision zone. Journal of Geophysical Research. 112, 3664–3676. https:// doi.org/10.1029/JB091iB03p03664.

England, P., Molnar, P., 1997. Active deformation of Asia: from kinematics to dynamics. Science 278, 647–650, doi:10.1126/science.278.5338.647.

England, P., Molnar, P., 2005. Late Quaternary to decadal velocity fields in Asia. Journal of Geophysical Research. 110, B12401, doi:10.1029/2004JB003541.

Epard, J.L., Groshong, R.H., 1995. Kinematic model of detachment folding including limb rotation, fixed hinges, and layer-parallel strain. Tectonophysics 247, 85–103.

https://doi.org/10.1016/0040-1951(94)00266-C.

Fang, X.M., Garzione. C., Vandervoo. R., Li, J.J, Fan, M.J., 2003. Flexural subsidence by 29 Ma on the NE edge of Tibet from the magnetostratigraphy of Linxia Basin, China. Earth and Planetary Science Letters. 210, 545–560.

Fang, X.M., Yan, M.D., Van der Voo, R., Rea, D.K., Song, C.H., Pares, J.M., Gao, J.P., Nie, J.S., Dai, S., 2005. Late Cenozoic deformation and uplift of the NE Tibetan plateau: Evidence from high-resolution magneto stratigraphy of the Guide Basin, Qinghai Province, China: Geological Society of America Bulletin. 117, 1208–1225.

Fang, L.H., Wu, J.P., Su, J.R., Wang, M.M., Jiang, C., Fan, L.P., Wang, W.L., Wang, C.Z., Tan, X.L., 2018. Relocation of mainshock and after sequence of the M_S 7.0 Sichuan Jiuzhaigou earthquake. Chinese Science Bulletin. 63, 649–662 (in Chinese with English abstract).

Feldl, N., Bilham, R., 2006. Great Himalayan earthquakes and the Tibetan plateau. Nature 444, 165–70.

Formento-Trigilio, M.L., Burbank, D.W., Nicol, A., Shulmeister, J., Rieser, U., 2002. River response to an active fold-and-thrust belt in a convergent margin setting, North Island, New Zealand. Geomorphology 49, 125–152.

Fu, B.H., Awata, Y., 2007. Displacement and timing of left-lateral faulting in the Kunlun Fault zone, northern Tibet, inferred from geological and geomorphic features. Journal of Asian Earth Sciences. 29, 253–265.

Gali, P., Galderisi, A., Ilardo, I and other four authors. 2018. Holocene paleoseismology of the Norcia fault system (Central Italy). Tectonophysics 745, 154-169.

Gan, W.J., Zhang, P.Z., Shen, Z.K., Niu, Z.J., Wang, M., Wan, Y.G., Zhou, D.M., Cheng, J., 2007. Present-day crustal motion within the Tibetan Plateau inferred from GPS

measurements. Journal of Geophysical Research. 112, B08416. https://doi.org/10.1029/2005jb004120.

Gansu Bureau of Geology and Mineral Resources (Gansu BGMR)., 1989. Regional geology of Gansu province (in Chinese with English abstract). Geological Publishing House, Beijing.

Gansu Bureau of Geology and Mineral Resources (Gansu BGMR), 1990. Geological map of Gansu Province (scale 1:1500000). Geological Publishing House, Beijing.

Gansu Bureau of Geology and Mineral Resources (Gansu BGMR)., 2006. Geological map of the Dingxi area (scale 1:250000). Geological Publishing House, Beijing.

Gao, R., Wang, H., Yin, A., Dong, S., Kuang, Z., Zuza, A.V., Li, W., Xiong, X., 2013, Tectonic development of the northeastern Tibetan Plateau as constrained by high-resolution deep seismic-reflection data. Lithosphere 5, 555–574.

Gaudemer, Y., Tapponnier, P., Meyer, B., Peltzer, G., Guo, S.M., Chen, Z.T., Dai, H.G., Cifuentes, I., 1995. Partitioning of crustal slip between linked, active faults in the eastern Qilian Shan, and evidence for a major seismic gap, the “Tianzhu gap” on the western Haiyuan fault, Gansu (China). Geophysical Journal International. 120, 599–645.

Gupta., S., 1997. Himalayan drainage patterns and the origin of fluvial megafans in the Ganges foreland basin. Geology 25, 11–14.

Han, Z.J., Xiang, H.F., Ran, Y.K., 2001. Active analysis of Lixian-Luojiapu fault zone in the east boundary of Tibetan Plateau since the Late Pleistocene. Seismology and Geology. 23, 43–48 (in Chinese with English abstract).

Harkins, N., Kirby, E., Shi, X., Wang, E., Burbank, D., Chun, F., 2010. Millennial slip rates along the eastern Kunlun fault: Implications for the dynamics of intracontinental

deformation in Asia. Lithosphere 2, 247–266.

Harvard University, 2014. Global CMT Catalog Search Available online at: http://www.globalcmt.org/CMT search.html. (last accessed, 11, Sep, 2018).

Holt, W.E., Chamot-Rooke, N., Le Pichon, X., Haines, A.J., Shen-Tu, B., Ren, J., 2000. Velocity field in Asia inferred from Quaternary fault slip rates and Global Positioning System observations. Journal of Geophysical Research. 105, 19185–19209.

Howard, A.D., 1967. Drainage analysis in geologic interpretation: a summation. The American Association of Petroleum Geologists Bulletin. 51, 2246–2259.

Houseman, G., England, P., 1993. Crustal thickening versus lateral expulsion in the Indian-Asian continental collision. Journal of Geophysical Research. 98, 12233–12249.

Hu, X., Pan, B., Kirby, E., Li, Q., Geng, H., Chen, J., 2010. Spatial differences in rock uplift rates inferred from channel steepness indices along the northern flank of the Qilian Mountain, northeast Tibetan Plateau. Chinese Science Bulletin. 55, 3205–3214.

Huang, W., 1993. Morphologic patterns of stream channels on the active Yishi Fault, southern Shandong Province, Eastern China: implications for repeated great earthquakes in the Holocene. Tectonophysics 219, 283–304.

Hubbard, J., Shaw, J.H., 2009. Uplift of the Longmen Shan and Tibetan plateau, and the 2008 Wenchuan (M= 7.9) earthquake. Nature 458, 194−197.

Hubert-Ferrari, A., Suppe, J., Gonzalez-Mieres, R., Wang, X., 2007. Mechanisms of active folding of the landscape (southern Tian Shan, China). Journal of Geophysical Research. 112, 1–39. https://doi.org/10.1029/2006JB004362.

Institute of Geology, State Seismological Bureau (SSB), 1990. The Haiyuan active fault

zone (in Chinese). Seismological Press, Beijing, pp. 134.

Jackson, J., Norris, R., Youngsun, J., 1996. The structural evolution of active fault and fold systems in central Otago, New Zealand: Evidence revealed by drainage patterns. Journal of Structural Geology. 18, 217–234.

Jade, S., Bhatt, B.C., Yang, Z., Bendick, R., Gaur, V.K., Molnar, P., Anand, M.B., Kumar, D., 2004. GPS measurements from the Ladakh Himalaya, India: Preliminary tests of plate-like or continuous deformation in Tibet. Geological Society of American Bulletin. 116, 1385–1391.

Jolivet, M., Brunel, M., Seward, D., Xu, Z.Q., Yang, J.S., Malavieille, J., Roger, F., Leyreloup, A., Arnaud, N., Wu, C., 2003. Neogene extension and volcanism in the Kunlun Fault Zone, northern Tibet: new constraints on the age of the Kunlun Fault. Tectonics 22, 1052. doi:10.1029/2002TC001428.

Jolivet, R., Cattin, R., Chamot-Rooke, N., Lasserre, C., Peltzer, G., 2008. Thin-plate modeling of interseismic deformation and asymmetry across the Altyn Tagh fault zone. Geophysical Research Letters. 35, L02309, doi:10.1029/2007GL031511.

Jolivet, R., Simons, M., Agram, P.S., Duputel, Z., Shen, Z.K., 2015. Aseismic slip and seismogenic coupling along the central San Andreas Fault. Geophysical Research Letter. 42, 297–306.

Kidd, W.S.F., Molnar, P., 1988. Quaternary and Active Faulting Observed on the 1985 Academia Sinica--Royal Society Geotraverse of Tibet. Philosophical Transactions of the Royal Society of London. 327, 337–363.

Kirby, E., Harkins, N., 2013. Distributed deformation around the eastern tip of Kunlun fault. International Journal of Earth Science. 102, 1759–1772.

Kirby, E., Reiners, P.W., Krol, M.A., Whipple, K.X., Hodges, K.V., Farley, K.A., Tang,

W.Q., Chen, Z.L., 2002. Late Cenozoic evolution of the eastern margin of the Tibetan Plateau: inferences from 40Ar/39Ar and (U-Th)/He thermochronology. Tectonics 21, 1–20. https://doi.org/10.1029/2000TC001246.

Kirby, E., Harkins, N., Wang, E.Q., Shi, X.H., Fan, C., Burbank, D., 2007. Slip rate gradients along the eastern Kunlun fault. Tectonics 26, 2, TC2010. https://doi.org/10.1029/2006TC002033.

Koons, P.O., 1995. Modelling the topographic evolution of collisional belts. Annual Review of Earth and Planetary Science. 23, 375–408.

Lanzhou Institute of Seismology, State Seismological Bureau, 1993. The study of earthquake hazard zoning, Gansu province (in Chinese). Lanzhou University Press, Lanzhou, China.

Lavé, J., Avouac, J.P., 2000. Active folding of fluvial terraces across the Siwaliks Hills, Himalayas of central Nepal. Journal Geophysical Research. 105, 5735–5770.

Lease, R.O., 2014. Cenozoic mountain building on the northeastern Tibetan Plateau. Geological Society of America, Special Paper. 507, 115–127. https://doi.org/10.1130/2014.2507(06).

Lease, R.O., Burbank, D.W., Zhang, H.P., Liu, J.H., Yuan, D.Y., 2012. Cenozoic shortening budget for the northeastern edge of the Tibetan Plateau: Is lower crustal flow necessary? Tectonics 31, TC3011, https://doi.org/10.1029/2011TC003066.

Leloup, P.H., Lacassin, R., Tapponnier, P., Schärer, U., Zhong, D.L., Liu, X.H., Zhang, L.S., Ji, S.C., Phan, T.T., 1995. The Ailao Shan-Red River shear zone (Yunnan China), tertiary transform boundary of Indochina. Tectonophysics 251, 3–84.

Li, C.Y., 2005. Quantitative studies on major active fault zones in Northeastern Qinghai-Tibet Plateau (Ph.D thesis). Institute of Geology, China Earthquake

Administration (in Chinese with English abstract).

Li, C.Y., Zhang, P.Z., Zhang, J.X., Yuan, D.Y., Wang., Z. C., 2007. Late Quaternary activity and slip rate of the western Qinling fault zone at Huangxianggou segment. Quaternary Science. 27, 54–63 (in Chinese with English abstract).

Li, C.Y., Zhang, P.Z., Yin, J.H., Min, W., 2009. Late Quaternary left-lateral slip rate of the Haiyuan fault, northeastern margin of the Tibetan Plateau. Tectonics 28, 1–26.

Li, H.B., Pan, J.W., Sun, Z.M., Liu, D.L., Zhang, J.J., Li, C.L., Liu, K., Marie-Luce, C., Yun, K., Gong, Z., 2015. Seismogenic structure and surface rupture characteristics of the 2014 M_S7.3 Yutian Earthquake. Acta Geologica Sinica. 89, 180–194 (in Chinese with English abstract).

Li, Y.H., Liu, M., Wang, Q.L., Cui, D.X., 2018. Present-day crustal deformation and strain transfer in northeastern Tibetan Plateau. Earth and Planetary Science Letters. 487, 179–189.

Lin, A., Guo, J.M., 2008. Non-uniform slip rate and millennial recurrence interval of large earthquakes along the eastern segment of the Kunlun fault, northern Tibet. Bulletin of Seismological Society of America. 98, 2866–2878.

Lin, A., Yang, Z.Y., Sun, Z.M., Yang, T.S., 2001. How and when did the Yellow River develop its square bend? Geology 29, 951–954.

Lin, A., Fu, B.H., Guo, J.M., Zeng, Q.L., Dang, G.M., He, W.G., Zhao Y., 2002. Co-Seismic Strike-Slip and Rupture Length Produced by the 2001 Ms 8.1 Central Kunlun Earthquake. Science 296, 2015–2017.

Lin, A., Guo, J.M., Kano, K., Awata, Y., 2006. Average Slip Rate and Recurrence Interval of Large-Magnitude Earthquakes on the Western Segment of the Strike-Slip Kunlun Fault, Northern Tibet. Bulletin of the Seismological Society of America. 96,

1597–1611.

Liu, B.Y., 2012. Study on Seismologic Tectonic and Mechanism on Two M 8 Historical Earthquakes at the Southeastern Area, Gansu Province (Master thesis). Lanzhou Institute of Seismology, China Earthquake Administration (in Chinese with English abstract).

Liu, M., Mooney, W.D., Li, S., Okaya, N., Detweiler, S., 2006. Crustal structure of the northeastern margin of the Tibetan Plateau from the Songpan-Ganzi terrane to the Ordos basin. Tectonophysics 420, 253–266.

Liu, M., Yang, Y., Shen, Z., Wang, S., Wang, M, Wan, Y., 2007. Active tectonics and intracontinental earthquakes in China: the kinematics and geodynamics. In: Stein, S., Mazzotti, S. (Eds.), Continental intraplate earthquakes: science, hazard, and policy issues: Geological Society of America Special Paper. 425, 299–318.

Liu-Zeng, J., Tapponnier, P., Gaudemer, Y., Ding, L., 2008. Quantifying landscape differences across the Tibetan plateau: implications for topographic relief evolution. Journal of Geophysical Research. 113, F04018.

Loveless, J.P., Meade, B.J., 2011. Partitioning of localized and diffuse deformation in the Tibetan Plateau from joint inversions of geologic and geodetic observations. Earth and Planetary Sciences Letter. 303, 11–24.

Matsuda, T., 1966. Strike-slip faulting along the Atotsugawa Fault, Japan. Bulletin of Earthquake Research Institute of University of Tokyo. 44, 1179–1212 (in Japanese with English abstract).

Matsuda, T., 1975. Active fault assessment for Irozaki fault system, Izu Peninsula. In: Tsuchi, R. (Ed.), Reports on the Earthquake off the Izu Peninsula, 1974, and the Disaster. Kurofune Press, Shizuoka, 121–125 (In Japanese).

Matsuda, I., 2004. River morphology and channel process in fresh surface water (Ed. James C.I. Dooge), in encyclopedia of life support systems (EOLSS), developed under the Auspices of the UNESCO, Eolss Publishers, Oxford, UK.

Maruyama, T., Lin, A., 2000. Tectonic history of the Rokko active fault zone (southwest Japan) as inferred from cumulative offsets of stream channels and basement rocks. Tectonophysics 323, 197–216.

McCalpin, J.P., 2009. Paleoseismology. 2nd Edition, Academic Press, Amsterdam-London.

Melosh, B.L., Keller, E.A., 2013. Effects of active folding and reverse faulting on stream channel evolution, Santa Barbara Fold Belt, California. Geomorphology 186, 119–135.

Mériaux, A.S., Ryerson, F.J., Tapponnier, P., Van der Woerd, J., Finkel, R.C., Xu, X.W., Xu, Z.Q., Caffee, M.W., 2004. Rapid slip along the central Altyn Tagh Fault: Morphochronologic evidence from Cherchen He and Sulamu Tagh. Journal of Geophysical Research. 109, B06401, doi:10/1029/2003jb002558.

Meyer, B., Tapponnier, P., Bourjot, L., Metivier, F., Gaudemer, Y., Peltzer, G., Guo, S.M., Chen, Z.T., 1998. Crustal thickening in Gansu-Qinghai, lithospheric mantle subduction, and oblique, strike-slip controlled growth of the Tibet plateau. Geophysical Journal International. 135, 1–47.

Molnar, P., 1988. Continental tectonics in the aftermath of plate tectonics. Nature 6186, 131–137.

Molnar, P., Lyon-Caen, H., 1989. Fault plane solutions of earthquakes and active tectonics of the northern and eastern parts of the Tibetan Plateau. Geophysical Journal International. 99, 123–153.

Molnar, P., Tapponnier, P., 1975. Cenozoic tectonics of Asia–Effects of a continental collision. Science 189, 419–426.

Molnar, P., Burchfiel, B.C., Liang, K., Zhao, Z., 1987. Geomorphic evidence for active faulting in the Altyn Tagh and northern Tibet and qualitative estimates of its contribution to the convergence of India and Eurasian. Geology 15, 249–253.

Molnar, P., England. P., Martinod, J., 1993. Mantle dynamics, the uplift of the Tibetan Plateau, and the Indian monsoon. Reviews of Geophysics. 31, 357–396.

Mount, V., Suppe, J., 1987. State of stress near the San Andreas fault: Implications for wrench tectonics. Geology 15, 1143–1146.

Olsson, I.U., 1968. Modern aspects of radiocarbon dating. Earth Science Reviews. 4, 203–218.

Okada, A., 1990. Studies of active faults by trenching method, in: N. Yonekura, A. Okada and A. Moriyama (Eds.), Tectonic Landforms. Kokon-Shoin, Tokyo, pp. 18-44 (in Japanese).

Ouchi, S., 2005. Development of offset channels across the San Andreas fault. Geomorphology 70, 112–128.

Palumbo, L., Hetzel, R., Tao, M., Li, X., 2011. Catchment-wide denudation rates at the margin of NE Tibet from in situ-produced cosmogenic 10Be. Terra Nova. 23, 42−48.

Pantosti, D., Addezio, G.D., Cinti, F.R., 1996. Paleoseismicity of the Ovindoli-Pezza fault, central Apennines, Italy: A history including a large, previously unrecorded earthquake in the Middle Ages (860-1300 A.D.) Journal of. Geophysical Research. 101, 5937−5959.

Peltzer, G., Saucier, F., 1996. Present-day kinematics of Asia derived from geologic fault rates. Journal of. Geophysical Research. 101, 27943–27956.

Peltzer, G., Tapponnier, P., Armijo, R., 1989. Magnitude of Late Quaternary left-lateral displacement along the north edge of Tibet. Science 246, 1285–1289.

Proceedings of Conference on Geological Problems of San Andreas Fault System, vol. XI. Stanford University Publications, Stanford, California.

Qinghai Bureau of Geology and Mineral Resources (Qinghai BGMR), 1989. Regional geology of Qinghai province (in Chinese with English abstract). Geological Publishing House, Beijing.

Qinghai Bureau of Geology and Mineral Resources (Qinghai BGMR), 2009. Geological map of the Minhe area (scale 1:250000). Geological Publishing House, Beijing.

Ramsey, C.B., 2009. Nayesian analysis of radiocarbon dates. Radiocarbon 51, 1337–1360.

Ramsey, L.A., Walker, R.T., Jackson, J., 2008. Fold evolution and drainage development in the Zagros mountains of Fars province, SE Iran. Basin Research. 20, 23–48.

Ramstein, G., Fluteau, F.F., Besse, J., Joussaume, S., 1997. Effect of orogeny, plate motion, and land-sea distribution on Eurasian climate change over the past 30 million years. Nature 286, 788–795.

Rao, G., Lin. A.M., Jia, D., Wu, X.J., Yan, B., Ren, Z.K., 2011. Co-seismic surface strike-slip shear structures produced by the 2010 M_w 6.9 Yushu earthquake, central Tibetan Plateau. Tectonophysics 507, 86–94.

Rao, G., Chen, P., Hu, J.M., Yu, Y.L., Qiu, J.H., 2016. Timing of Holocene paleo-earthquakes along the Langshan Piedmont Fault in the western Hetao Graben, North China: Implications for seismic risk. Tectonophysics 677, 115–124.

Ren, Z.K., Zhang, Z.Q., Chen, T., Yan, S.L., Yin, J.H., Zhang, P.Z., Zheng, W.J., Zhang,

H.P., Li, C.Y., 2016. Clustering of offsets on the Haiyuan Fault and their relationship to paleo-earthquakes. Geological Society of America Bulletin. 128, 3–18.

Ren, Z.K., Zielke, O., Yu, J.X., 2018. Active tectonics in 4D high-resolution. Jouranl of Structural Geology. 117, 264–271.

Roux-Mallouf, R.L., Ferry, M., Ritz, J and other three authors. 2016. First paleoseismic evidence for great surface-rupturing erthquakes in the Bhutan Himalayas. Journal of Geophysical Resarch: Solid Earth. 121, 7271–7283.

Royden, L.H., Burchfiel, B.C., King, R.E., Wang, E., Chen, Z., Shen, F., Liu, Y., 1997. Surface deformation and lower crustal flow in eastern Tibet. Science 276, 788–790.

Royden, L.H., Burchfiel, B.C., VanderHilst, R.D., 2008. The geological evolution of the Tibetan Plateau. Science 321, 1054–1058.

Ruddiman, W.F, Kutzbach, J.E., 1989. Forcing of Late Cenozoic northern hemisphere climate by plateau uplift in southern Asia and the American west. Journal of. Geophysical Research. 94, 18409–18427.

Russell, R.J. 1926. Recent horizontal offsets along the Haywards Fault. The Journal of Geology. 34(6), 507–511.

Sancar, T., Zabci, C and other three authors. 2019. Geometry and Paleoseismology of the Malatya Fault (Malatya-Ovacık Fault Zone), Eastern Turkey: Implications for intraplate deformation of the Anatolian Scholle. Journal of Seismology. 23, 319-340.

Scholz, P.H., 2000. Evidence for a strong San Andreas fault. Geology 28, 163–166.

Schumm, S.A., Dumont, J.F., Holbrook, J.M., 2000. Active tectonics and alluvial rivers. Cambridge University Press, Cambridge, UK, pp. 376.

Seeber, L., Gornitz, V., 1983. River profiles along the Himalayan arc as indicators of active tectonics. Tectonophysics 92, 335–367.

Sengör, A.M.C., Kidd, W.S.F., 1979. Post-collisional tectonics of the Turkish–Iranian Plateau and a comparison with Tibet. Tectonophysics 55, 361–376.

Shao, Y.X., Yuan, D.Y., Oskin, M.E., Wang, P.T., Zeng-Liu, J., Li, C.P., Wu, Z., 2017. Historical (Yuan Dynasty) Earthquake on the North Danghe Nanshan Thrust, Western Qilian Shan, China. Bulletin of the Seismological Society of America. 107, 1175−1184.

Shen, F., Royden, L.H., Burchfiel, B.C., 2001. Large-scale crustal deformation of the Tibetan Plateau. Journal of Geophysical Research. 106, 6793–6816.

Shen, Z.-K., Zhao, C., Yin, A., Li, Y., Jackson, D., Fang, P., and Dong, D., 2000. Contemporary crustal deformation in East Asia constrained by Global Positioning System measurement: Journal of Geophysical Research. 105, 5721–5734.

Shen, Z.K., Lu, J., Wang, M. Burgmann, R., 2005. Contemporary crustal deformation around the southeast borderland of the Tibetan Plateau. Journal of Geophysical Research. 110, doi:10.1029/2004JB003421.

Shi, W., Dong, S.W., Liu, Y., Hu, J.M., Chen, X.Q., Chen, P., 2015. Cenozoic tectonic evolution of the South Ningxia region, northeastern Tibetan Plateau inferred from new structural investigations and fault kinematic analyses. Tectonophysics 645, 139–164.

Sieh, K.E., 1978. Prehistoric large earthquakes produced by slip on the San Andreas Fault at Pallett Creek, Colifornia. Journal of Geophysical Research: Solid Earth, 83, 3907–3939.

Song, S., Zhang, L., Niu, Y., Su, L., Song, B. Liu, D., 2006. Evolution from oceanic subduction to continental collision: A case study from the northern Tibetan Plateau based on geochemical and geochronological data. Journal of Petrology. 47, 435–455.

Song, S., Niu, Y., Su, L., and Xia, X., 2013, Tectonics of the North Qilian orogen, NW China. Gondwana Research, 23, 1378–1401.

State Seismological Bureau (SSB), 1992. The Altyn Tagh Active Fault System (in Chinese). Seismological Press, Beijing, pp. 319.

Stuiver, M., Reimer, P.J., 1993. Extended ^{14}C data base and revised Calib 3.0 ^{14}C Age Calibration Program. Radiocarbon 35, 215–230.

Su, Y.Q., Liu, H.C., Wang, D.J., 2013. The geomorphic evidences of activity in Tanchang-Huangzui segment of Lixian-Luojiabao Fault zone since the Holocene. Northwestern Seismological Journal. 35, 1–6 (in Chinese with English abstract).

Sun, J.B., Yue, H., Shen, Z.K., Fang, L.H., Zhan, Y., Sun, X.Y., 2018. The 2017 Jiuzhaigou earthquake: a complicated event occurred in a young fault system. Geophysical Research Letters. 45, 2230–2240.

Suppe, J., 1983. Geometry and kinematics of fault-bend folding. American Journal of Science. 283, 684–721.

Suppe, J., Connors, C.D., Zhang, Y.K., 2004. Shear fault-bend folding. In: Thrust Tectonics and Hydrocarbon Systems, edited by K. McClay. The American Association of Petroleum Geologists Memoir. 82, 303–323.

Tapponnier, P., Molnar, P. 1976. Slip line field theory and large-scale continental tectonics. Nature 264, 319–324.

Tapponnier, P., Peltzer, G., Ledain, A.Y., Cobbold, P., 1982. Propagating extrusion tectonics in Asia–New insights from simple experiments with plasticine. Geology 10, 611–616.

Tapponnier, P., Xu, Z.Q., Roger, F., Meyer, B., Arnaud, N., Wittlinger, G., Yang, J.S., 2001. Oblique Stepwise Rise and Growth of the Tibet Plateau. Science 294, 1671–

1677.

Teng, R.Z., Jin, Y.Q., Li, X.H., Su, X.Z., 1994. Recent activity characteristics of the fault zone at northern edge of Western Qinling MT. Northwestern Seismological Journal. 16, 85–90 (in Chinese with English abstract).

Thatcher, W., 2007. Microplate model for the present-day deformation of Tibet. Journal of Geophysical Research: Solid Earth.112, B01401, doi:10.1029/2005JB004244.

The Research Group for Active Faults of Japan, 1991. Active faults in Japan-sheet maps and inventories (revised edition), 437 pp., University of Tokyo Press, Tokyo, Japan.

Walker, R.T., 2006. A remote sensing study of active folding and faulting in southern Kerman province, S.E. Iran. Journal of Structural Geology. 28, 654–668.

Wallace, R.E., 1968. Notes on stream channels offset by the San Andreas Fault, southern coast ranges, California, Dickson, William R., A. G. (Eds.), 6–21.

Wang, X., Metcalfe, I., Jian, P., He, L. Wang, C., 2000. The Jinshajiang–Ailaoshan suture zone, China: tectonostratigraphy, age and evolution. Journal of Asian Earth Sciences. 18, 675–690.

Wang, Q., Zhang, P.Z., Freymueller, J., Bilham, R., Larson, K., Lai, X., You, X.Z., Niu, Z.J., Wu, J.C., Li, Y.X., Liu, J.N., Yang, Z.Q., Chen, Q.Z., 2001. Present-day crustal deformation in China constrained by Global Positioning System (GPS) measurements. Science 294, 574–577.

Wang, M., Shen, Z., Niu, Z., Zhang, Z., Sun, H., Gan, W., Wang, Q., and Ren, Q., 2003. Modern crustal motion within China mainland and active block model. Science in China. 46, 25–40.

Wang, S.F., Fang, X.M., Zheng, D.W., Wang, E.Q., 2009. Initiation of Slip along the Xianshuihe fault zone, eastern Tibet, constrained by K-Ar and fission-track ages.

International Geology Review. 51, 1121–1131.

Watanabe, M., 1996. Some problems on event analysis in trenching survey. Active Fault Research. 15, 64–72 (in Japanese with English abstract).

Wells, D.L., Coppersmith, K.J., 1994. Updated empirical relationships among magnitude, rupture length, rupture area, and surface displacement. Bulletin of the Seismological Society of America. 84, 974–1002.

Wesnousky, S.G., Jones, L.M., Scholz, C.H., Deng, Q., 1984. Historical seismicity and rates of crustal deformation along the margins of the Ordos Block, North China. Bulletin of the Seismological Society of America. 74, 1767–1783.

Wesnousky, S.G., Prentice, C.S., Sieh, K.E., 1991. An offset Holocene stream channel and the rate of slip along the northern reach of the San Jacinto fault zone, San Bernardino Valley, California. Geological Society of America Bulletin. 103, 700–709.

Wittlinger, G., Tapponnier, P., Ooupinet, G., Jiang, M., Shi, D., Herquel, G., Masson, F., 1998. Tomographic evidence for localized lithospheric shear along the Altyn Tagh fault. Science 282, 74–76.

Wright, T.J., Parsons, B., England, P.C., Fielding, E.J., 2004. InSAR observations of low slip rates on the major faults of western Tibet. Science 305, 236–239.

Xi’an Institute of Geology and Mineral Resources, Chinese Academy of Geological Sciences., 1992. Geological map of Qinling-Daba Mountains and adjacent region (scale 1:1000000). Geological Publishing House, Beijing.

Xu, X.W., Yu, G.H., Klinger, Y., Tapponnier, P., Van Der Woerd, J., 2006. Reevaluation of surface rupture parameters and faulting segmentation of the 2001 Kunlunshan earthquake (Mw7.8), northern Tibetan Plateau, China. Journal of Geophysical

Research: Solid Earth, 111(B5).

Xu, X.W., Wen, X.Z., Yu, G.H., Chen, G.H., Klinger, Y., Hubbard, J., Shaw, J., 2009. Coseismic reverse- and oblique-slip surface faulting generated by the 2008 Mw 7.9 Wenchuan earthquake, China. Geology 37, 515–518.

Xu, X.W., Tan, X.B., Wu, G.D., Chen, J.B., Shen, J., Fang, W., Song, H.P., 2011. Surface rupture features of the 2008 Yutian M_S 7.3 earthquake and its tectonic nature. Seismology and Geology. 33, 462–471 (in Chinese with English abstract).

Yan, B., Lin, A., 2015. Systematical deflection and offset of the Yangtze River drainage system along the strike-slip Ganzi-Yushu-Xianshuihe Fault Zone, Tibetan Plateau. Journal of Geodynamics. 87, 13–25.

Yan, B., Lin, A., 2016. Holocene activity and paleoseismicity of the Selaha Fault, southeastern segment of the strike-slip Xianshuihe Fault Zone, Tibetan Plateau. Tectonophysics 694, 302–318.

Yang, J., Robinson, P., Jiang, C. Xu, Z., 1996. Ophiolites of the Kunlun Mountains, China and their tectonic implications. Tectonophysics 258, 215–231.

Yang, S.F., Chen, H.L., Cheng, X.G., Xiao, A., He, G., Chen, J., Tian, D., 2007. Deformation characteristics and rules of spatial change for the Northern Qilianshan thrust belt: Earth Science Frontiers. 14, 211–221.

Yang, Y.Q., Liu, M., 2009. Crustal thickening and lateral extrusion during the Indo-Asian collision: A 3D viscous flow model. Tectonophysics 465, 128–135.

Yang, X.P., Feng, X.J., Huang, X.N., Song, F.M., Li, G.Y., Chen, X.C., Zhang, L., Huang, W.L., 2015. The Late Quaternary activity characteristics of Lixian-Luojiabao fault: A discussion on the seismogenic mechanism of the Lixian M8 earthquake in 1654. Chinese Journal of Geophysics. 58, 504–519 (in Chinese with English

abstract).

Ye, Z., Gao, R., Li, Q.S., Zhang, H.S., Shen, X.Z., Liu, X.Z., Gong, C., 2015. Seismic evidence for the North China plate underthrusting beneath northeastern Tibet and its implications for plateau growth. Earth and Planetary Sciences Letter. 426, 109–117.

Yeats, R., Seih, K., Allen, C., 1997. The Geology of Earthquakes. Oxford University Press, Oxford, UK, pp. 568.

Yin, A., 2006. Cenozoic tectonic evolution of the Himalayan orogen as constrained by along-strike variation of structural geometry, exhumation history, and foreland sedimentation. Earth Science Review. 76, 1–131.

Yin, A., 2010. Cenozoic tectonic evolution of Asia: A preliminary synthesis. Tectonophysics 488, 293–325.

Yin, A., and Nie, S., 1996, A Phanerozoic palinspastic reconstruction of China and its neighboring regions, in Yin, A., and Harrison, T.M., eds., The tectonics of Asia: New York, Cambridge University Press, p. 442–485.

Yin, A., Harrison, M.K., 2000. Geologic evolution of the Himalayan-Tibetan orogeny. Annual Reviews of Earth and Planetary Sciences. 28, 211–280.

Yin, A., Rumelhart, P.E., Butler, R., Cowgill, E., Harrison, T.M., Foster, D.A., Ingersoll, R.V., Zhang, Q., Zhou, X.Q., Wang, X.F., Hanson, A., Raza, A., 2002. Tectonic history of the Altyn Tagh fault system in northern Tibet inferred from Cenozoic sedimentation. Geological Society of America Bulletin. 114, 1257–1295.

Yu, J.X., Zheng, W.J., Yuan, D.Y., Pang. J.Z., Liu, X.W., Liu, B.Y., 2012. Late Quaternary active characteristics and slip rate of Pingding-Huama fault, the eastern segment of Guanggaishan-Dieshan fault zone (west Qinling Mountain). Quaternary Science. 32, 957–967 (Chinese with English abstract).

Yuan, D.Y., and other 21 authors., 2013. The growth of northeastern Tibet and its relevance to large-scale continental geodynamic: a review of recent studies. Tectonics 32, 1–13.

Yuan, D.Y., Lei, Z.S., Wang, A.G., 2017. Additional textual criticism of southern Tianshui M8 earthquake in Gansu province in 1654. China Earthquake Engineering Journal. 39, 0509–0520 (in Chinese with English abstract).

Yue, Y., Ritts, B.D., Graham, S.A., Wooden, J.L., Gehrels, G.E., Zhang, Z., 2003. Slowing extrusion tectonics: lowered estimate of post-Early Miocene slip rate for the Altyn Tagh fault. Earth Planetary Science Letter. 217, 111–122.

Zhang, P.Z., Monlar, P., Burchfiel, B.C., Royden, L., Wang, Y.P., Deng, Q.D., Song, F.M., Zhang, W.Q., Jiao, D.C., 1988a., Bounds on the Holocene slip rate of the Haiyuan fault, north-central China. Quaternary Research. 30, 151–164.

Zhang, P.Z., Monlar, P., Zhang, W.Q., Deng, Q.D., Wang, Y.P., Burchfiel, B.C., Song, F. M., Royden, L., Jiao, D.C., 1988b. Bounds on the average recurrence interval of major earthquakes along the Haiyuan fault in north-central China. Seismical Research Letter. 59, 81–89.

Zhang, P.Z., Shen, Z.K., Wang, M., Gan, W.J., Bürgmann, R., Molnar, P., Wang, Q., Niu, Z.J., Sun, J.Z., Wu, J.C., 2004. Continuous deformation of the Tibetan Plateau from global positioning system data. Geology 32, 809–812.

Zhang, Y.Q., Mercier, J.L., Vergely, P., 1998. Extension in the graben system around the Ordos (China), and its contribution to the extrusion tectonics of south China with respect to Gobi-Mongolia. Tectonophysics 285, 41–75.

Zheng, D.W., Zhang, P.Z., Wan, J.L., Yuan, D.Y., Li, C.Y., Yin, G.M., Zhang, G.L., Wang, Z.C., Min, W., Chen, J., 2006. Rapid exhumation at ~8 Ma on the Liupan Shan

thrust fault from apatite fission-track thermochronology: Implications for growth of the northeastern Tibetan Plateau margin. Earth and Planetary Science Letters. 248, 198–208.

Zheng, W.J., Liu, X.W., Yu, J.X., Yuan, D.Y., Zhang, P.Z., Pang, J.Z., Liu, B.Y., 2016. Geometry and Late Pleistocene slip rates of the Liangdang-Jiangluo fault in the western Qinling mountains, NW China. Tectonophysics 687, 1–13.

Zuza, A.V., Cheng, X., Yin, A., 2016. Testing models of Tibetan Plateau formation with Cenozoic shortening estimates across the Qilian Shan-Nan Shan thrust belt. Geosphere 12, 501–532.